

# **Computational approaches for nuclear design analyses of the stellarator power reactor HELIAS**

Zur Erlangung des akademischen Grades

**Doktor der Ingenieurwissenschaften (Dr.-Ing.)**

von der KIT-Fakultät für Maschinenbau des  
Karlsruher Instituts für Technologie (KIT)

genehmigte

**Dissertation**

von

André Häußler M.Sc.

|                             |  |
|-----------------------------|--|
| Tag der mündlichen Prüfung: | 28.09.2020   |
| Hauptreferent:              | Prof. Dr.-Ing. Robert Stieglitz<br>Karlsruher Institut für Technologie (KIT)   |
| Korreferent:                | Prof. Dr. Robert Wolf<br>Max-Planck-Institut für Plasmaphysik (IPP) Greifswald |



This document is licensed under a Creative Commons Attribution-ShareAlike 4.0 International License (CC BY-SA 4.0): <https://creativecommons.org/licenses/by-sa/4.0/deed.en>

---

Hiermit erkläre ich, dass ich die vorliegende Arbeit selbstständig angefertigt, noch nicht anderweitig für Prüfungszwecke vorgelegt und keine anderen als die angegebenen Quellen und Hilfsmittel benutzt sowie die wörtlich und inhaltlich übernommenen Stellen als solche kenntlich gemacht und die Satzung des Karlsruher Institut für Technologie (KIT) zur Sicherung guter wissenschaftlicher Praxis in der jeweils gültigen Fassung beachtet habe.

Karlsruhe, den 21.07.2020

André Häußler

# Abstract

The Helical-Axis Advanced Stellarator (HELIAS) is a conceptual design of a stellarator-type fusion power reactor proposed by Max-Planck-Institute for Plasma Physics (IPP) Greifswald with a thermal fusion power of 3000 MW. The shape of the stellarator is defined by the non-planar shaped magnetic field coils, which generate a twisted plasma confining magnetic field. For the HELIAS 5-B reactor design, a comprehensive Monte Carlo (MC) based neutronic design analysis with the Monte Carlo N-Particle (MCNP) transport code is developed to provide important nuclear parameters like the Neutron Wall Loading (NWL), the neutron flux distribution, the Tritium Breeding Ratio (TBR) and the shielding performance.

The complex toroidal twisted HELIAS stellarator geometry is created fully by higher-order surfaces following the shape of the magnetic field from a CAD model into an MCNP representation. Three different geometry transfer options have been investigated and the faceted geometry formed by a triangular surface mesh on the CAD geometry in the Direct Accelerated Geometry Monte Carlo (DAGMC) approach is considered as the most promising option because it is capable of using the complex geometry without any restrictions.

For the neutronic characterisation of HELIAS, the original CAD envelope model is separated radially into different functional layers filled with homogenised material mixtures to represent the breeding blanket based on the Helium Cooled Pebble Bed (HCPB) concept, the back supporting structure, the vacuum vessel and the shielding. The NWL distribution shows a variation of the load across the first wall with a peak load of  $1.93 \text{ MW m}^{-2}$  and an average load of  $0.95 \text{ MW m}^{-2}$ . The neutron flux distribution is obtained with a peak flux inside the plasma of  $4 \times 10^{14} \text{ n/cm}^2/\text{s}$ , which is attenuated through the blanket and vacuum vessel to  $1 \times 10^{10} \text{ n/cm}^2/\text{s}$ . The TBR in this configuration is  $\sim 1.38$ , a rather optimistic value due to the applied homogenised material mixtures.

The reactor components need to provide sufficient shielding for the radiation protection of sensitive equipment. The attenuation of the plasma neutron flux by four orders

of magnitude through the bulk shield leads to an increase of the relative statistical error which requires the application of variance reduction methods to reduce the statistical error in these domains. The shielding calculations conducted with application of the mesh based weight window approach for variance reduction have been assessed in an area with a NWL of  $\sim 1.35 \text{ MW m}^{-2}$  and less radial thickness of  $\sim 1.0 \text{ m}$ . The requirements specified for the EU DEMO tokamak fusion reactor cannot be met by HELIAS and the need for enhancing the shielding capabilities is indicated by increasing the shielding layer and/or applying advanced shielding materials.

Here, for the first time a comprehensive neutronic investigation of HELIAS is conducted, which is based on a verified computational radiation transport methodology. This approach is applicable to future nuclear engineering design analyses for this reactor type, targeting at optimised breeding blanket concepts and advanced nuclear shielding indispensable for a fusion reactor.

# Zusammenfassung

Der Helical-Axis Advanced Stellarator (HELIAS) ist ein konzeptioneller Entwurf eines nach dem Stellarator Konzept operierenden Fusionsleistungsreaktor, der vom Max-Planck-Institut für Plasmaphysik (IPP) Greifswald mit einer thermischen Fusionsleistung von 3000 MW entwickelt wurde. Die Form des Stellarators ist durch nicht-planare Magnetfeldspulen charakterisiert, die ein Plasma einschließendes Magnetfeld erzeugen. Für das HELIAS 5-B Reaktordesign wird eine erste umfassende Monte Carlo (MC) basierte Neutronik Designanalyse mit dem Monte Carlo N-Particle (MCNP) Strahlentransportcode durchgeführt, um wichtigen nukleare Kenngrößen wie die Neutronenwandbelastung (NWL), die Neutronenflussverteilung, die Tritium-Brutrate (TBR) und das Abschirmvermögen zu ermitteln.

Die komplexe toroidal verdrillte HELIAS Stellaratorgeometrie wird vollständig durch Oberflächen höherer Ordnung beschrieben, welche der Form des Magnetfeldes folgen und von einem CAD-Modell in ein MCNP-Modell übertragen werden müssen. Es wurden drei verschiedene Möglichkeiten zur Geometriekonvertierung untersucht, wobei die facettierte Geometrie, die durch ein trianguliertes Oberflächennetz auf der CAD-Geometrie im Direct Accelerated Geometry Monte Carlo (DAGMC) Ansatz als die vielversprechendste Option angesehen wird, da sie die komplexe Geometrie ohne Einschränkungen nutzen kann.

Für die neutronenphysikalische Charakterisierung von HELIAS wurde das ursprüngliche CAD-Modell in radialer Richtung in unterschiedliche funktionelle Schichten aufgeteilt und mit homogenisierten Materialmischungen gefüllt, basierend auf dem Helium Cooled Pebble Bed (HCPB) Brutblanket Konzept, der Stützstruktur, dem Vakuumbehälter und der Abschirmung. Die NWL Verteilung zeigt eine Variation der Belastung über die gesamte erste Wand mit einer Spitzenlast von  $1.93 \text{ MW m}^{-2}$  und einer Durchschnittslast von  $0.95 \text{ MW m}^{-2}$ . Die Neutronenflussverteilung hat einem maximalen Wert innerhalb der Plasmakammer von  $4 \times 10^{14} \text{ n/cm}^2/\text{s}$ , die durch das Blanket und den Vakuumbehälter auf  $1 \times 10^{10} \text{ n/cm}^2/\text{s}$  abgeschwächt wird. Die TBR in dieser Konfiguration beträgt  $\sim 1.38$ ; ein eher optimistischer Wert, welcher auf die Anwendung

von homogenisierten Materialmischungen zurückzuführen ist.

Die Reaktorkomponenten müssen ein ausreichendes Abschirmvermögen aufweisen, um strahlungsempfindliche Bauteile zu schützen. Die Abschwächung des Neutronenflusses um vier Größenordnungen durch die verwendete Abschirmung führt zur Erhöhung des statistischen Fehlers, der die Anwendung von Varianzreduktionsverfahren erforderlich macht. Die Abschirmberechnungen basierend auf der Technik der gitterbasierten Weight Window Verfahrens wurden in einem Bereich mit einem NWL von  $\sim 1.35 \text{ MW m}^{-2}$  und einer geringen radialen Baudicke von  $\sim 1.0 \text{ m}$  durchgeführt. Die für den EU-Tokamak-Fusionsreaktor DEMO definierten Grenzwerte bezüglich des Abschirmvermögens können von HELIAS in dem aktuellen Design nicht erfüllt werden. Es wird deutlich, dass hier signifikante Verbesserungen der Abschirmung erforderlich sind, die durch die Erhöhung der radialen Abschirmungsschichtdicke und/oder der Anwendung fortschrittlicher Abschirmmaterialien erreichbar sind.

Die hier vorgestellte Arbeit präsentiert erstmals eine umfassende neutronenphysikalische Untersuchung eines auf dem Stellaratorprinzip beruhendem Leistungsreaktors am Beispiel des HELIAS-Designs, die auf einer verifizierten numerischen Methodik für den Strahlungstransport basiert. Dieser Ansatz ist für zukünftige neutronenphysikalische Anwendungen für diesen Reaktortyp anwendbar. Er ermöglicht die Entwicklung optimierter Brutblanket-Konzepte und fortschrittlicher Strahlungsabschirmungen, die für einen Fusionsreaktor unverzichtbar sind.

# Contents

|   |            |
|---|------------|
| <b>Abstract</b>   | <b>III</b> |
| <b>Zusammenfassung</b>  | <b>V</b>   |
| <b>Nomenclature</b>   | <b>X</b>   |
| <b>1 Introduction and Overview</b>  | <b>1</b>   |
| 1.1 Nuclear Fusion . . . . .  | 1          |
| 1.2 HELIAS 5-B conceptual design . . . . .                                  | 7          |
| 1.3 Current stellarator research status . . . . .                           | 9          |
| 1.4 Objective and Purpose . . . . .   | 10         |
| <b>2 Fusion Neutronics, Monte Carlo Method and Breeding Blanket Concept</b> | <b>12</b>  |
| 2.1 Neutrons and their interaction with matter . . . . .                    | 12         |
| 2.2 Monte Carlo method . . . . .  | 17         |
| 2.2.1 Fundamental Monte Carlo laws . . . . .                                | 17         |
| 2.2.2 Monte Carlo neutron transport simulation . . . . .                    | 18         |
| 2.3 Monte Carlo particle transport code MCNP . . . . .                      | 19         |
| 2.3.1 Computational geometry definition . . . . .                           | 20         |
| 2.3.2 Tally definition . . . . .  | 23         |
| 2.3.3 Estimation of Monte Carlo Errors . . . . .                            | 24         |
| 2.3.4 Variance Reduction Methods of Monte Carlo Calculations . . . . .      | 28         |
| 2.4 Fusion Neutronics . . . . .   | 30         |
| 2.5 Neutronic aspects in Breeding Blanket Concepts . . . . .                | 32         |
| <b>3 Transfer of CAD data to nuclear physics representation</b>             | <b>38</b>  |
| 3.1 Problem statement and possible transfer options . . . . .               | 38         |
| 3.2 Overview and Preparation of the HELIAS 5-B CAD model . . . . .          | 41         |



---

|          |   |           |
|----------|---|-----------|
| 3.2.1    | Examination of a stellarator half-field period . . . . .  | 42        |
| 3.2.2    | Repair of the envelope model . . . . .  | 43        |
| 3.2.3    | Refinement of the envelope model and introducing material layers                                      | 44        |
| 3.3      | CAD models before translating into MC geometry representation . . .                                   | 49        |
| 3.3.1    | Global HELIAS CAD model ready for neutronics simulation . .   | 49        |
| 3.3.2    | CAD model for the Neutron Wall Loading (NWL) calculation .  | 49        |
| 3.3.3    | CAD geometry for set-up of the MCNP boundary condition . .  | 51        |
| 3.4      | Analysis of different options to represent a stellarator geometry . . . .                             | 53        |
| <b>4</b> | <b>CAD to MCNP Geometry Conversion Method Verification</b>  | <b>56</b> |
| 4.1      | Construction of the CAD verification geometry . . . . .   | 56        |
| 4.2      | Neutron source for the verification geometry . . . . .  | 59        |
| 4.3      | Computation and Results . . . . .   | 60        |
| 4.4      | Conclusion of the investigated approaches . . . . .   | 63        |
| <b>5</b> | <b>Neutron Source development for HELIAS</b>  | <b>64</b> |
| 5.1      | Procedure of the MCNP Neutron Source development . . . . .  | 64        |
| 5.2      | Verification of the MCNP Neutron Source Subroutine . . . . .  | 70        |
| <b>6</b> | <b>Variance Reduction Technique applied to the Stellarator</b>  | <b>72</b> |
| 6.1      | Identification of suitable Variance Reduction Techniques . . . . .                                    | 72        |
| 6.2      | Application of cell based importance sampling technique to the CAD<br>verification geometry . . . . . | 73        |
| 6.3      | Generation of mesh based weight windows . . . . .   | 78        |
| 6.4      | Summary of variance reduction methods for HELIAS . . . . .  | 89        |
| <b>7</b> | <b>Nuclear Responses for a generic HELIAS reactor design</b>  | <b>90</b> |
| 7.1      | Neutron Wall Loading (NWL) . . . . .  | 90        |
| 7.1.1    | Procedure for NWL assessment . . . . .  | 91        |
| 7.1.2    | Computational Results . . . . .   | 91        |
| 7.2      | Neutron Flux Distribution . . . . .   | 99        |
| 7.3      | Tritium Breeding Ratio (TBR) . . . . .  | 102       |
| 7.4      | Analyses of reactor shielding performance . . . . .   | 104       |
| 7.4.1    | Neutron flux . . . . .  | 106       |
| 7.4.2    | Nuclear power density . . . . .   | 108       |
| 7.4.3    | Radiation damage . . . . .  | 110       |
| 7.4.4    | Gas production . . . . .  | 112       |

|                              |            |
|------------------------------|------------|
| <b>Contents</b>              | <b>IX</b>  |
| <hr/>                        |            |
| <b>8 Summary and Outlook</b> | <b>118</b> |
| <b>References</b>            | <b>121</b> |
| <b>A Appendix</b>            | <b>132</b> |
| <b>Acknowledgements</b>      | <b>149</b> |

# Nomenclature

|                |   |
|----------------|---|
| <b>ADVANTG</b> | Automated VARIance reducTION Generator                                      |
| <b>appm</b>    | Atomic Parts Per Million  |
| <b>BB</b>      | Breeding Blanket  |
| <b>BSS</b>     | Back Supporting Structure   |
| <b>CAD</b>     | Computer-Aided Design   |
| <b>CIEMAT</b>  | Centro para Investigaciones Energéticas, Medioambientales y<br>Tecnológicas |
| <b>CP</b>      | Cumulative Probability  |
| <b>CPs</b>     | Cooling Plates  |
| <b>CSG</b>     | Constructive Solid Geometry   |
| <b>DAG</b>     | Direct Accelerated Geometry   |
| <b>DAGMC</b>   | Direct Accelerated Geometry Monte Carlo                                     |
| <b>DCLL</b>    | Dual Coolant Lithium Lead   |
| <b>DEMO</b>    | Demonstration Fusion Power Reactor  |
| <b>DPA</b>     | Displacement Per Atom   |
| <b>ENDF</b>    | Evaluated Nuclear Data Format   |
| <b>EU</b>      | European Union  |
| <b>FOM</b>     | Figure of Merit   |
| <b>FPY</b>     | Full Power Year   |
| <b>FW</b>      | First Wall  |
| <b>HCLL</b>    | Helium Cooled Lithium Lead  |
| <b>HCPB</b>    | Helium Cooled Pebble Bed  |
| <b>HELIAS</b>  | Helical-Axis Advanced Stellarator   |
| <b>INEST</b>   | Institute of Nuclear Energy Safety Technology                               |
| <b>IPP</b>     | Max-Planck-Institute for Plasma Physics                                     |
| <b>ITER</b>    | International Thermonuclear Experimental Reactor                            |
| <b>JEFF</b>    | Joint Evaluated Fission and Fusion File                                     |
| <b>KfK</b>     | Kernforschungszentrum Karlsruhe   |
| <b>KIT</b>     | Karlsruhe Institute of Technology   |
| <b>LANL</b>    | Los Alamos National Laboratory  |
| <b>LHD</b>     | Large Helical Device  |
| <b>LCFS</b>    | Last Closed Flux Surface  |
| <b>MC</b>      | Monte Carlo   |
| <b>MCNP</b>    | Monte Carlo N-Particle  |
| <b>MPI</b>     | Message Passing Interface   |
| <b>NIFS</b>    | National Institute for Fusion Science                                       |
| <b>NRT</b>     | Norgett-Robinson-Torrens  |
| <b>NWL</b>     | Neutron Wall Loading  |

---

|                |  |
|----------------|--|
| <b>PDF</b>     | Probability Density Function   |
| <b>RAM</b>     | Random-Access Memory   |
| <b>RN</b>      | Random Number  |
| <b>SuperMC</b> | Super Multi-functional Calculation Program for Nuclear Design and<br>Safety Evaluation |
| <b>TFC</b>     | Tally Fluctuation Chart  |
| <b>TBR</b>     | Tritium Breeding Ratio   |
| <b>UM</b>      | Unstructured Mesh  |
| <b>VR</b>      | Variance Reduction   |
| <b>VV</b>      | Vacuum Vessel  |
| <b>W7-X</b>    | Wendelstein 7-X  |
| <b>WCLL</b>    | Water Cooled Lithium Lead  |
| <b>WW</b>      | Weight Window  |

# Chapter 1

## Introduction and Overview

Fusion power plants are under investigation as a worldwide research and development subject, because they are considered to be a promising technology of a carbon dioxide free electricity production. The presented thesis is devoted to the first closed nuclear analyses of a magnetic confinement fusion power plant based on the stellarator concept. Here, the principal idea of nuclear fusion and the magnetic confinement based on the stellarator concept are outlined, before the major objectives are formulated from which the structure of the thesis is deduced.

### 1.1 Nuclear Fusion

Nuclear fusion describes a reaction of two or more isotopes as a union to form one or more different atomic nuclei. The mass difference between reactants and products is due to the difference in the ‘atomic binding energy’, which is individual for each isotope and shown in figure 1.1 as binding energy per nucleon. An atomic nucleus consists of protons and neutrons that are referred to as nucleon, except hydrogen which has only one proton in its atomic nucleus. In the fusion reaction, the difference in binding energy can induce a release of energy on the fusion product. The binding energy per nucleon  $E_B$  [MeV] as function of the nucleon number  $A$  is presented in figure 1.1. It shows a maximum binding energy per nucleon for the nickel isotope  $^{62}\text{Ni}$  [Hua17]. Isotopes left from nickel are favourable for nuclear fusion due to their release of energy during a fusion reaction. Isotopes with a higher nucleon number than nickel are not suitable for fusion, but some of them can undergo a fission reaction typically induced by neutron absorption. A widely used fissile material in a nuclear power plant is uranium, especially the isotope  $^{235}\text{U}$ , and its fission reaction releases energy, 2 – 3 neutrons and fission products with a nucleon number in the range of 90 – 160 [Bor11].

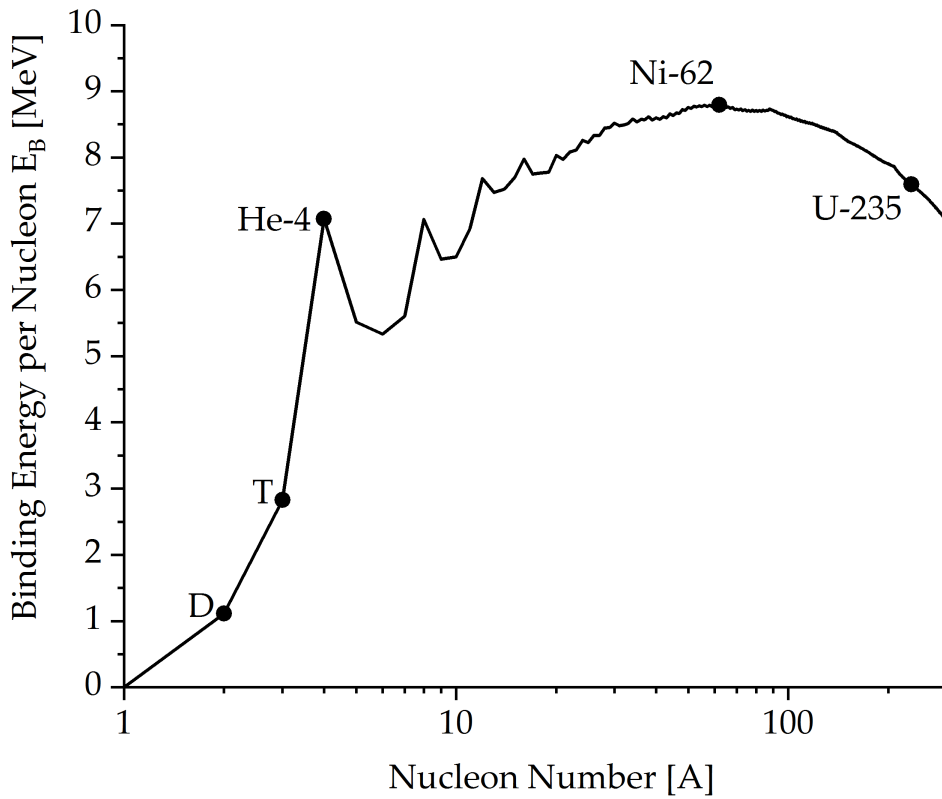


Figure 1.1: Binding energy per nucleon  $E_B$  as function of the nucleon number  $A$ , data from [Hua17].

The most prominent fusion reactor in nature is the sun with its proton-proton chain fusion reaction. The sun itself consists of a plasma with strongly varying density and temperature from its core to the surface corona [Str11]. In its centre, the temperatures are of  $\sim 1.5$  keV ( $\sim 17 \times 10^6$  °C) and densities of  $\sim 10^{32}$  m $^{-3}$ , which is around 1000 times higher than the solid state density on earth [Str11]. The proton-proton chain reaction cannot be reproduced on earth with the ratio between temperature and density, and it also has a very low reaction rate. Therefore, different boundary conditions, as well as different reactants, are necessary for generating a stable fusion reaction for a possible fusion power plant on earth.

The fusion of light atoms on earth requires a high temperature to generate a plasma, which must be confined either with magnetic or inertial confinement [Kau13]. The fusion research in Europe mainly follows the magnetic confinement which is investigated in this work. Charged particles typically move along magnetic field lines, but only a closed ring shape magnetic field can confine the particles with less losses. The magnetic field in a torus configuration consists of a toroidal and a poloidal magnetic field. The magnetic field lines must be twisted, which is achieved by overlapping the toroidal and poloidal field lines to create a torus shape field with almost uniform magnetic field

strength. The magnetic confinement designates the resulting magnetic field to confine the fusion plasma inside. Typical plasma parameters for the magnetic confinement are temperatures of  $T = (10\dots 20)\text{keV}$  (equivalent to  $T \approx (116\dots 232) \times 10^6\text{°C}$ ) and a particle density of  $n = (1\dots 2) \times 10^{20} \text{ m}^{-3}$  [Kau13].

A very promising fusion reaction is between the hydrogen isotopes Deuterium ( $D$ ) and Tritium ( $T$ ):



where both isotopes transform after their fusion into a neutron ( $n$ ), a helium nucleus ( $He$ ) and an energy release of  $\sim 17.6 \text{ MeV}$ . The energy is distributed to the neutron and the helium atom accordingly to the conservation of momentum, so the neutron gets 80 % (14.08 MeV) and the helium atom gets 20 % (3.52 MeV) of kinetic energy. In a fusion device with magnetic confinement, the helium particle remains inside the plasma and its energy is used for plasma heating; the uncharged neutron escapes the magnetic confinement in direction of the fusion plasma confining structure. The highest reaction probability of the DT reaction is at a temperature of  $T \approx 64 \text{ keV}$ , other potential fusion reactions needs even higher temperatures and have lower reaction cross-sections.

The introduction of the cylindrical coordinate system is important to understand the description of a torus shape plasma configuration. Here,  $R$  [m] is the radial coordinate measured from the reactor centre,  $\varphi$  [°] is the toroidal coordinate angle direction, and  $z$  [m] is the height, which is visualised in figure 1.2.

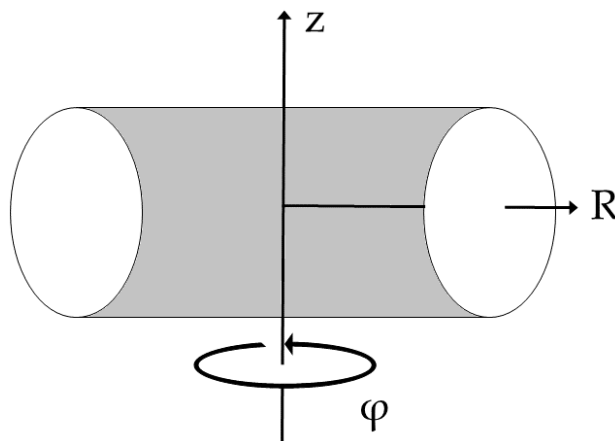


Figure 1.2: Reference curvilinear coordinate system for a torus shape configuration.

Two fusion power reactor concepts with different magnetic field coil configurations are investigated in the European fusion programme, the Tokamak and the Stellarator [Don18]. The stellarator, proposed by L. Spitzer [Spi58], and the tokamak, proposed by

soviet researchers [DS58], were the first concepts of a magnetic confined nuclear fusion plasma. Both concepts are based on the magnetic confinement of a plasma inside a torus which can be explained with the help of a simplification in figure 1.3 [Str11]. In this figure,  $\varphi$  is toroidal coordinate angle direction,  $\theta$  is the poloidal coordinate angle direction,  $z$  is the height,  $B$  is the magnetic field which is depending on  $B = \frac{B_0 R_0}{R}$  ( $B_0$  is the toroidal component of the magnetic field in direction to  $R_0$ ),  $R_0$  is the major plasma radius,  $R$  is the radial coordinate measured from the reactor centre,  $r$  is the radial coordinate of the closed flux surfaces,  $a$  is the minor plasma radius inside the torus, and  $\nabla p$  is the kinetic pressure difference inside the plasma [Str11].

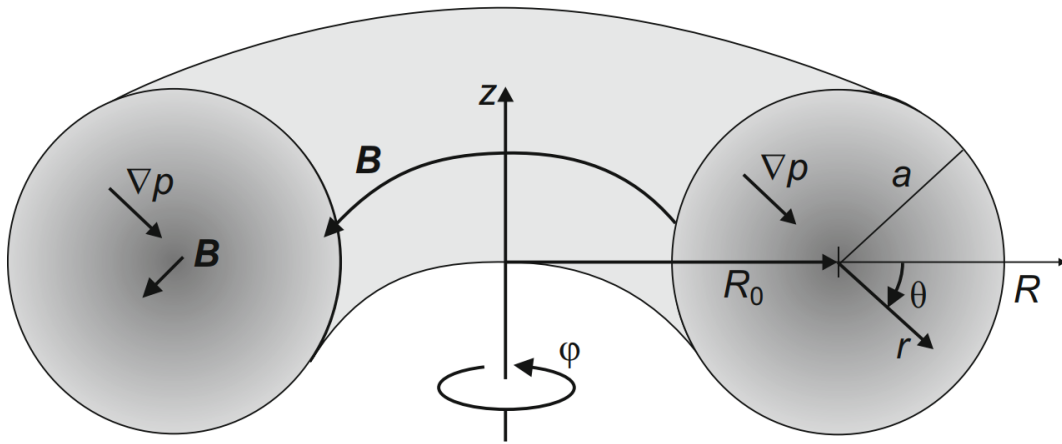


Figure 1.3: Geometry of a simple magnetised torus with constant parameters in toroidal direction ( $\varphi$ ). The pressure is highest on the torus axis which leads to a pressure gradient in radial direction ( $R$ ) [Str11].

Aim of a power reactor is to provide more output energy than needed to operate the reactor and its auxiliary systems. The fusion energy gain factor  $Q$  describes the ratio between  $P_{fusion}$  as the power being released by the fusion reactions inside the reactor, and  $P_{heating}$  as the constant heating power being supplied to the plasma:  $Q = \frac{P_{fusion}}{P_{heating}}$  [Str11]. This factor is very important for a fusion power reactor, nevertheless the presented simple relation does not take any losses (e.g. radiation and/or heat losses) into account. That means, the factor must be much larger than one to obtain self-heating from the fusion products, which is relevant for a commercial reactor concept to produce electrical energy. One aim of the International Thermonuclear Experimental Reactor (ITER) is to achieve a  $Q \geq 10$  for 400 s to ‘produce and study an inductively-driven plasma’ [Gre03].

A poloidal cross-section of ITER in figure 1.4 [Sta10] shows structural components like the central solenoid (CS), poloidal field coil (PF), toroidal field coil (TF), divertor (DI), and the space for the modular breeding blankets (BB), which are used in ITER



only for shielding and not for breeding, surrounding the plasma [Kau13]. Components like the breeding blanket or the divertor are also used in the stellarator, as well as the structural materials like low activation steel.

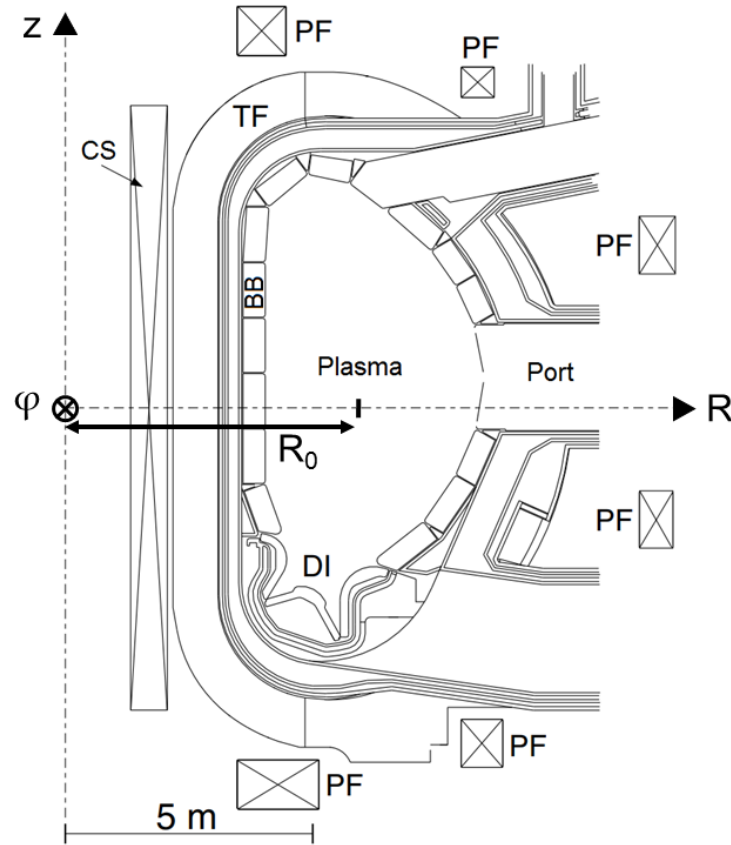


Figure 1.4: Poloidal cross-section of ITER including structural components which are: CS: Central Solenoid, PF: Poloidal Field Coil, TF: Toroidal Field Coil, DI: Divertor, BB: Breeding Blanket; [Kau13], edited.

A major difference between tokamak and stellarator reactor concepts is the way to achieve the magnetic confinement and the resulting shape of the confined plasma. A sketch of the ITER tokamak magnetic field lines is shown in figure 1.5 which is generated by a set of the toroidal and poloidal field coils. This results in an elliptic-axisymmetric plasma shape and an azimuthal (toroidal) symmetric reactor geometry. In order to confine the plasma, a helical magnetic field is required to overcome basic drifts which can be achieved by inducing a current in the plasma [Gre03]. The tokamak reactor thus needs to be operated in pulsed mode because the central solenoid interacts as a transformer to induce the current inside the plasma.

A sketch of Wendelstein 7-AS, which is the precursor of Wendelstein 7-X (W7-X), is shown in figure 1.6. The stellarator confines the plasma by a steady magnetic field, which is only generated by several specifically designed, non-planar magnetic field coils

[Alk05]. Thus, no electric current is induced inside the plasma. Due to the usage of non-planar field coils, the reactor has a discrete rotational symmetry that is given by the number of field periods, e.g. a five field periodicity. In theory, the stellarator is designed for a steady-state plasma operation. The plasma shape changes within a half-field period from bean shape ( $\varphi = 0^\circ$ ) to triangular shape ( $\varphi = 36^\circ$ ), which can be seen in figure 1.6.

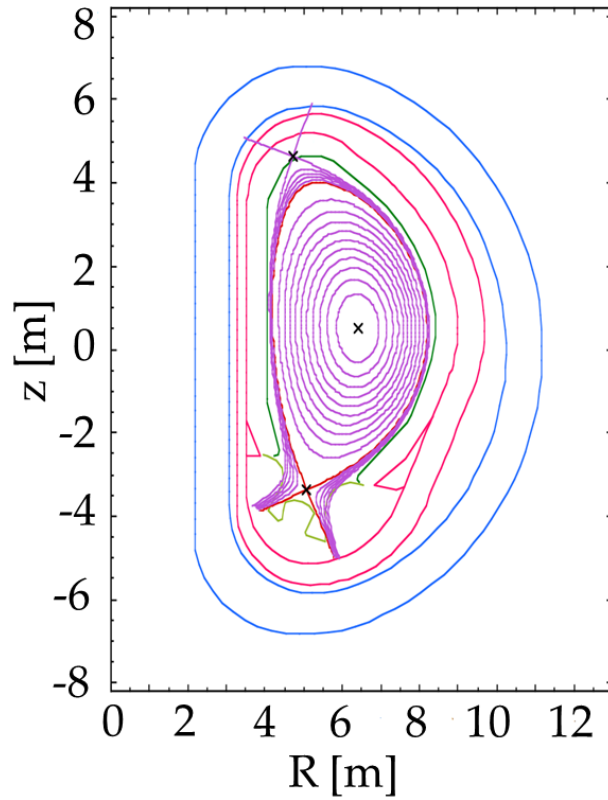


Figure 1.5: Poloidal cross-section of the ITER magnetic field (purple) including firstwall (dark green), breeding blanket / shielding (red), toroidal field coil (blue) and divertor (light green); [INT02], edited.

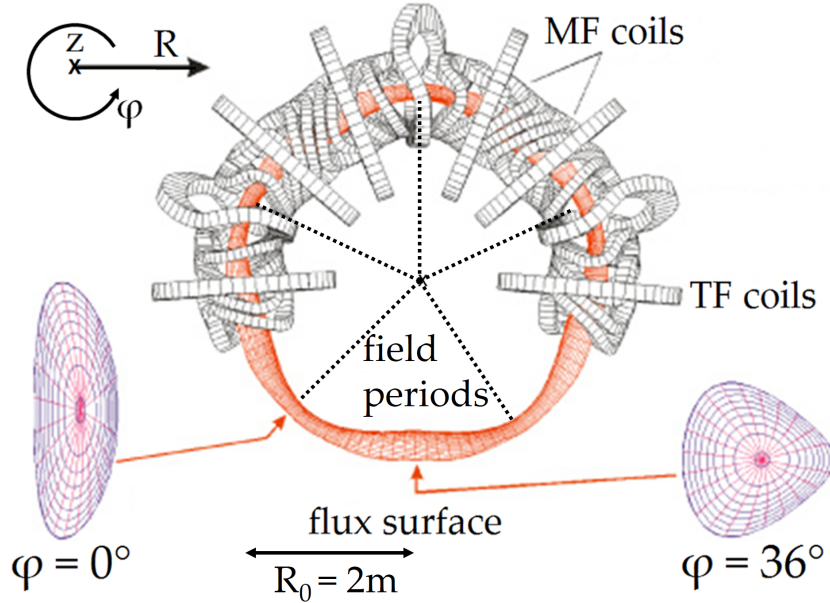


Figure 1.6: Top view of an outside flux surface (red) of the Wendelstein 7-AS, a five field period stellarator with a major radius of  $R_0 = 2\text{ m}$  and an average plasma radius of  $\leq 18\text{ cm}$ , together with a part of the magnetic field (MF) and toroidal field (TF) coils. The transformation of the plasma from bean shape ( $\varphi = 0^\circ$ ) to triangular shape ( $\varphi = 36^\circ$ ) within a half field period is highlighted; [Hir08], edited.

## 1.2 HELIAS 5-B conceptual design

The HELIAS concept is the result of a design study of a stellarator power reactor at the IPP in Greifswald [Sch13]. The idea behind this study is to develop an integrated concept of a fusion power reactor with a minimum of assumptions on plasma performance and future technical innovations [Igi06]. The optimisation of the stellarator line used several criteria like sufficient flux surfaces of the magnetic field; sufficient particle and energy confinement; and the feasibility of the modular coil set to obtain a realistic curvature [Gri92] [War17]. These criteria are physics based and presently known from stellarator experiments, which means that the physics of the reactor should stay within known limits. The same can be applied to the magnetic field, which should be as small as possible to allow for mechanically feasible designs. As an additional criterion, the reactor size should be large enough to accommodate a blanket and a shield between plasma and magnetic coils with total thickness of 1.3 m and to allow a self-sustained plasma burn within presently known laws of confinement [Igi06]. HELIAS 5-B is an up-scaled specific 5-field period power reactor design of the W7-X, using Deuterium-Tritium plasma fuel and designed for a fusion power of 3000 MW [Sch13]. Beside the HELIAS 5-B design, different studies with 4-field and 3-field periods exist [Igi06].

Figure 1.7 shows a 3D view of HELIAS 5-B with the plasma vessel surrounded by

the magnet system and the outer vessel. The non-planar field coils and the resulting 3D shape of the plasma vessel can be seen as well. Some important design parameters underlying this study are presented in table 1.1 for the HELIAS 5-B.

Table 1.1: Selected design parameters of the HELIAS 5-B reactor. Complete table in [Sch13] and [Igi06].

|                                 | HELIAS 5-B |
|---------------------------------|------------|
| Major radius [m]                | 22         |
| Average minor radius [m]        | 1.8        |
| Plasma volume [m <sup>3</sup> ] | 1407       |
| Average field on axis [T]       | 5.9        |
| Maximum field on coil [T]       | 12.5       |
| Number of coils                 | 50         |
| Fusion power [MW]               | 3000       |

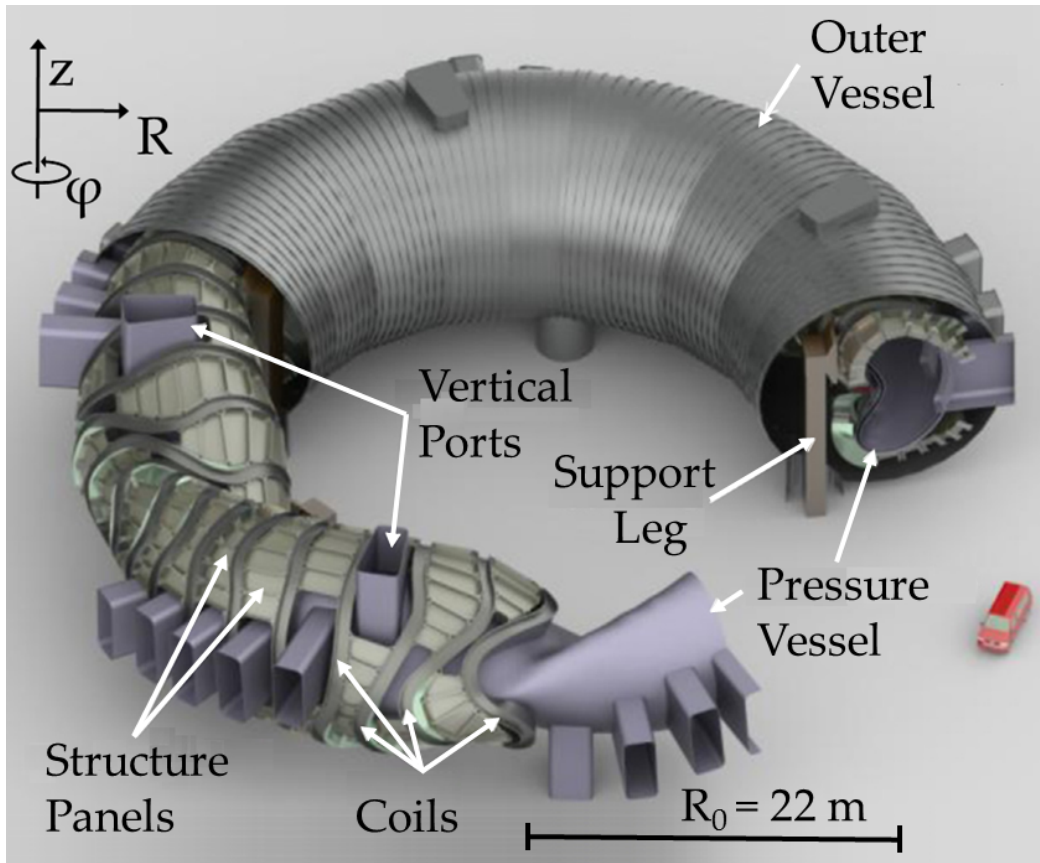


Figure 1.7: 3D view of the HELIAS 5-B power reactor including the plasma vessel, the magnetic system with five different non-planar field coils, the port openings, the supporting structure and the outer vessel; [Sch13], edited.

## 1.3 Current stellarator research status

The prime example in Europe for a stellarator is the Wendelstein 7-X (W7-X) located at IPP in Greifswald, Germany. The first plasma of this machine has been ignited in December 2015 and the reactor shows very good results between the calculated magnetic field and its measurements with only small deviations [Ped16]. The W7-X is an optimised stellarator designed for steady state operation and to demonstrate the basic capabilities of a stellarator power reactor [Wol10]. Further optimisation of stellarators have to include both physics and engineering solutions that are not taken into account during W7-X optimisation [Wol10].

A part of the European Union (EU) fusion programme is to bring the stellarator to maturity as a possible long-term alternative to tokamaks [Don18]. The European programme will ‘focus primarily on the optimised HELIAS line’ [Don18] and the work on ‘other stellarator lines (e.g., Heliotrons and compact stellarators) will continue as part of national programmes or in the frame of international collaborations’ [Don18]. The work in the EU fusion programme focuses in the first phase on the W7-X and its scientific exploitation. The ‘next-step HELIAS burning plasma experimental device’ is not yet defined and the ‘goal of such a device can be decided only after a proper assessment of the Wendelstein 7-X’ [Don18]. Concepts for different sizes between an ITER-like stellarator and a full power plant stellarator exist [War17], whereas the power plant must be optimised for generating electricity, including its remote maintenance capabilities and a specific breeding blanket concept [War17].

The flexible heliac TJ-II installed at ‘Centro para Investigaciones Energéticas, Medioambientales y Tecnológicas (CIEMAT)’, Spain, is a four period, low magnetic field stellarator and designed to have a high degree of magnetic confinement configuration flexibility [Ale01]. It is the second largest stellarator experiment in Europe, after W7-X. This stellarator is a physics experiment to study different fusion plasmas, e.g. helium and hydrogen plasma, including phenomena in particle control, configuration effects, and particle transport [Ale01]. The TJ-II allows the investigation of the effects of 3D geometry inside a stellarator, e.g the neoclassical transport, which have an impact on particle fuelling and impurity transport [Cas17].

Beside the European stellarator research activities, this topic is subject of worldwide investigation. An example is the Large Helical Device (LHD) experimental reactor, located at the ‘National Institute for Fusion Science (NIFS)’, Japan, ignited its first plasma in 1998 [Iiy99] and is still in operation.

The fusion research activities in the United States, presented in [Gat18], encompass

a research outline for stellarator related activities. It is represented by a collaboration on W7-X as well in the statement ‘Strengthening our partnerships with international research facilities’ [Gat18], which also includes collaborations for the tokamak ITER. Computational tools for neutronic investigations of complex fusion systems are also part of the US fusion research [Saw09]. Such specifically developed tools are needed to represent the complex 3D shape of a stellarator in the code, and ensure the adequate and error-free theoretical outcome.

## 1.4 Objective and Purpose

The thesis represents a contribution to the European fusion research programme to bring the stellarator to maturity. The ‘optimisation of a HELIAS reactor is still on the stage of initial exploration of reactor physics and engineering options’ [Igi06]. The objective of the first comprehensive neutronics investigation of the stellarator power reactor HELIAS is to develop a stellarator specific neutronics approach to provide input required for the engineering reactor design especially for the in-vessel components.

The neutronic investigations require input for the neutron source and the geometry model to obtain reliable results. These requirements lead to the targets of the thesis, which are:

**The development of a consistent neutron source:** The neutron source is a self-developed, user specific MCNP source subroutine which processes a neutron distribution, based on plasma physics calculations, to provide the spatial representation of the neutrons in the simulation. The development and verification is described, it ensures a faithful representation of the plasma source for neutron transport simulations.

**The consistent verified neutronic model development:** The target is to identify the most reliable approach to execute an enveloping nuclear analysis, which simultaneously is not suffering from geometry limitations. Therefore, the development and verification of a neutronic model with as few restrictions as possible is very important. The complicated Computer-Aided Design (CAD) geometry of HELIAS consists only of higher-order surfaces to describe the stellarator. An easy transfer of this geometry into a neutronics model is a challenging task due to the inherent limitations of particle tracking through complex boundary surfaces. Three different CAD to neutronics geometry approaches are investigated

and verified to determine the most suitable approach for the nuclear analysis of HELIAS.

**The first closed nuclear analysis of the plasma facing reactor components:**

The nuclear analysis encompasses the provision and quantification of important design parameters as NWL, neutron flux, TBR and radiation shielding. The design parameters are needed as an input for the iterative development of the HELIAS design, like the development of a stellarator specific breeding blanket or the improvement of the shielding capabilities.

Based on the targets, the subsequent logic of the thesis has been developed:

- Chapter 2 gives an overview about fusion neutronics, the Monte Carlo method based particle transport code MCNP and the breeding blanket concept from neutronics point of view.
- Chapter 3 presents the used geometry models in this work and their transfer into a nuclear physics representation.
- Chapter 4 covers the generation and verification of a simplified MCNP geometry model with three different geometry transfer approaches to find the most suited for applying to the HELIAS stellarator geometry.
- Chapter 5 presents the development and verification of a stellarator neutron source for MCNP, based on plasma physics simulations.
- Chapter 6 reflects a comparison between two techniques to improve the statistical error in the particle transport calculations, and their suitability to application for the stellarator investigations.
- Chapter 7 reports the nuclear analysis results obtained for HELIAS including a shielding analysis in a specific area with increased NWL and low material thickness.
- Chapter 8 summarises the major results and formulates research tasks based on the obtained results of the thesis.

# Chapter 2

## Fusion Neutronics, Monte Carlo Method and Breeding Blanket Concept

The chapter gives a principle overview about the theoretical background of the thesis. It consists out of neutron induced interaction with matter, a short description of the Monte Carlo (MC) method and their application in fusion neutronics, and material specifications including the breeding blanket concept for the application to HELIAS.

### 2.1 Neutrons and their interaction with matter

Neutrons are, beside protons, components of the atomic nuclei. They are naturally bound in the nucleus and can be released by fusion, fission or spontaneous decay reaction of the nucleus. Single neutrons ( $n$ ) are uncharged and unstable with a mean life of around 880s and a half-life of around 610s. Their radioactive decay is into a proton ( $p$ ), electron ( $e^-$ ) and anti-neutrino ( $\bar{\nu}_e$ ) including a release of energy in form of a gamma ray which is shown in equation 2.1 [Bet08]:



Neutrons and their interaction with matter play a key role in fusion technology, because they are generated in the D-T fusion reaction. When a beam of particles impinges upon a nucleus, the ratio of the reaction rate to the incident flux is defined as the ‘nuclear cross-section’ (in units of  $\text{cm}^2$  or barn with  $1 \text{ b} = 10^{-24} \text{ cm}^2$ ) [Cac10]. It is a virtual surface area which represents the potential hit area between the particle



with an initial energy and the nucleus. This context can be explained in figure 2.1, where the particle current  $j$  impinges on an infinitesimal volume element, filled with matter, with the thickness  $d$  and the surface area  $F$ , is shown.

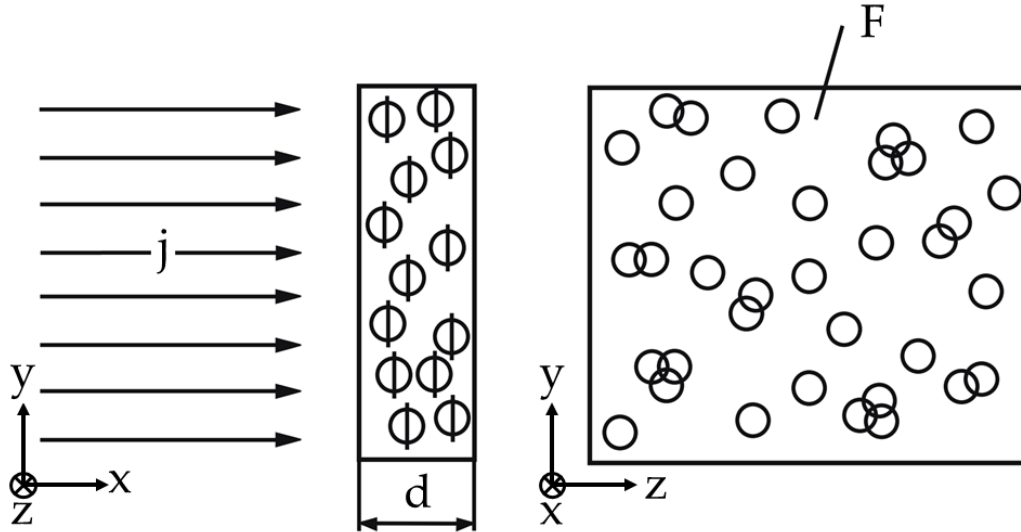


Figure 2.1: Schematic representation of the nuclear cross-section, where the particle current  $j$  impinges on an infinitesimal matter volume element with thickness  $d$  and surface area  $F$ , in side and front view [Bet08].

The nuclear cross-section (b) characterises the probability that a nuclear reaction will occur between projectile and target atom [Bet08]. Thus it can be described in equation 2.2 [Bet08]:

$$N = n \cdot j \cdot \sigma, \quad (2.2)$$

where  $j$  is the particle current in  $\text{s}^{-1}$  on surface  $F$  in  $\text{m}^2$ ,  $n$  are the target particles as number of particles per area in  $\text{m}^{-2}$ ,  $N$  is the reaction yield in  $\text{s}^{-1}$  and  $\sigma$  as nuclear cross section in  $\text{m}^2$ . If the material with the surface area  $F$  has an infinitesimal thickness  $d$ , the projection surface of each particle can be assumed to be spherical. The probability for a hit of a particle is  $\propto n \cdot \sigma / F$ , where the target atoms do not overlap [Bet08]. Therefore, the nuclear cross-section is a measure of the strength of the reaction which can be described as reaction rate in equation 2.3 [Cac10]:

$$N_i = N_v \cdot \sigma \cdot \varphi_n. \quad (2.3)$$

$N_i$  is the number of interactions occurring in  $\text{cm}^{-3} \text{s}^{-1}$ ,  $N_v$  is the number of atoms that could interact in the unit volume in  $\text{atoms}/\text{cm}^3$ ,  $\sigma$  is the microscopic cross-section in  $\text{cm}^2$ , and  $\varphi_n$  is the neutron flux in  $\text{cm}^{-2} \text{s}^{-1}$ .

The microscopic cross-section can be transformed to  $\Sigma$ , which is the macroscopic cross-section in  $\text{cm}^{-1}$ . The macroscopic cross-section describes the total hit area as a product of the microscopic cross-section and the nucleus number density presented in equation 2.4:

$$\Sigma = N_v \cdot \sigma(E). \quad (2.4)$$

This means that the macroscopic cross-section returns as quantity of how many interactions between particle per track length covered occur [Zie13]. This relationship can be used to describe the mean free path  $\lambda$  in equation 2.5, which is the average travel distance of a particle in matter:

$$\lambda = \frac{1}{\Sigma}. \quad (2.5)$$

Each interaction of neutrons with matter lead to a decreasing flux, which can be described by the Beer-Lambert attenuation law of the particle flux  $I$ :

$$I = I_0 \cdot e^{-\Sigma \cdot x}, \quad (2.6)$$

where  $I_0$  is the original neutron flux intensity and  $x$  the path length in material. Interaction in this sense mean a nuclear reaction which depends on the material, the particle type and its corresponding energy. Possible reactions are particle scattering, e.g. elastic and inelastic scattering, and particle absorption, e.g. fission, capture or particle emission [Zie13]. The reactions and their probabilities are stored as microscopic cross-sections in nuclear data files, like the Joint Evaluated Fission and Fusion File (JEFF) nuclear data library. This library is used in the present work in version 3.2 [JEF14], because it is the reference nuclear cross-section library for the EU Demonstration Fusion Power Reactor (DEMO) tokamak neutronic simulations.

Fusion neutrons are released with an energy of  $\sim 14.1$  MeV. Slowing down of neutrons via elastic scattering to atomic nucleus means that the neutrons transfer a part of their kinetic energy and get decelerated, which is called moderation of neutrons. This effect happens until the mean speed of the neutrons is in equilibrium to the thermal oscillation of the surrounding material atoms, and the neutrons now get the name ‘thermal neutrons’ [Zie13]. To reach this state of neutrons, a material with a low atomic number is preferred and hydrogen is one of the best neutron moderators, because a hydrogen atom is built with one proton and one electron. The proton in the nucleus, where the interaction takes place, and the neutron have nearly the same atomic mass with  $\sim 1$  u, whereas the electron has a mass of  $\sim 5 \times 10^{-4}$  u. The elastic

scattering of two particles with a comparable mass results in the largest quantity of energy transfer between both.

The energy of neutrons has an important influence on the interaction they undergo with matter, because the material cross-sections depend on the impinging neutron energy. This relation can be derived from equation 2.3 that leads to equation 2.7.  $\sigma(E)$  describes the energy dependent neutron cross-section and  $\varphi_n(E)$  the neutron flux in the energy range covered:

$$N_i(E) = N_v \cdot \sigma(E) \cdot \varphi_n(E). \quad (2.7)$$

A subdivision into three different neutron energy groups simplifies the representation and can be done in table 2.1. The context of this table can be visualised in figure 2.2 using a selection of nuclear fusion relevant nuclides which can be explained:

- $^{56}_{26}\text{Fe}$ : Iron is part of all structural components in a fusion reactor and  $^{56}\text{Fe}$  is the most common nuclide in natural iron,
- $^6_3\text{Li}$  and  $^7_3\text{Li}$ : Lithium is essential in a fusion power reactor for tritium production,
- $^9_4\text{Be}$ : Beryllium is a possible neutron multiplier material inside a breeding blanket.

Table 2.1: Categorisation of the neutrons in fusion neutronics by their energy [Zie13].

| NEUTRON ENERGY                                | CLASSIFICATION |
|---|----------------|
| $< \sim 10^1 \text{ eV}$                      | thermal        |
| $\sim 10^1 \text{ eV} - \sim 10^5 \text{ eV}$ | epithermal     |
| $> \sim 10^5 \text{ MeV}$                     | fast           |

If the reaction between a neutron and a nucleus does not need a threshold energy, then all three classifications from table 2.1 can be found in the cross-section behaviour between both reactants. Usually, the thermal range shows a nearly  $\frac{1}{v}$  behaviour, where  $v$  denotes the neutron speed. This means that the cross-section increases with lower neutron energy [Zie13]. This behaviour can be seen in figure 2.2 for the isotopes  $^{56}_{26}\text{Fe}$  and  $^6_3\text{Li}$ .

The epithermal range, also called resonance range, is characterised by large resonances of the nuclear cross-section which occur due to the absorption of neutrons and the related excitation. Each nucleus has discrete energy levels, which can be seen for  $^{56}_{26}\text{Fe}$ . If the sum of the binding energy of the neutron and its kinetic energy, dependent to the relative speed, correspond to such an energy level, the probability for a

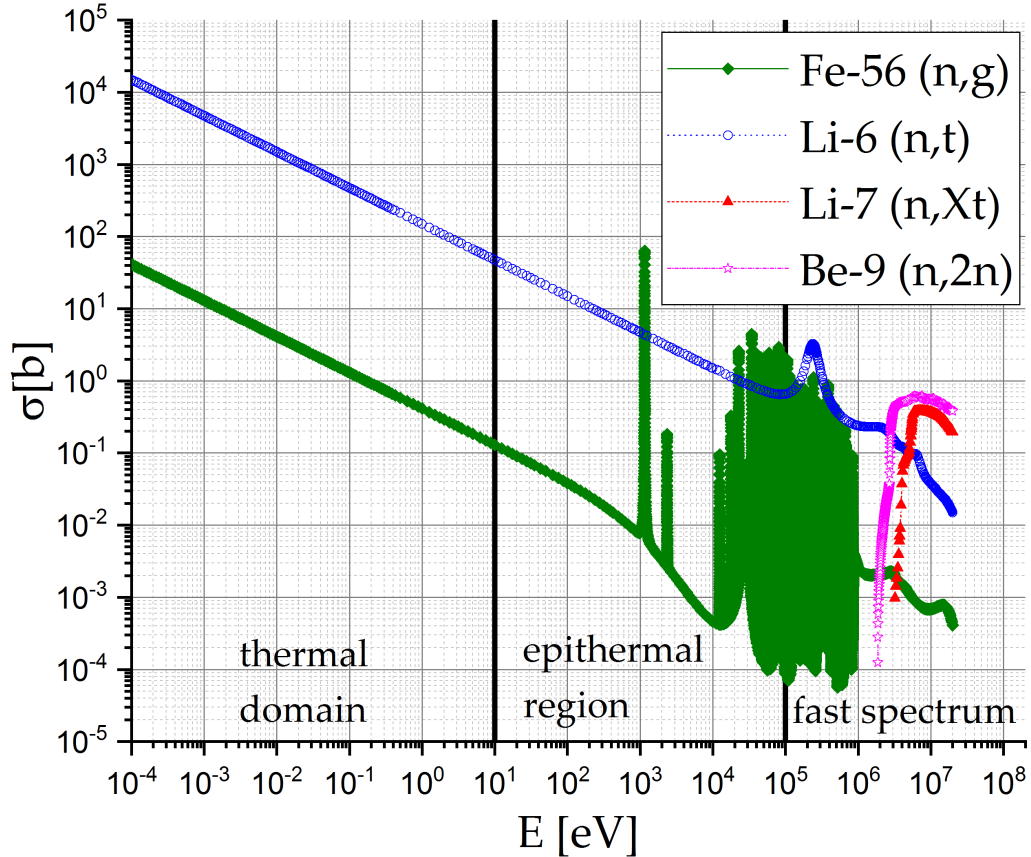


Figure 2.2: Typical neutron-induced cross-sections, from the JEFF 3.2 [JEF14] nuclear data library, for fusion relevant nuclide over an energy range from  $10^{-4}$  to  $10^8$  eV.

absorption reaction increases rapidly [Zie13]. This means that the probability for such an effect is higher at higher neutron energies, while the lower resonance goes smoothly into the  $\frac{1}{v}$  regime [Zie13]. The epithermal range is the smallest range compared to the two other energy ranges in table 2.1.

The fast range, with higher neutron energies above the resonance range, shows a decreasing reaction cross-section if not a threshold energy for the reaction is required. If it is a threshold reaction which requires a minimum neutron energy, like  ${}^7_3\text{Li}$  and  ${}^9_4\text{Be}$ , the behaviour is different. Inelastic scattering can occur for neutron energies above 10 keV, which is nuclide dependent. In an inelastic scattering, the neutron gets absorbed by the nucleus and particles, often neutrons, will be emitted after a certain amount of time from the excited nucleus. A small part of the neutron energy is transferred during the inelastic scattering from the excited nucleus to the emitted neutrons as kinetic energy, whilst the excitation energy is emitted by photons [Zie13].

## 2.2 Monte Carlo method

The Monte Carlo (MC) method is a technique of numerical analysis based on the use of sequences of random numbers to obtain sample values for the problem variables [Dup02]. The sample values for the problem variables are obtained by selecting specific numbers from probability distributions. The desired solution can be obtained, along with estimates of uncertainties, by analysing the results from the sample values. The sample evaluation in a Monte Carlo calculation is considerable equivalent to conducting an experiment. Both, an experiment and a Monte Carlo calculation yield a result that is a possible, or representative, outcome of the process being modelled, and both contain uncertainties that can often be reduced by repeated measurements and quantified by the use of statistical analysis [Dup02].

### 2.2.1 Fundamental Monte Carlo laws

The Monte Carlo method is based on three fundamental laws [Dup02]:

**The Strong Law of Large Numbers** The law represents a connection between the relative frequency of a random event and its probability at a large number of repetitions. It describes that the result of performing the same experiment a large number of times, the average of the result obtained from a large number of trials should be close to the expected value, and will tend to become closer as more trials are performed.

**The Central Limit Theorem** The law states that the distribution of a large number of independent random numbers trends to a normal distribution, even if the independent random numbers are not normally distributed. The normal distribution has a variance of  $\sigma^2$  that is proportional to  $1/n$ , where  $n$  is the total number of random numbers.

**The Conservation of Weight** The law describes that every performed random experiment gives the same weighting to the end result. Every random experiment can be split into several experiments, but the sum of the weightings of the split experiments must be equal to the weighting of the original experiment.

A simple example to demonstrate the Monte Carlo Method is the simulation of  $\pi$ . The experiment takes the unit square which includes the a circle with radius  $r = 0.5$  cm, where  $A_{circle}$  is the surface of the circle. To simplify this consideration, only a quarter of the whole scenario is investigated. The idea is to randomly shoot particles on the

unit square, either registered in the circle or not. The relation can be expressed by equation 2.8:

$$\pi = A_{circle} = 4 \times \lim_{N \rightarrow \infty} \frac{\text{hits in circle "n"}}{\text{total number of tries "N"}}. \quad (2.8)$$

The equation 2.8 is visualised in figure 2.3 by a quarter circle with the radius  $r = 0.5$  cm. In this example,  $N = 4000$  particles hit the unit square and  $n = 3125$  particles hit inside the circle. The simulation of  $\pi$  in this example comes to  $\pi \approx 3.125$  which is with a deviation of  $\sim 0.016$  close to the value of  $\pi \approx 3.141$ .

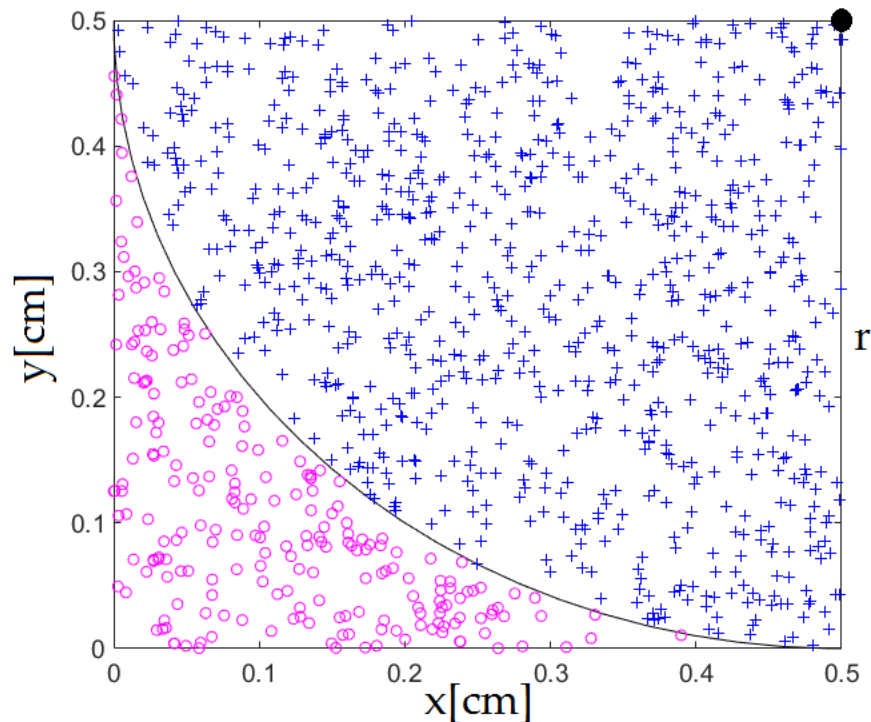


Figure 2.3: Approximation of  $\pi$  with a simple example to shoot particles on a unit square which includes a circle with  $r = 0.5$  cm, where blue crosses are hits inside the circle and magenta circles are hits outside the circle.

### 2.2.2 Monte Carlo neutron transport simulation

An important application of the MC technique is the transport of particles, like neutrons and photons, associated with atomic and nuclear processes [Dup02]. The neutron can be defined by its location  $r$ , its direction of travel  $\Omega$ , and its Energy  $E$  at time  $t$  [Dup02]. This information, apart from the time, describes the particle and its trajectory fully inside the simulation. The MC method models the particle flight paths and the various reactions between neutrons and material to solve the neutron

transport problem. The neutron path simulation is also known as random walk which involves the evaluation of random variables associated with the physical processes of neutron transport [Dup02]. This produces a set of particle collision points along with information about the consequences of these collisions, like neutron scattering or secondary particle production. Each particle trajectory is a mathematical realisation of one of the physically possible paths that a neutron could follow through the material. In a well-defined problem, with a large number of random walks calculated by MC simulation, the result tend to those of an analogous physical measurement [Dup02].

The individual probabilistic events that comprise a process are simulated sequentially. The probability distributions governing these events are statistically sampled to describe the total phenomenon. In MC simulation a large number of particles are necessary to track, because this process is based on the selection of random numbers, it must be statistically representative and the sampling range should cover all intervals of the variables of the physical phenomenon [MCN03]. This means that MC sampling should be systematically correct in addition to the statistical adequacy. Results of the Monte Carlo technique are pre-eminently realistic, because it is a numerical experiment. All particles which take place in a simulation are simulated autonomously, for each from birth throughout its life to its death (e.g. absorption, leakage, escape, etc.). Probability distributions are randomly sampled using transport data to determine the outcome at each step of its life [MCN03].

## 2.3 Monte Carlo particle transport code MCNP

The steps presented for the general Monte Carlo method are now adapted to the computer code MCNP. The sub-chapter 2.3 is based on the manuals of MCNP 5 [MCN03], MCNP 6 [Goo12] and MCNP 6.1.1beta [Goo14].

MCNP is a general-purpose **M**onte **C**arlo **N**-**P**article code which can perform coupled neutron/photon/electron particle transport simulations, developed at Los Alamos National Laboratory (LANL), USA. The code is able to treat an arbitrary three-dimensional configuration of material cells in geometric cells bounded by first-, and second-degree surfaces, and fourth-degree elliptical tori.

In the particle transport simulation with MCNP, an adequate input file is necessary which will be read and processed during the simulation. This file contains the following information:

- the geometry definition,

- the description of materials and selection of cross-section evaluations,
- the location and characteristics of the particle (neutron, photon, electron, or others) source,
- the type of answers or tallies desired, and
- any variance reduction techniques used to improve efficiency.

The output file contains tables of standard summary information to give a better understanding of how the problem ran. This information gives insight into the physics of the problem and the adequacy of the MC simulation.

An example of a random particle history of an incident neutron into fissionable material is presented in figure 2.4. Random numbers in the interval  $[0, 1)$  are generated in MCNP to determine what, if any, and where interaction takes place, based on physics rules and transport data probabilities governing the processes and materials involved. The example in figure 2.4 shows at position 1 a neutron scatter, which has been randomly selected from the physical scattering distribution. A photon (dotted line) is produced and temporarily stored for later analysis. At position 2, a fission event occurs which means that the incoming neutron will be terminated, two neutrons and one photon will be created at this event in which one neutron and the photon will be stored. The first fission neutron will be captured at point 3 and terminated. The stored neutron undergoes a random sampling and leaks out of the geometry at position 4. The stored photon has a scattering event at position 5 and leaks out at position 6. One photon is remaining in the storage from event 1 and this will have a capture event at position 7 and gets terminated. The order of stored particles in MCNP is: the last particle which is stored is the first particle taken out. This exemplary neutron history is now complete.

### 2.3.1 Computational geometry definition

The traditional geometry approach to depict a domain in Monte Carlo methods is the so-called Constructive Solid Geometry (CSG) approach. It defines the geometry with Boolean algebra by a combination of intersections, unions, and complements, where all the regions are bounded by surfaces. In the meantime, different approaches are developed to enable using more complex computational geometry, like Unstructured Mesh (UM) geometry or faceted geometry with DAGMC. Nevertheless, it is important to understand the concept of the CSG definition, because the recently developed



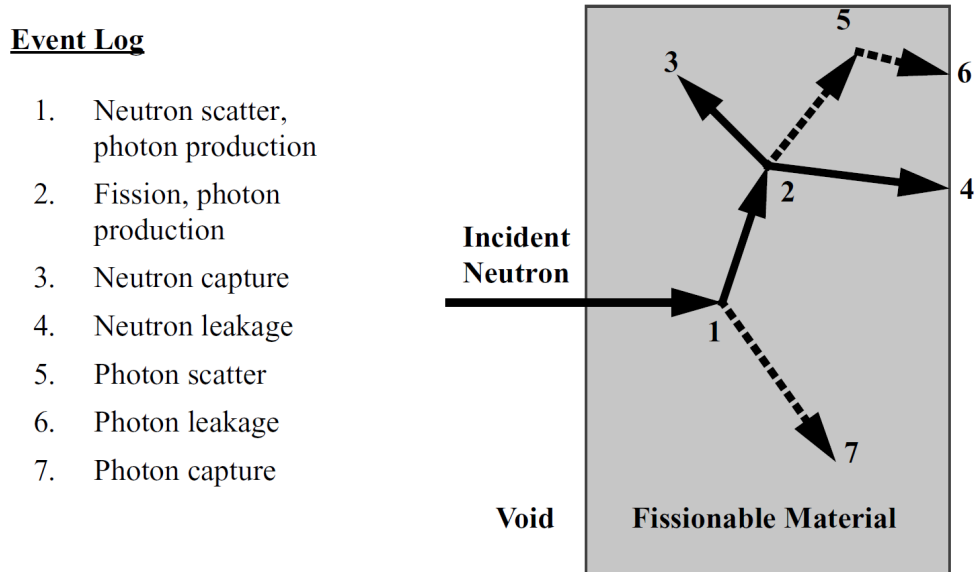


Figure 2.4: Example history, including the random walk with secondary particle production, of an incident neutron into fissionable material [MCN03].

approaches have clear similarities in geometry cell definition with the CSG approach. Surfaces are defined by supplying coefficients to the analytic surface equations or known points on the surfaces. In CSG of MCNP, allowed surface cards are the following [MCN03]:

- **Plane:** General, Normal to X-, Y-, or Z-axis.
- **Sphere:** General at Origin, General, Centered on X-, Y-, or Z-axis.
- **Cylinder:** Parallel to X-, Y-, or Z-axis, On X-, Y-, or Z-axis.
- **Cone:** Parallel to X-, Y-, or Z-axis, On X-, Y-, or Z-axis.
- **Ellipsoid, Hyperboloid, Paraboloid:** Axis parallel to X-, Y-, or Z-axis.
- **Cylinder, Cone, Ellipsoid, Hyperboloid, Paraboloid:** Axes not parallel to X-, Y-, or Z-axis.
- **Elliptical or circular torus:** Axis is parallel to X-, Y-, or Z-axis.
- **Surfaces defined by points.**

The combination of a sort of surfaces to define cells by means of Boolean algebra is an important ability. The defined cells are called bodies which can be combined in Boolean operations to set a full defined, arbitrary geometry. Each cell can be filled with

a material, associated density and the particle importance can be set in an appropriate way. The particle importance must be set to tell the code if a specific particle type should be tracked inside the cell, and the importance can be used to apply variance reduction methods. In analogue calculations, not using variance reduction techniques, the particle importance is set to 1 everywhere, except for the outside of the calculation geometry where it is zero to terminate all particles leaving the calculation geometry.

An example geometry in figure 2.5 shows a cross-section through the centre of the geometry. The green circle, enclosed by surface number 11 to create the cell 1, is filled with void. Cell 1 is enclosed by the red box that defines cell 2 with six surfaces, from numbers 21 to 26. Cell 2 is filled with material number 158, which is iron with a density of  $7.874 \text{ g cm}^{-3}$  [McC11]. Cell 3 is a sphere that covers the whole geometry and is filled with material number 354, which is water with a density of  $0.998207 \text{ g cm}^{-3}$  [McC11]. Outside of cell 3 is cell 4 which is filled with void and defined as graveyard by setting the particle importance for neutrons/photons to zero. The MCNP geometry definition, which follows the order cell number, material, surface number and particle importance, is presented in table 2.2. In this example, material 0 is a void cell which does not require a density.

Table 2.2: Example of an MCNP geometry definition.

| CELL No. | MATERIAL ID | DENSITY   | SURFACE ID                 | IMPORTANCE |         |
|----------|-------------|-----------|----------------------------|------------|---------|
|          |             |           |                            | NEUTRON    | PHOTON  |
| 1        | 0           |           | -11                        | imp:n=1    | imp:p=1 |
| 2        | 158         | -7.874    | 11 -21 22 -23 24 -25 26    | imp:n=1    | imp:p=1 |
| 3        | 354         | -0.998207 | -31 (21:-22:23:-24:25:-26) | imp:n=1    | imp:p=1 |
| 4        | 0           |           | 31                         | imp:n=0    | imp:p=0 |

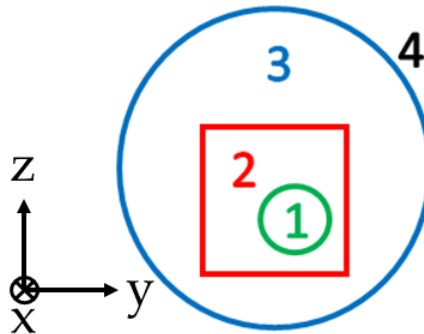


Figure 2.5: 2-dimensional example of an MCNP geometry, cell numbers are colour matching to their enclosing surfaces and the geometry definition is presented in table 2.2.

Specific boundary conditions for surfaces can be set in MCNP, like reflecting bound-

aries. This means that an impinging particle is reflected on such a surface as on a mirror. The usage of this surface function can simplify the geometry set-up, as it only needs to be defined as a representative volume including reflecting boundary conditions. In a fusion reactor simulation, like for the ITER tokamak, a  $40^\circ$  toroidal sector is considered to the leading order as to be representative. It looks like a piece of cake, while the reflecting surfaces are both at the toroidal sides of the reactor chamber to symmetrically duplicate 9 times the  $40^\circ$  toroidal sector and reproducing a whole  $360^\circ$  torus. This ability reduces the amount of specified MCNP geometry and accelerates the particle tracking significantly.

The defined geometry must be checked, which can be done by the user by plotting it with the MCNP geometry plotter or by executing an MCNP run that checks the geometry each time during the input file reading. If the geometry is ill-defined, which means it includes e.g. overlapping surfaces or undefined space, lost particles can occur during the simulation. MCNP checks, during the particle tracking, at each cell boundary if this boundary is defined correctly and continues the particle transport, or if an ill-defined geometry region is reached and lost particles occur. A lost particle is a particle which does not know where it is inside the geometry, and it will be terminated by MCNP in the simulation. The whole particle track, all interactions and secondary particles, will be erased, too. This means that a lost particle does not contribute to the result of the calculation. Therefore, it is very important to define the geometry as good as possible to prevent lost particles.

### 2.3.2 Tally definition

MCNP allows the definition of various tallies related to particle current, particle flux, and energy deposition. All MCNP tallies are normalised per starting particles with a few exceptions for criticality sources. Tallies are typically defined on surfaces / surface segments / sum of surfaces or for cells / cell segments / sum of cells. The mesh tally detects fluxes in a mesh superimposed to the problem geometry. A short overview of the available tallies in MCNP is presented in table 2.3. Around 100 standard Evaluated Nuclear Data Format (ENDF) reactions plus several non-standard ones can be detected by tallies. The tally results in the output file are printed with their statistical relative errors corresponding to one standard deviation. After that MCNP prints results of 10 statistical checks for the estimated answer for the Tally Fluctuation Chart (TFC). The detailed analysis of TFC allows judgement of the precision of the tally and to define its confidence interval. The TFC are automatically printed to show how a tally mean,

error, variance of the variance, and slope of the largest history scores fluctuate as a function of the number of histories run. All tally results, except for mesh tallies, can be displayed graphically, either while the code is running or in a separate post-processing mode.

Table 2.3: Short overview of the in MCNP available tallies [MCN03].

| TALLY     | DESCRIPTION  | UNIT                      |
|-----------|--|---------------------------|
| F1        | Surface current                                    | particles                 |
| F2        | Surface flux                                       | particles/cm <sup>2</sup> |
| F4/FMESH4 | Track length estimate of cell flux                 | particles/cm <sup>2</sup> |
| F5        | Flux at a point or ring detector                   | particles/cm <sup>2</sup> |
| F6        | Track length estimate of energy deposition         | MeV g <sup>-1</sup>       |
| F7        | Track length estimate of fission energy deposition | MeV g <sup>-1</sup>       |
| F8        | Pulse height tally                                 | pulses                    |

Tallies must be defined by particle, either neutrons, photons or electrons, despite not all tallies are available for each particle type. If an asterisk is added in the tally definition (\*Fn, where n is the tally number), the tally changes into an energy tally and multiplies by a specific factor to each tally. Thus e.g. the energy flux instead of the particle flux through a surface can be detected without specifying extra ‘FM’ tally multiplication cards.

The mesh tally FMESH4 has the advantage that a superimposed mesh overlay the 3D calculation geometry. The mesh grid can be adjusted in size individually, therefore a detailed resolution in the area of interest is possible, independently from the geometry cells description. Each mesh element is calculated in the same way as a regular F4 tally, which can be seen in equation 2.9:

$$F4 = \frac{1}{V} \int_V dV \int_E dE \int_{4\pi} d\Omega \phi(r, E, \Omega). \quad (2.9)$$

In equation 2.9, V is the volume (cm<sup>3</sup>), E the energy (MeV),  $\Omega$  the direction vector, and  $\phi(r, E, \Omega)$  the energy and angular distribution of the fluence as a function of the position. The term  $\frac{1}{V}$  indicates an averaged result for each mesh cell volume.

### 2.3.3 Estimation of Monte Carlo Errors

Monte Carlo results represent an average of the contribution from many histories sampled during the course of the problem execution. An important quantity equal in importance to the Monte Carlo answer, or tally, itself is the statistical error or

uncertainty associated with the result. The importance of this error and its behaviour compared to the number of histories is highlighted, because it represents on the one hand the quality of the result and on the other hand it determines if a tally behaves statistically well. If not, the tally must be redefined and the simulation must be executed again.

Monte Carlo results are generated by sampling possible random walks and assigning a score of  $x_i$  to each random walk, where  $x_i$  is equivalent to the energy deposition of the  $i^{th}$  random walk. The random walks typically produce a wide range of quantities depending on the chosen tally and variance reduction method.

Assuming that  $f(x)$  is the Probability Density Function (PDF) for selecting a random walk that scores  $x$  to the tally being estimated. Then the true answer, or mean, is the expected value of  $x$ , defined with  $E(x)$  by the formula:

$$E(x) = \int x f(x) dx = \text{true mean.} \quad (2.10)$$

The function  $f(x)$  is usually not explicitly known and  $f(x)$  needs to be implicitly sampled by the Monte Carlo random walk process. This implies that the true mean is estimated by the sample mean  $\bar{x}$  by:

$$\bar{x} = \frac{1}{N} \sum_{i=1}^N x_i, \quad (2.11)$$

where  $x_i$  is the value of  $x$  selected from  $f(x)$  for the  $i$ -th history and  $N$  is the total number of histories used in the problem. This means that  $\bar{x}$  is the average value of the scores  $x_i$  for all the histories investigated. The connection between  $E(x)$  and  $\bar{x}$  is given by the Strong Law of Large Numbers stating that if  $E(x)$  is finite then  $\bar{x}$  tends to the limit  $E(x)$  as  $N \rightarrow \infty$ .

The variance  $\sigma^2$  of the population of  $x$  values is a measure of the spread in these values and is given by:

$$\sigma^2 = \int (x - E(x))^2 f(x) dx = E(x^2) - (E(x))^2. \quad (2.12)$$

The square root of the variance is  $\sigma$ , which is called the standard deviation of the population of scores. The same as  $E(x)$ ,  $\sigma$  is usually unknown but can be estimated by Monte Carlo as  $S$ , given for large  $N$  by

$$S^2 = \frac{\sum_{i=1}^N (x_i - \bar{x})^2}{N - 1} \approx \overline{x^2} - \bar{x}^2, \quad (2.13)$$

and,

$$\overline{x^2} = \frac{1}{N} \sum_{i=1}^N x_i^2. \quad (2.14)$$

The quantity  $S$  is the estimated standard deviation of the population of  $x$  based on the values of  $x_i$  that have been sampled. The estimated variance of  $\bar{x}$  is given by:

$$S_{\bar{x}}^2 = \frac{S^2}{N}. \quad (2.15)$$

The presented formulas do not depend on the distribution of  $x$  or  $\bar{x}$  beyond requiring that  $E(x)$  and  $\sigma^2$  exist and are finite. The estimated standard deviation of the mean  $\bar{x}$  is given by  $S_{\bar{x}}$ .

An important fact is, that  $S_{\bar{x}}$  is proportional to  $1/\sqrt{N}$ , which is a constitutional drawback of the Monte Carlo method. To get the half  $S_{\bar{x}}$ , four times of the original number of histories must be calculated, which can result in a very computationally expensive calculation. The quantity  $S_{\bar{x}}$  can also be reduced for a specific  $N$  by making  $S$  smaller, reducing the inherent spread of the tally results. This can be achieved by using variance reduction techniques, which are discussed in chapter 2.3.4.

The estimation of the relative statistical error in MCNP follow these rules. Besides the relative error, several different statistical checks are performed to provide a reliable guideline to interpret the tally results, which is not discussed here.

The tallies in MCNP are normalised per starting particle history and the results printed in the output file with a second number, which is the estimated relative error  $R$ :

$$R = \frac{S_{\bar{x}}}{\bar{x}}. \quad (2.16)$$

The relative error is a convenient number, because it represents statistical precision as a fractional result with respect to the estimated mean MCNP tally result. According to the Central Limit Theorem, it presents  $1\sigma$  confidence interval with 68% chance that the true result is inside the range of  $\bar{x}(1 \pm R)$  for each tally result. In table 2.4 the guideline to interpret the relative error of each tally result within the confidence interval of  $1\sigma$  is shown. These guidelines have been determined empirically, based on a wide variety of problems.

MCNP calculates the relative error for each tally bin in the problem using equation 2.15. Each  $x_i$  is defined as the total contribution from the  $i$ -th starting particle and all resulting progeny. This definition is important in many variance reduction methods, multiplying physical processes such as  $(n, xn)$  neutron reactions that create additional

Table 2.4: Guideline for interpreting the Relative Error  $R$  within the confidence interval of  $1\sigma$  [MCN03].

| RANGE OF $R$ | QUALITY OF THE TALLY                         |
|--------------|--|
| 0.5 to 1.0   | Garbage                                      |
| 0.2 to 0.5   | Factor of a few                              |
| 0.1 to 0.2   | Questionable                                 |
| < 0.10       | Generally reliable except for point detector |
| < 0.05       | Generally reliable for point detector        |

neutrons, and many more problems. The  $i$ -th source particle and its offspring may thus contribute many times to a tally and all of these contributions are correlated because they are from the same source particle.

As shown in equation 2.15, the relative error  $R^2$  scales as  $1/N$ . The computer time  $T$  used in an MCNP calculation correlates proportional to  $N$ , which means that  $R^2T$  should be approximately a constant within a Monte Carlo run. This leads to define the Figure of Merit (FOM) for every tally as:

$$FOM = \frac{1}{R^2T}. \quad (2.17)$$

MCNP prints the FOM in the output file for one bin of each tally as function of  $N$ . The FOM is a very important statistics, which is a tally reliability indicator in the sense that if the tally is well behaved, the  $FOM$  should be approximately a constant with the possible exception of statistical fluctuations very early in the calculation problem. An order-of-magnitude estimate of the expected fractional statistical fluctuations in the  $FOM$  is  $2R$ . This result assumes that both the relative statistical uncertainty in the relative error is of the order of the relative error itself and the relative error is small compared to unity.

A better relation between the relative error  $R$  and the  $FOM$  is:

$$R = \frac{1}{\sqrt{FOM \times T}}, \quad (2.18)$$

where it can be seen that a high number of  $FOM$  results into a less required computational time  $T$  to achieve the desired level of precision. In summary, the  $FOM$  has three uses. First, it is used as a tally reliability indicator. Second, it can be used to optimise the MC calculation by making several short test runs with different variance reduction parameters and select the one with the largest  $FOM$ . Third, it can be used to estimate the computer time required to reach a desired value of  $R$  by  $T \sim \frac{1}{R^2 \times FOM}$ .

### 2.3.4 Variance Reduction Methods of Monte Carlo Calculations

MCNP variance reduction techniques allow trying to produce better statistical estimates of the particle density  $N$  where the tally function  $T$  is large, usually at the expense of poorer estimates where the tally function  $T$  is zero or small. Without applying any variance reduction techniques, MCNP performs analogue Monte Carlo calculations, which means, that the sampling of events is according to their natural probabilities. On the opposite, non-analogue techniques do not directly simulate nature. Instead, non-analogue techniques are free to do anything if the particle  $N$ , hence the tally  $\langle T \rangle$ , is preserved. This preservation is accomplished by adjusting the weight of the particles. The weight can be thought of as the number of physical particles represented by the MCNP particle. Every time a decision is made, the non-analogue techniques require that the expected weight associated with each outcome be the same as in the analogue game. In this way, the expected number of physical particles executing any given random walk is the same as in the analogue game.

The aim of using variance reduction methods in Monte Carlo calculations is to reduce the computational time required to obtain results of sufficient statistical precision. Therefore, two different choices can be selected to improve the MC efficiency, which are the tally type and the random walk sampling. Both choices effect the runtime per particle history and the history variance.

The tally location is fixed to the area of interest, but the tally type must be set to return appropriate results. The choice of the correct tally is based on obtaining the best results from the random walk sampled, and must ensure that the tally registers a sufficient large number of events to decrease its relative statistical error.

The chosen random walk sampling corresponds to the preferred sampling ‘important’ random walks, where an important random walk has a large effect on a tally.

In total, MCNP uses three types of non-analogue games:

**Splitting** This means to divide the particle’s weight among two or more daughter particles and following the daughter particles independently. Usually, the weight is simply divided evenly among the daughter particles, and the daughters contribute to the full tally result with the same weights reduced by a number of daughters.

**Russian Roulette** This method takes a particle at  $(\vec{r}, \vec{v}, t)$  of weight  $w_0$  and turns it into a particle of weight  $w_1 > w_0$  with probability  $w_0/w_1$  and kills it (that is,



weight = 0) with probability  $(1 - (w_0/w_1))$ . The expected weight at  $(\vec{r}, \vec{v}, t)$  is  $w_1 \cdot (w_0/w_1) + (1 - (w_0/w_1)) \cdot 0 = w_0$ , the same as in the analogue game.

**Sampling from nonanalogue Probability Density Function** If an outcome ‘A’ is made  $q$  times as likely as in the analogue game, when a particle chooses outcome ‘A’, its weight must be multiplied by  $q^{-1}$  to preserve the expected weight for outcome ‘A’. Let  $p$  be the analogue probability for outcome ‘A’; then  $pq$  is the non-analogue probability for outcome ‘A’. If  $w_0$  is the current weight of the particle, then the expected weight for outcome ‘A’ in the analogue game is  $w_0 \cdot p$  and the expected weight for outcome ‘A’ in the nonanalogue game is  $(w_0/q) \cdot pq$ .

The variance reduction techniques can be used in a combination of the above-mentioned games, and some use all three of it. In total, four different classes of variance reduction techniques are used in MCNP:

**Truncation Methods** These methods neglect parts which do not contribute significantly to the solution. It can be done by e.g. not modelling unimportant parts of the geometry, or by energy cutoff of the particles.

**Population Control Methods** These methods use splitting and Russian Roulette to control the number of samples taken in various regions of the simulation. In important regions many samples of low weight are tracked, while in unimportant regions few samples of high weight are tracked.

**Modified Sampling Methods** These methods change the statistical sampling of a problem to increase the number of tallies per particle. For any Monte Carlo event it is possible to sample from any arbitrary distribution rather than the physical probability as long as the particle weights are then adjusted to compensate. Modified sampling methods in MCNP include the exponential transform, implicit capture, forced collisions, source biasing, and neutron-induced photon production biasing.

**Partially-Deterministic Methods** These methods circumvent the normal random walk process by using deterministic-like techniques, e.g. using the next event estimator, or controlling the random number sequence.

The described classes can take effect on several MCNP variance reduction techniques, or a mixture of these. They cover the energy, time and weight cutoff, geometry splitting with Russian Roulette, energy splitting/roulette and time splitting/roulette, weight window methods, and some more.

A widely used variance reduction technique is the application of the mesh based Weight Window (WW) method. It is a superimposed mesh which covers the whole computational model up to the outside cell boundary. A WW mesh is obtained with a weight lower-bound value on each mesh cell, while the upper-bound is provided in the MCNP input card as a factor, usually 5.0, to the lower-bound. When the weight of a particle is above/within/below the weight window cell, the particle entering this mesh cell will be split/kept/killed by Russian Roulette with the particle weight adjusted accordingly.

The application of these variance reduction techniques must be done very carefully, and the whole problem configuration must be understood before applying such kind of manipulations. At the beginning, all applied variance reduction techniques are analysed with smaller calculation problems until they fulfil the expected behaviour. One possibility is to use the so called ‘F5 point detector tally’ for the quality check during the generation of a mesh based WW. The F5 point detector tally registers the events of the particles if they reach the tally location. Therefore, the location of this tally has to be chosen in such a manner that it is not facing the source and in 10 cm distance to the geometry with void in between. By this measure no interaction between particles and material occur at the point detector region. This is accomplished by setting up the sphere of exclusion around the point detector [Boo85].

## 2.4 Fusion Neutronics

Fusion Neutronics studies the nuclear interaction process of neutrons in a fusion device. As presented from equation 1.1, one neutron is produced per DT fusion reaction. The particle transport is a mathematical problem and can be done either on macroscopic level with deterministic methods, e.g. solving the Boltzmann transport equation to obtain the collective behaviour of neutrons, or on microscopic level by probabilistic methods, e.g. using the Monte Carlo method to simulate each individual particle history. Here, only the probabilistic method with application of the MCNP code is used. The code is well suited to solve the problem for a complex geometry and is verified in a broad field of application [MCN03]. Important input for a neutronic calculation with MCNP is setting up the distribution of source neutrons in space and energy, and providing a geometry including correct material definitions. Both, neutron source and geometry, must be defined as accurate as possible to perform the calculations of interest.

The Monte Carlo method has the benefit, that an accurate quasi ‘exact’ simulation

on microscopic level takes place. Each particle history is investigated from ‘birth’ to ‘death’ whilst performing nuclear interactions with material on its way. It allows to model arbitrary 3D geometry descriptions of any complexity. Also, the accuracy of the calculated results are reliable and limited only by the statistical error and the uncertainty of the nuclear data.

The described relationship between particle flux and particle interaction with matter is recorded in nuclear data libraries, which are the base for particle transport calculations. These libraries need to contain the cross-section data for neutron, photon and electron transport in a wide energy range from  $10^{-3}$  eV to 20 MeV. Inside these libraries are the cross-section data for elastic and inelastic scattering, particle capture, production data for secondary particles like neutrons, photons and electrons, and data for reaction rates of like activation, energy deposition, radiation damage and gas production [Fis18].

The uncharged neutron from the DT fusion reaction escapes the magnetic confinement and interacts with the material of the surrounding geometry. These interactions produce secondary particles which undergo further interactions. All of them are tracked within the way of the birth to the death of the plasma neutron. The interactions are: elastic and inelastic scattering, neutron capture, material degradation (e.g. transmutation, lattice displacement damage), burn-up of initial constituents, build-up of new elements, gas production (e.g. hydrogen, helium) and nuclear heating. Also it is important to take radiation hazard due to activity and decay heat production into account, which are important values for the plant safety (under normal and off-normal conditions) and for the radioactive waste disposal and material recycling [Fis14].

The results of fusion neutronic calculations are important for the design of reactor components. A nuclear design analysis should aim at quantifying the nuclear responses from the simulation and the most relevant are:

**Neutron Flux Distribution** The neutron flux distribution analysis is important to check if the source and geometry are spatial consistent, and if the neutron flux is reduced, when it is further away from the source, as expected. Furthermore, the neutron flux distribution can be used for activation calculations and the estimation of the radiation dose in a specific distance to the source.

**NWL** The Neutron Wall Loading is a quantity that registers the impinging neutrons with its energy on the first wall. The result is a distribution map that shows where, and with which intensity, the neutrons hit the first wall.

**TBR** Tritium Breeding Ratio is a quantity describing how much Tritium is bred per

fusion reaction. The TBR should exceed unity to ensure tritium self-sufficiency of the reactor and optimally should attain a value between 1.05 – 1.15 [Fis20]. The margin above unity account for the radioactive decay of tritium, losses inside the tritium fuel cycle and uncertainties in the used material data libraries for the neutronic calculations.

**Nuclear Heating** Interaction between particles and matter is connected with an energy transfer. Besides the direct transfer between the neutrons and matter, an energy deposition of secondary particles occurs. All together, this results in nuclear heating of the surrounding material. This data is important for the thermal-hydraulic layout of a fusion reactor.

**Shielding Capability** In most cases, neutrons and secondary particles are harmful to matter, but an exception of this is the transmutation of material by neutron capture. The shielding performance is a quantity to evaluate if the neutron and secondary particle flux is attenuated to a tolerable value. Each matter is differently sensitive on the neutron and particle flux, which means that the shielding performance must be investigated at each individual point of interest.

**Gas Production** Reactions between neutrons and matter can lead to the production and accumulation of gas like hydrogen or helium. The gas is produced inside the crystal lattice which may deteriorate the material performance.

All mentioned quantities are of major importance for the engineering design of fusion reactor components. All of the requirements and limits are to be met to ensure operational functionality and safety, maintenance and most important feasibility and performance.

## 2.5 Neutronic aspects in Breeding Blanket Concepts

The Breeding Blanket (BB) is located in a fusion reactor between plasma and vacuum vessel. It has various functions to fulfil simultaneously [And06]:

- tritium self-sufficiency to generate at least the same amount of tritium which is consumed in the fusion reactor,
- conversion of the neutron kinetic energy into heat to maximise the net efficiency related to a high coolant outlet temperature,

- satisfactory radiation shielding to protect the surrounding components, e.g. the superconducting magnetic field coils.

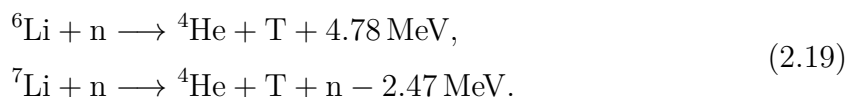
Different BB concepts in the European fusion programme are under development, which are [Boc16] [Fis16]:

- Helium Cooled Pebble Bed (HCPB): solid breeding blanket with lithium (Li) pebbles as breeder material, beryllium (Be) as neutron multiplier and helium gas as coolant,
- Water Cooled Lithium Lead (WCLL): liquid metal blanket with eutectic lead-lithium (PbLi) as breeder and multiplier material, and water as coolant,
- Helium Cooled Lithium Lead (HCLL): liquid metal blanket with eutectic PbLi as breeder and multiplier material, and helium gas as coolant,
- Dual Coolant Lithium Lead (DCLL): liquid metal blanket with eutectic PbLi acting both as breeder, multiplier, and coolant material, and additionally employing helium gas as coolant for the first wall blanket steel structure.

The HCPB and WCLL are selected as primary blanket candidates for the European DEMO tokamak [Fed19]. Nevertheless, the HCLL and DCLL are still considered as possible blanket alternatives, and limited research and development activities are ongoing for these concepts [Fed19].

The DT fusion reaction (equation 1.1) creates one neutron per reaction, but not every neutron undergoes the tritium breeding reaction. The random behaviour of the neutron history leads to loss, capture, leakage, elastic and inelastic scattering in other structures outside the blanket or in the structural material itself. This reduces the total number of available neutrons for the breeding reaction. Thus, neutron multiplier materials, like lead or beryllium, are included in the breeding blanket concepts to compensate for these neutron losses. Another benefit is the moderation of fast neutrons in the neutron multiplier material Beryllium.

The small amount of natural available tritium, as well as the fact that tritium is not a stable isotope, leads to the need of tritium breeding within the reactor in the breeding blanket. Tritium is bred by a neutron capture reaction of the element lithium that naturally contains two stable isotopes with a ratio of 7.59 %  ${}^6\text{Li}$  and 92.41 %  ${}^7\text{Li}$  [Web17]. The tritium breeding reactions are:



Both reactions in equation 2.19 depend on the incident neutron energy and the isotope specific cross-sections shown in figure 2.2. The  ${}^7\text{Li}(n,t)$  reaction is related to a threshold energy of  $\sim 7.6$  MeV. Only neutrons with a higher energy can undergo this reaction. The neutron energy spectra includes also lower energy neutrons that cannot produce tritium with  ${}^7\text{Li}$ , but have a high probability to interact with  ${}^6\text{Li}$ . As indicated in figure 2.2 at lower the neutron energy the probability to undergo a  $(n,t)$  reaction with  ${}^6\text{Li}$  increases. Therefore, this reaction is the preferred tritium breeding reaction. To enlarge the tritium yield, an enrichment of  ${}^6\text{Li}$  up to 60 % for the solid breeding blanket concept and up to 90 % for the liquid breeding blanket concepts is assumed.

In a previous HELIAS study, three different breeding blankets have been investigated as possible blanket concept for the reactor [Wob99]. The paper [Wob99] concludes: ‘From the technical point of view all three blanket concepts are applicable to the HELIAS reactor. Every concept has its merits and drawbacks, and only an integrated design including shield, vacuum vessel and maintenance procedure can prepare the basis to select a specific concept.’ This conclusion shows no limitations from earlier studies regarding the blanket design for HELIAS. A complete engineering design study of the HELIAS reactor can provide sufficient data about the preferred breeding blanket concept for a stellarator power reactor.

The HCPB concept is the only solid breeding blanket concept in the current development. All other use an eutectic liquid Lithium-Lead alloy as a breeder and multiplier material. The biggest advantage of the solid breeding blanket concept is, that it has a smaller radial built compared to a liquid breeding blanket concept due to its moderation capability using Be as multiplier. This is essential for a stellarator type reactor, because of its space constraints compared to a tokamak, between the plasma and the vacuum vessel. The space must be used as efficient as possible to allow for tritium self-sufficiency and neutron shielding.

The first design of the HCPB has been developed at Kernforschungszentrum Karlsruhe (KfK), one of the predecessors of Karlsruhe Institute of Technology (KIT) [DD91] [DD94]. Compared to the other three liquid metal breeding blanket, HCPB uses Beryllium as moderator and neutron multiplier. Beryllium has a low mass number beneficial for neutron moderation, and it has a high neutron cross-section for the  $(n, 2n)$  multiplication reaction at neutron energies exceeding 3 MeV. This design allows multiplication and slowing down of neutrons in the same material with less parasitic absorption. Thereby also the required radial blanket built is smaller compared to the liquid metal blanket designs, which require additional shielding.

The 2016 HCPB design for a tokamak based EU DEMO, shown in figure 2.6, consists of a box defined by the First Wall (FW), the backplate and an arrangement of parallel Cooling Plates (CPs). The FW is covered by a 2 mm layer of Tungsten Armour (W) to protect the FW against sputtering and erosion due to charged particles from the plasma [Her17]. The CPs include separate alternate layers of  $\text{Li}_4\text{SiO}_4$  (breeder material) and Be (neutron multiplier), both in form of pebble beds with a diameter of  $0.25 \div 0.63$  mm for the Lithium Orthosilicate ( $\text{Li}_4\text{SiO}_4$ ) breeding ceramic and a diameter of 1 mm for the Beryllium (Be) neutron multiplier [Her17]. The blanket modules, each individually, are assembled to the Back Supporting Structure (BSS). The BSS acts as main structural support for the blanket segments and as manifold for the purge gas and the helium coolant distribution. The purge gas sweeps in the  $\text{Li}_4\text{SiO}_4$  and Be bed separately and it is composed by He with an addition of 0.1 %wt  $\text{H}_2$  as doping agent to promote an isotopic exchange between the Tritium (T) bred in the pebbles and the doping agent to form HT, helping to the T release and extraction [Her17].

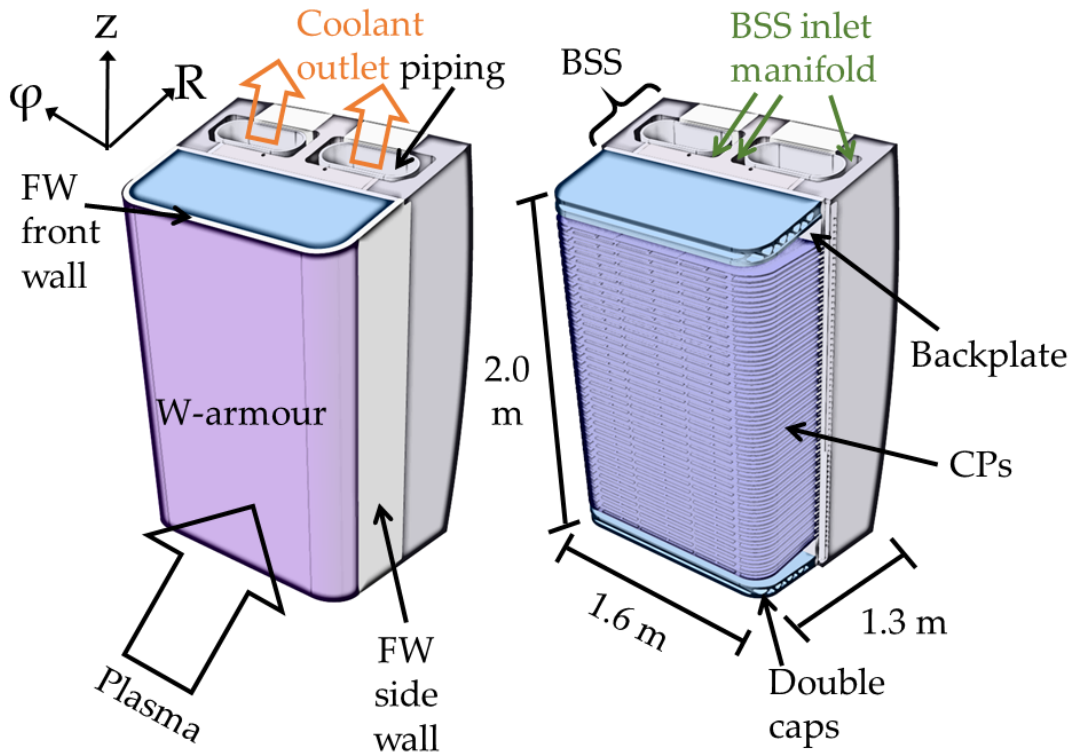


Figure 2.6: HCPB breeding blanket based on a 'sandwich' architecture, on the right with removed first wall to present the interior. [Her17] [Zho17]

The tritium breeding performance of the HELIAS fusion reactor can be assessed using a TBR value which is the number of tritium atoms generated in the reactor per one source neutron. Tritium is generated in the HCPB breeding blanket both in the

breeding ceramic and in the Beryllium (Be) neutron multiplier. The Lithium Orthosilicate ( $\text{Li}_4\text{SiO}_4$ ) breeding ceramic provides a high content of the Li atoms that serve for the tritium breeding through  ${}^6\text{Li}(n,t)$  and  ${}^7\text{Li}(n,t)$  reactions, presented in equation 2.19, with a small contribution of tritons generated in  ${}^9\text{Be}(n,t)$  reaction in the neutron multiplier.  ${}^6\text{Li}$  has  $(n,t)$  cross-sections rapidly increasing with a decreasing of the neutron energy which makes this reaction for tritium breeding the mostly used in fusion technology. The presence of the Be is necessary to provide the neutron multiplication through  ${}^9\text{Be}(n,2n)$  reaction and to enable neutron moderation to facilitate the tritium generation.

Due to the high degree of detail of the tokamak blanket development, the following analysis assumes a similar radial structure of a stellarator blanket and is thus based on the widely available verification and validation results of the tokamak blanket. The operationalisation of a stellarator blanket within the framework of a technical design is not yet available for a stellarator, but does not change much in the material composition of the radial structure. Therefore, assuming a homogenised material composition in neutronic analysis provides fundamental information about the performance of the stellarator breeding blanket concept. The detailed engineering design of the blanket changes these parameters mainly locally and influences them rather in a secondary order. The material definitions applied in this work are derived by the EU DEMO tokamak HCPB breeding blanket material definition by [Spa16] and presented in table 2.5.





# Chapter 3

## Transfer of CAD data to nuclear physics representation

The transfer of CAD data into the nuclear physics representation is a key element of the nuclear design analyses. This chapter gives an overview about the possible transfer options and studies different methods. The original HELIAS 5-B CAD design is shown and the process to generate a CAD model transferable to particle transport simulations is elaborated.

### 3.1 Problem statement and possible transfer options

The computational model in a neutronic calculation with the MCNP code is three-dimensional. The model tries to represent the real conditions as good as possible in the calculations with a reasonable level of details. In earlier time, constructing a geometry for MCNP simulation has been done manually with text input decks, with the tools and methods that the code provides. The construction of a geometry in this way is an extensive, time consuming and error prone task [MCN03]. Different options to generate geometry in an MCNP suitable format are available and discussed here.

As the requirement on the simulation accuracy increases, it simultaneously leads to the increase of the complexity of the computational model. Nowadays dedicated software generates a model, and provides at the same time the possibility of exchanging the model to different applications. It should be noted that the CAD and the MCNP representations are based on two different approaches of geometry representation. The CAD geometry is designed as boundary representation composed for models into two

parts: topology and geometry. The topology is a set of faces, edges and vertices, while the geometry is a set of surfaces, curves and points. This means that a face is a bounded part of a surface, an edge is a bounded piece of a curve and a vertex is located at a point [Mä88]. The CSG representation, used by MCNP, in contrast uses simple objects e.g. cube, cylinder, sphere, or Boolean algebraic based half-spaces to combine into solids. Generally speaking, the boundary representation is more adaptable and complex geometries can be generated much easier compared to the CSG geometry.

The CAD models are often generated with a high level of details, which is not favourable in neutronic calculations, because the details have less impact on the results but consume a lot of computational time in the calculation. These geometries need to be simplified, e.g. reduction of levels of details or replacement of high-order surfaces with simpler surface descriptions. Furthermore they require to be reconstructed to fit into the restrictive geometry set-up of MCNP. Therefore, three different geometry conversion options for the transfer of CAD into MCNP representation are considered:

1. Traditional CAD to Constructive Solid Geometry (CSG) conversion,
2. Generation of hybrid CSG and Unstructured Mesh (UM) geometry,
3. Direct particle tracking in faceted CAD geometry with Direct Accelerated Geometry Monte Carlo (DAGMC).

All three geometry modelling methods require a different approach to create a MC geometry for MCNP. Aim of this translation process is to generate a MC geometry with the least possible deviations from the CAD model. This is challenging, because all of the investigated transfer options have pros and cons, as discussed subsequently.

The CSG method is the standard modelling approach for fusion neutronics calculations and needs to be investigated for the application to a stellarator reactor. This translation approach uses dedicated geometry conversion software, e.g. McCad [Lu14] developed at KIT, Germany, or ‘Super Multi-functional Calculation Program for Nuclear Design and Safety Evaluation (SuperMC)’ [Wu09], [Wu18] developed at Institute of Nuclear Energy Safety Technology (INEST), China, to generate a CAD based MC geometry. In the CSG description mainly first and second order surfaces are allowed, e.g. planes, cylinder and sphere as adapted by the MC particle transport codes, except one fourth-order surface: torus, which is also supported. Spline surfaces, which are fourth order surfaces, are not supported and McCad does neither translate nor simplify them for translation [MCN03]. For a complex geometry like the stellarator, the CSG method, without CAD model simplification and modification, is hardly applicable for

creating a reasonably accurate model. Nevertheless, the CSG geometry description is the best verified and validated method of all three investigated methods.

It is known that the construction of CSG, to represent the CAD model, becomes difficult, tedious, time-consuming and error-prone, demands rise for a new modelling approach to overcome these issues. As a result, a better way to develop and construct geometries for MC based particle transport simulations is launched [Mar14], that is the unstructured mesh modelling approach which has been initially introduced in MCNP6. It includes the capability to use an UM geometry representation in the particle tracking simulation. An UM is approximating a CAD model, independent of the CAD model surface description, to a set of mesh elements with first- and second-order surfaces. It brings the advantage that very complex geometries can be handled in MC simulations without laborious simplification or decomposition. There are some limitations on using UM in the MCNP6 code. One of them is that only tetrahedral, hexahedral and wedge elements can be accepted at the same time and a mixture of different mesh types is rejected. ANSYS Workbench [Ans18] has been used as meshing tool to generate the unstructured mesh geometry. It is possible to adapt the generated mesh to the limitations of MCNP6.

The DAGMC approach for the direct use of CAD geometry in the MC transport simulation has been used as third approach. DAGMC adaptations to different MC radiation transport codes are available. Here, the DAGMC patch for MCNP has been applied. DAGMC uses a faceted geometry, which is a surface mesh, for the particle tracking. The approach can analytically solve a number of lower order surfaces, but higher order surfaces require iterative numerical root-finding approaches which are implemented in DAGMC with a number of acceleration techniques and approximations [Wil10]. This ensures that the method can be efficiently used for high order surfaces, like spline or other fourth-order surfaces. The tracking algorithm applied in DAGMC is based on the ray-tracing technique. This technique allows the performance of simple calculations to determine the next surface boundary, depending on the particle position and its movement trajectory [Wil10]. The CAD geometry is prepared with Trelis [Cor20] to ensure that all bodies and surfaces are preprocessed and faceted in the correct way for the use with DAGMC.

## 3.2 Overview and Preparation of the HELIAS 5-B CAD model

The original HELIAS 5-B CAD model is provided by IPP Greifswald, Germany. It was originally created, mainly with splines (fourth-order surface) and planes (first-order surface), to show the remote maintenance function of HELIAS 5-B [Sch13]. As shown in the paper from F. Schauer, the basic concept of HELIAS 5-B is applicable for maintenance tasks, but neutronics investigations have not been part during the construction of the CAD model. The original model contains a blanket envelope model which is a layer representing the breeding blanket and back supporting structure, and the double layer Vacuum Vessel (VV), and five non-planar shaped field coils. All these components are shown in figure 3.1. The envelope model has openings for the divertor from  $\varphi = 0^\circ$  to  $\varphi = 18^\circ$  of the  $36^\circ$  half-field period model. Neither the divertor design nor the final position of the divertors are currently set. The openings are highlighted with yellow circles in figure 3.1.

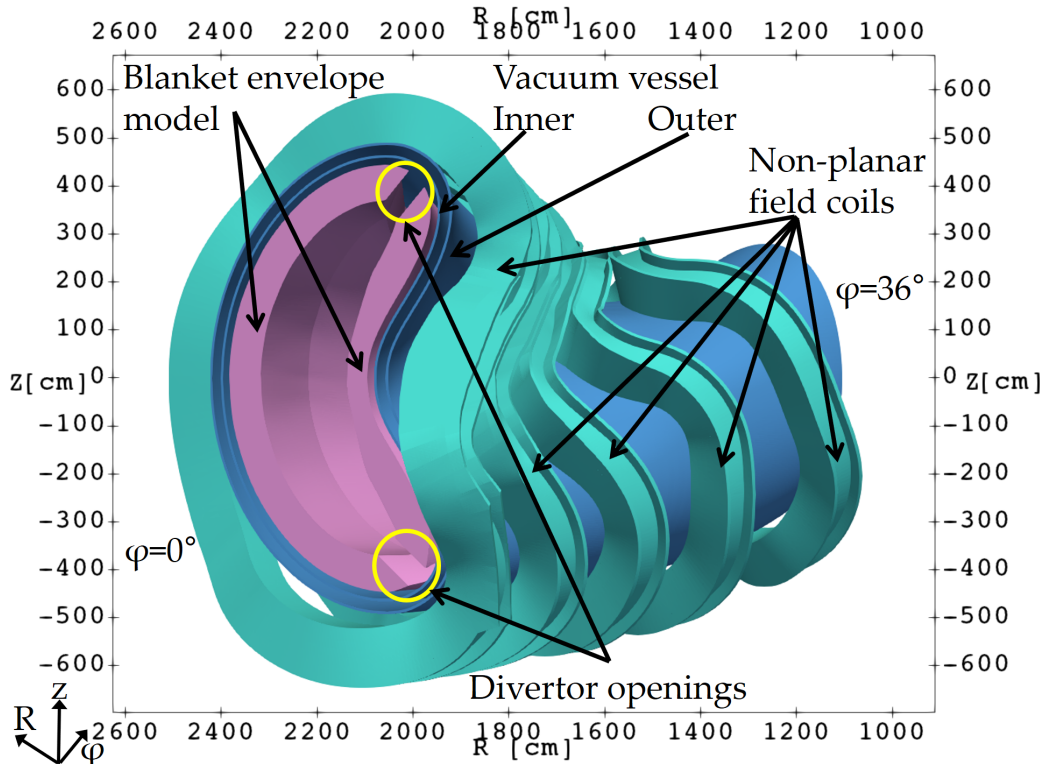


Figure 3.1: Primary CAD model, including blanket envelope model (purple), vacuum vessel (light blue) and non-planar shaped field coils (turquoise), provided by IPP Greifswald, Germany [Sch13]. The divertor openings at the bean shape side ( $\varphi = 0^\circ$ ) are highlighted with yellow circles.

For a principle neutronic analysis, a simplified model with less details and sep-

arated homogenised material zones is appropriate. The focus is to demonstrate the capability to run neutronic simulations for a stellarator type reactor with the currently available MC particle transport approaches without including too many details in the preliminary CAD design.

### 3.2.1 Examination of a stellarator half-field period

The complete HELIAS 5-B stellarator reactor consists of five field periods, which means that one field period represents  $72^\circ$  of the entire power reactor. In neutronic simulations, typically reflecting boundary conditions are used to represent the full reactor geometry correctly. The complicated stellarator description makes a simple CAD to MC geometry translation impossible. Even with different conversion approaches, like UM and DAGMC, a full  $72^\circ$  model is hard to generate and yield to a large input geometry, which consumes a lot of memory and computational power for the MC calculations. A simplification of this complicate geometry problem is a  $36^\circ$  model assuming reflecting boundary conditions. This cannot replace a  $72^\circ$  model completely. The configuration is illustrated in figure 3.2 including a red line representing an example neutron track. The reflecting boundary is acting like a mirror which is indicated by a dotted line of the neutron track in the  $36^\circ$  model.

The simplified geometry in figure 3.2 represents a  $72^\circ$  model on the left side and a  $36^\circ$  model on the right side with reflecting boundary conditions and its resulting projection. At first glance, the shape of both representations seems to be the same geometry. This is not the case when the magnetic configuration in this example is taken into account, which is tried to represent with the colour gradient. The  $72^\circ$  model can be generated by two  $36^\circ$  models while one of them is flipped over and both are attached at the flipping axis. This introduces a systematic error in the investigation of a  $36^\circ$  model instead on a  $72^\circ$  model. For principle neutronics investigation of a stellarator, a  $36^\circ$  model can be used because the systematic error has only a marginal influence on the global quantities like NWL, TBR and the neutron flux distribution. The results obtained later can be used without re-calculation in a  $72^\circ$  model, as they only present a principle investigation of the stellarator. Other benefits of a  $36^\circ$  model are the need of less computational power, assumed lower computational time, and the presumed easier transfer of the CAD into MC geometry description.

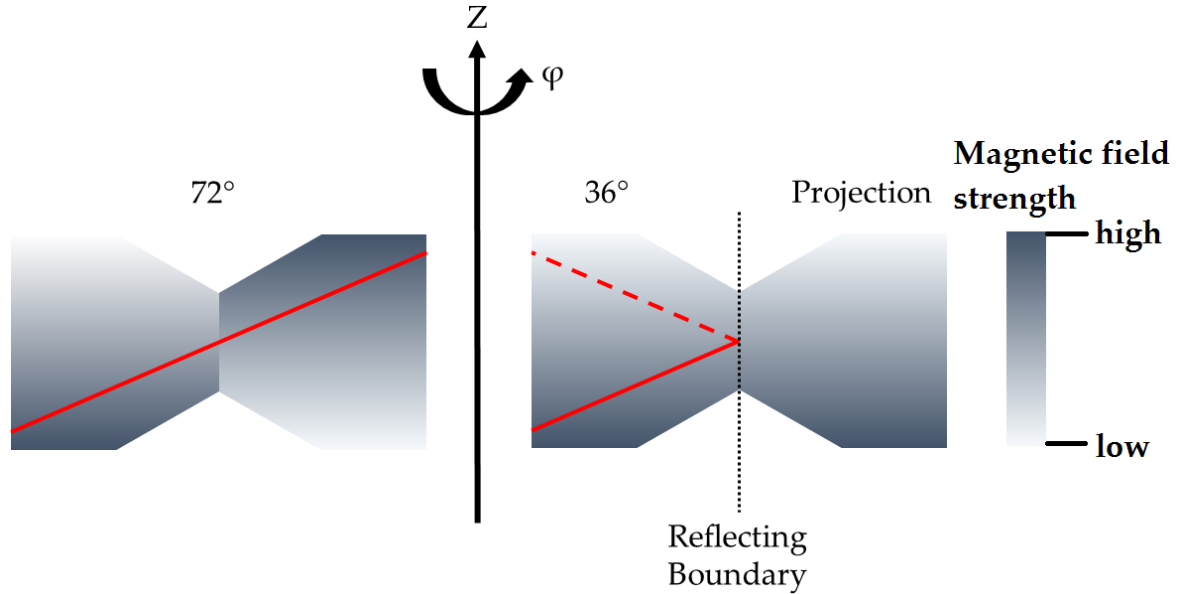


Figure 3.2: Example of a 72° model (left) compared to a 36° model (right) with reflecting boundary conditions, including a red line representing an example neutron track. The grey scale indicates the magnitude of the magnetic field strength.

### 3.2.2 Repair of the envelope model

The blanket envelope model is a dummy volume layer representing the space assumed for the BB and the BSS. The plasma facing side of this layer depends on the the shape of the Last Closed Flux Surface (LCFS), and the minimum distance between plasma and first wall. The radial thickness of the envelope model is flexible between FW and the VV.

The LCFS was created as a by-product during the generation of the plasma distribution for HELIAS 5-B. This surface describes the outermost closed magnetic surface without intersecting the reactor geometry. It is therefore the boundary surface between the plasma, which is inside the LCFS, and the surrounding components. This surface is used to check, if the plasma and the CAD geometry fit to each other in meaning of its spatial location. Several collisions have been detected between the LCFS and the blanket envelope model, which are a result of inaccurate CAD modelling. One example at the triangular shape side, at  $\varphi = 36^\circ$ , of the model is depicted in figure 3.3. These collisions are spread over a large area, mainly at the outboard side which is in radial direction the side furthest away from the central axis. To solve this problem, the LCFS has been extended to 10 cm in direction to the blanket envelope model with respect to the surface normal vector. All parts of the blanket envelope model inside the extended LCFS have been removed. This ensures at least a space of 10 cm between the plasma

and the plasma facing material layer, as shown in figure 3.4 with the modified blanket envelope model. The 10 cm space is a minimum requirement of the plasma physicists at IPP Greifswald and is a result of the magnetic plasma confinement.

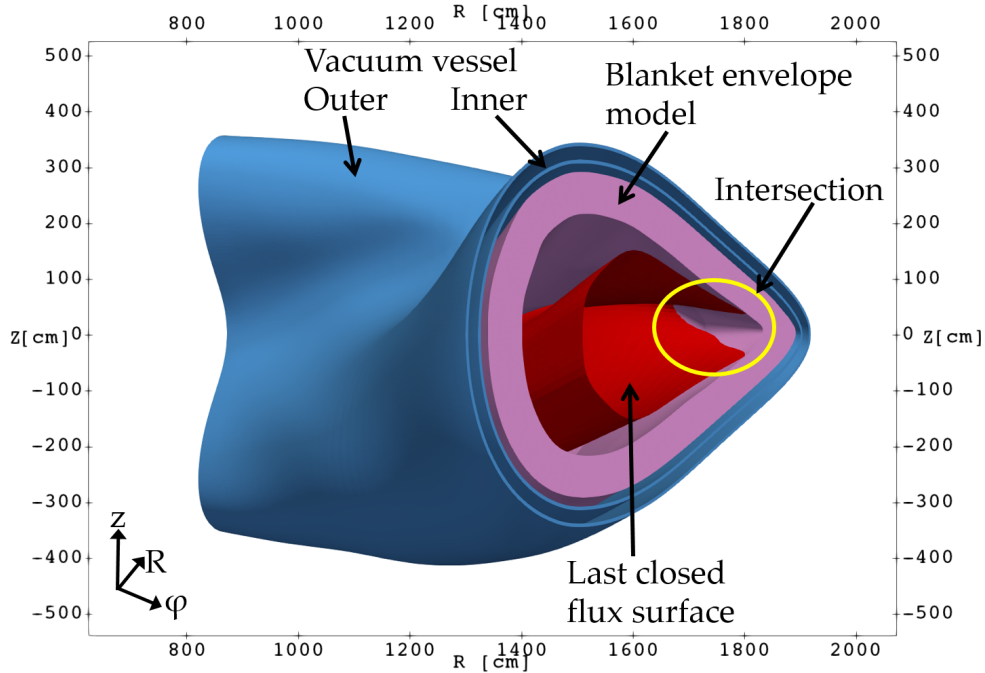


Figure 3.3: Sketch of the HELIAS 5-B CAD model at the triangular shape side  $\varphi = 36^\circ$  containing the blanket envelope (purple), the double layer vacuum vessel (light blue) and the last closed flux surface (red). The intersection between blanket envelope and LCFS is highlighted inside the yellow circle.

### 3.2.3 Refinement of the envelope model and introducing material layers

The original CAD model from IPP Greifswald contains only one envelope layer without subdivision into different material layers. The envelope model is composed of eight rings with each five parts, in total 40 parts. Furthermore, figure 3.1 shows a gap between the blanket envelope model and the inner shell of the vacuum vessel, and a gap between vacuum vessel inner and outer shell. All the empty space is filled manually through enlargement of the modified envelope model and by introduction of a new volume cell between the vacuum vessel. The subdivision of the modified envelope model is consistent with the EU DEMO tokamak reactor concept [Fis14]. The presented subdivision can be adapted to the stellarator, which is shown as an example for one blanket module in figure 3.5. The subdivision is performed by moving the plasma facing surface through the solid and cut the solid in a certain radial depth



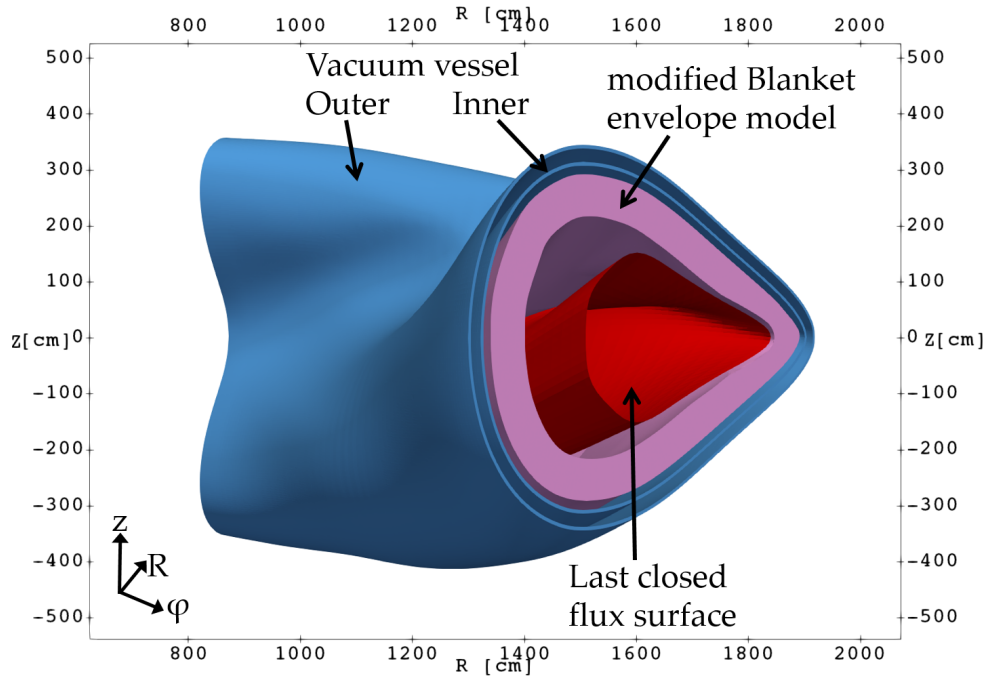


Figure 3.4: Sketch of the HELIAS 5-B CAD model at the triangular shape side  $\varphi = 36^\circ$  containing the modified blanket envelope (purple) with at least 10 cm distance to the last closed flux surface (red), and the double layer vacuum vessel (light blue). All intersections between blanket envelope and LCFS are repaired.

to generate the different layer thicknesses. This process is conducted manually and every adaptation, e.g. introduction of a new layer or changing the radial thickness, is therefore very time consuming.

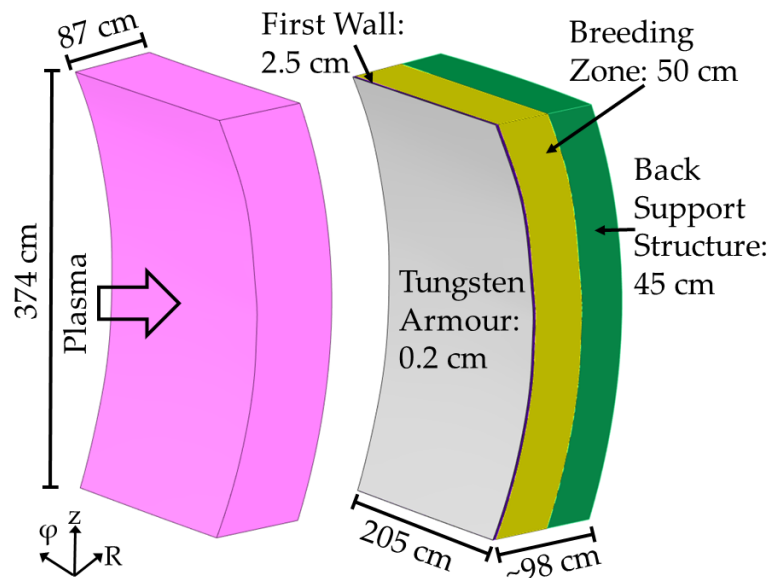


Figure 3.5: Sketch of layering of one blanket module. Left original envelope module and right with layers of different material compositions. The material colour coding corresponds to table 3.1.

The resulting radial layout, from the plasma towards the outside of the stellarator, is presented in table 3.1. Additionally, the thickness of each layer and its homogenised material composition, according to [Spa16], is given. The colour coding in this table refers to the colouring of the material layers in the HELIAS geometry and is visualised in figure 3.6. The JEFF 3.2 [JEF14] nuclear database is used in all MCNP calculations.

Table 3.1: Radial build of the HELIAS stellarator mid-plane from plasma to outside, materials according to [Spa16].

| THICKNESS [CM] | COMPONENT              | MATERIAL   | COLOUR     |
|----------------|------------------------|--|------------|
| 0.2            | Tungsten Armour        | 100 % Tungsten                                   | grey       |
| 2.5            | First Wall             | 70 % Eurofer [Fin09],<br>30 % Helium             | dark blue  |
| 50             | Breeding Zone          | Homogenised HCPB BB<br>with 60 % Li-6 enrichment | yellow     |
| ~ 10 - 45      | Back Support Structure | 75 % Eurofer, 25 % He-<br>lium                   | green      |
| 6.0            | Inner Vacuum Vessel    | 100 % Stainless Steel<br>(SS316-IG)              | light blue |
| 20             | Vacuum Vessel Shield   | 60 % Stainless Steel<br>(SS316-IG), 40 % Water   | orange     |
| 6.0            | Outer Vacuum Vessel    | 100 % Stainless Steel<br>(SS316-IG)              | light blue |

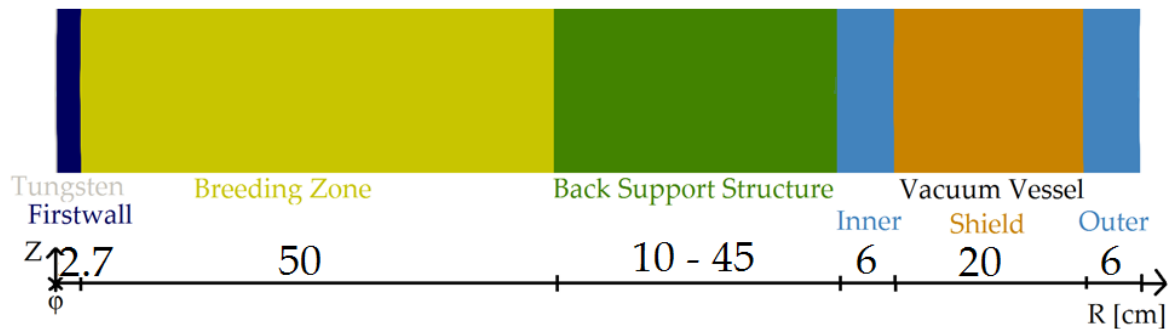


Figure 3.6: Colour coding of the material layers inside the HELIAS geometry, radial build up refers to table 3.1.

The refinement process introduces new solids due to the subdivision of the envelope model. The total number of solids per material layer of the final model is presented in table 3.2. The large deviation between 40 solid parts of the envelope model and the layered model at the end is a result of the CAD conversion process. It is often necessary to subdivide a solid into smaller volumes to allow for its correct conversion

into an MCNP geometry. The vacuum vessel in the original model contains one solid for each inside and outside layer, and it has been split due to the same reasons.

Table 3.2: Number of solids in the HELIAS CAD model.

| COMPONENT                 | NUMBER OF SOLIDS |
|---------------------------|------------------|
| Tungsten Armour           | 106              |
| First Wall                | 137              |
| Breeding Zone             | 73               |
| Back Support Structure    | 87               |
| Inner Vacuum Vessel Shell | 5                |
| Vacuum Vessel Shield      | 3                |
| Outer Vacuum Vessel Shell | 5                |

Figure 3.7 shows a sketch of HELIAS at the bean shape side  $\varphi = 0^\circ$  including the material layers. The different layers, including the variation of the thickness in the back support structure, can additionally be seen in figure 3.8.

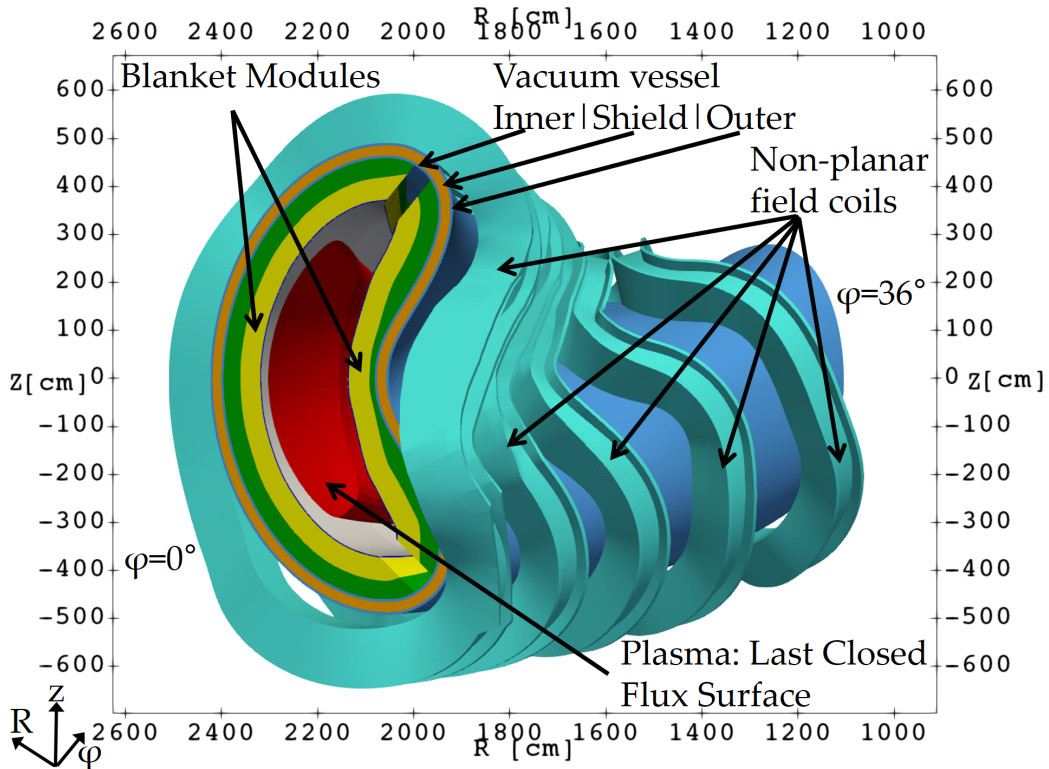


Figure 3.7: Sketch at the bean shape side  $\varphi = 0^\circ$  of the HELIAS reactor with the layered structure in the blanket modules, including Tungsten Armour, First Wall, Breeding Zone, and Back Support Structure. The colour coding refers to table 3.2.

Two zones with a maximum and minimum available space in the stellarator are shown in figure 3.8. The available space in this sense means the radial space between

plasma facing layer and vacuum vessel outside. The shape of the VV is defined by the non-planar shaped field coils and can thus not be extended in radial direction. The zone with the maximum available radial space of  $\sim 127.2$  cm is comparable with the thickness of the inboard side in the EU DEMO tokamak. This available thickness is presumably sufficient for satisfying tritium breeding and shielding requirements. The minimum available radial space of  $\sim 96.7$  cm is challenging in the neutronic investigations to fulfil design requirement limits as e.g. for the neutron flux attenuation, and the shielding performance. A total thickness of less than 1 m needs a different set-up for a reduced / minimised breeding zone, and / or a larger shielding layer with more efficient shielding material.

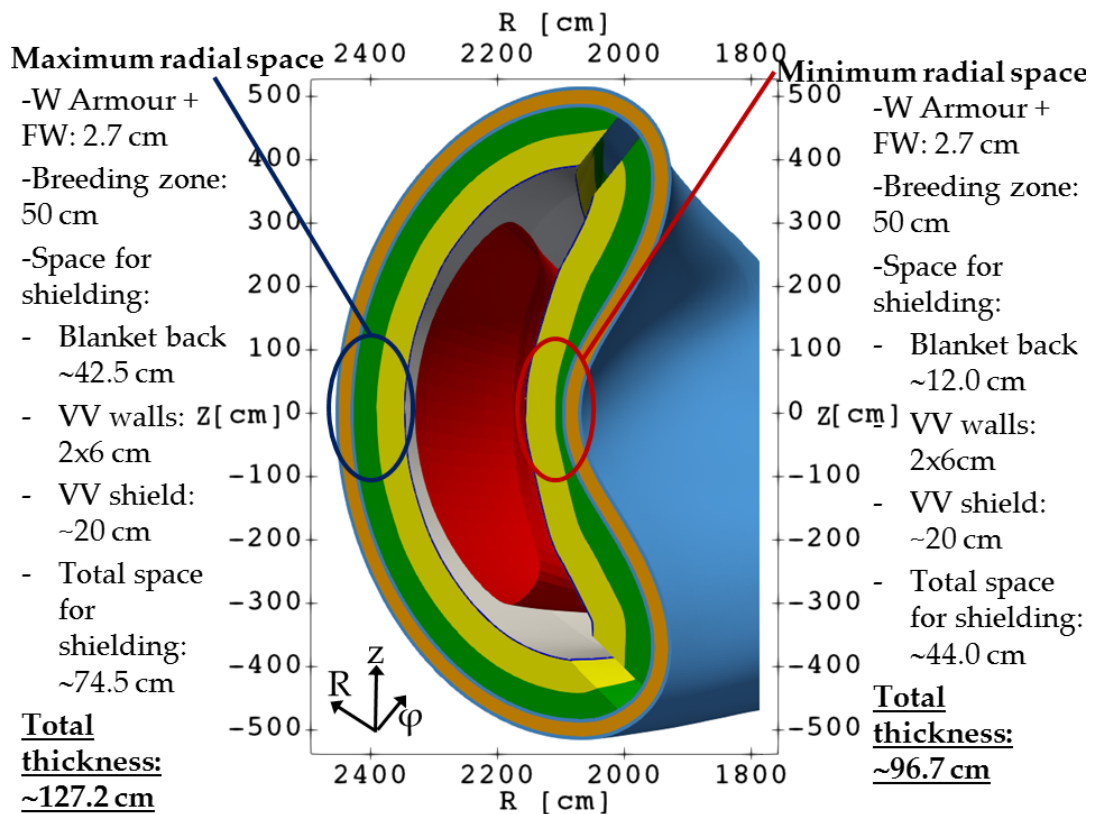


Figure 3.8: Sketch of the bean shape side  $\varphi = 0^\circ$  to present the maximum and minimum available radial space for the reactor components inside HELIAS.

### 3.3 CAD models before translating into MC geometry representation

Two different CAD models of HELIAS are used in the neutronic simulation for different purposes. The one mainly used is the half-field period stellarator model containing all material layers. The second CAD model is only used to calculate the NWL. Therefore, it contains only the plasma facing layer.

The superconducting field coils are not integrated in the computational models. The coils have very complicate surface descriptions and thus increase the needed computational power which leads to a decrease of the computational speed. Beside this, the coils are complicated to transfer into an appropriate MC geometry description.

#### 3.3.1 Global HELIAS CAD model ready for neutronics simulation

The global HELIAS CAD model is the main model. It is represented mainly by spline and plane surfaces. There are several assumptions taken on the geometry. Firstly, the opening for the divertor which increases the neutron losses and could lead to an under-/over-estimation of nuclear responses like the TBR. Secondly, the absence of ports for the plasma heating system and diagnostics system translating to a potential overestimation of the TBR. These must be taken into account during the nuclear analyses for evaluating the results.

The CAD model, in different perspectives, is presented in figure 3.9. This figure present the transformation of the stellarator cross-section, from bean shape  $\varphi = 0^\circ$  to triangular shape  $\varphi = 36^\circ$  side, as well as the dimensions of the reactor.

#### 3.3.2 CAD model for the Neutron Wall Loading (NWL) calculation

The peculiarity of the NWL calculation is that only the plasma facing layer is needed, which is the tungsten armour layer in HELIAS. All other components are not taken into account, which reduces significantly computational resources.

The CAD geometry of the tungsten layer must be edited, because the original design is too coarse to generate a smooth NWL distribution. In total, eight different solid rings including 106 solids represent the tungsten area in the  $36^\circ$  reactor section model. It is important to split the large solids into smaller tiles to generate a higher

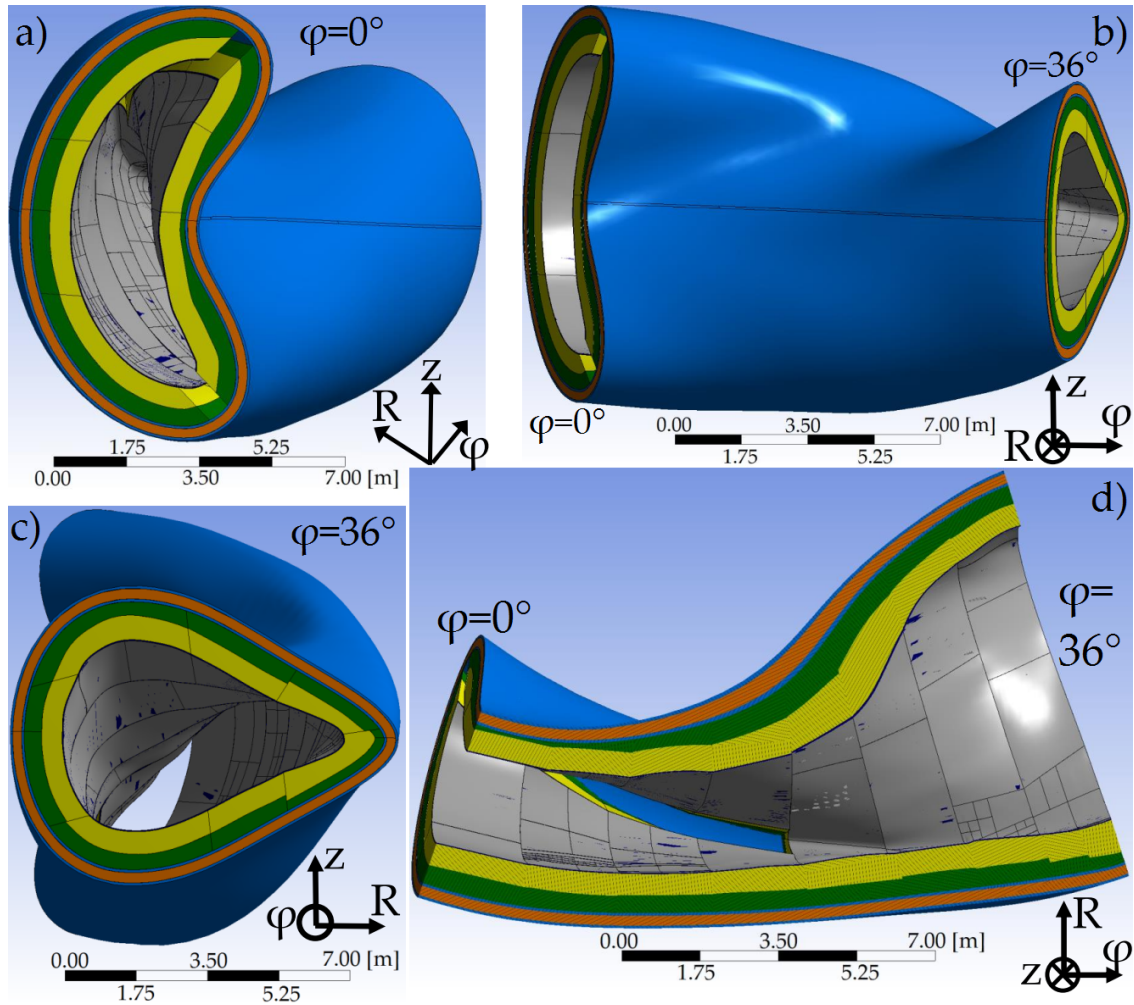


Figure 3.9: HELIAS CAD geometry including material layers, colour coding refers to table 3.2, in different perspectives. From top left to bottom right: (a) bean shape side at  $\varphi = 0^\circ$ ; (b) view from the coordinate centre to the inboard side; (c) triangular shape side at  $\varphi = 36^\circ$ ; (d) cross-section at the midplane  $z = 0$  cm with view to the upper section.

resolution in the NWL distribution. The small tiles are needed additionally to identify domains with the highest / lowest loads. It has been tried to split each solid ring into five  $1^\circ$  rings in toroidal direction. A drawback of this separation is that some of the  $1^\circ$  rings are not fully closed, and some of the rings have toroidal thicknesses of less than one degree. This step must be executed carefully to create not too small tiles, because smaller tiles require more particles to obtain statistically reliable results. Finally, 1845 tiles have created in a range of  $0.05 \text{ m}^2$  to  $0.24 \text{ m}^2$  with an average size of about  $0.15 \text{ m}^2$ , which are illustrated in figure 3.10.

The blue tiles in the refined tungsten layer in figure 3.10 show the indicator for the mid-plane, which is a plane at  $z = 0$  cm. It is later used for the presentation of the NWL results.

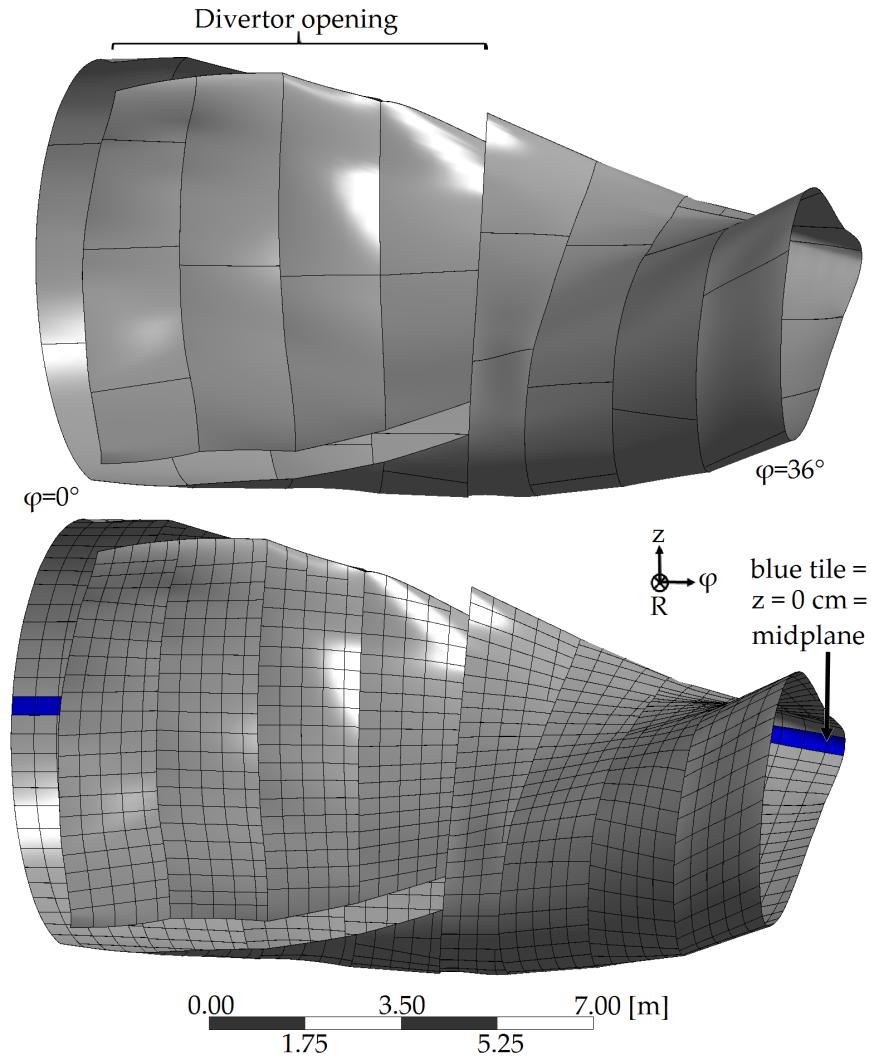


Figure 3.10: Tungsten layer before (top) and after (bottom) preparation for the NWL calculation including refinement into 1845 tiles. The blue tiles in the refined model indicate  $z = 0$  cm to represent the midplane.

### 3.3.3 CAD geometry for set-up of the MCNP boundary condition

Each MCNP simulation needs the definition of the whole calculation area including the indication of boundary conditions [MCN03]. If the boundary conditions are missing, MCNP follows one particle without an outline of the simulation area which ends up in an infinite calculation for this one particle. A graveyard region outside the simulation area, where all entering particles are killed immediately, must be defined. Reflecting surfaces will reflect a particle, which hit such a surface, like a mirror [MCN03]. This feature can be used for the simulation of the stellarator to reduce the computational effort. In fact, the CAD stellarator model created represents only one

tenth of the full stellarator, but the generated results are valid for the full stellarator model if they are composed of identical sectors. A good approximation for the first neutronic investigations is to use reflecting boundary conditions at the bean shape side  $\varphi = 0^\circ$  and at the triangular shape side  $\varphi = 36^\circ$  of the stellarator.

The calculation area has been created as box covering the whole geometry. The box must be adapted to the bean and triangular shape side to apply at each side a plane with the reflecting boundary conditions. These two planes have a spacing between the stellarator geometry of 0.02 mm which is necessary to guarantee the correct work of the plasma source. The gap is at the same time small enough to be negligible in the neutron transport calculation. If the spacing is not introduced, MCNP cannot handle the plasma source correctly, because particles can be generated outside the reflecting boundary in the graveyard region. The figure 3.11 presents the geometrical boundary of the simulation, including the two reflecting surfaces.

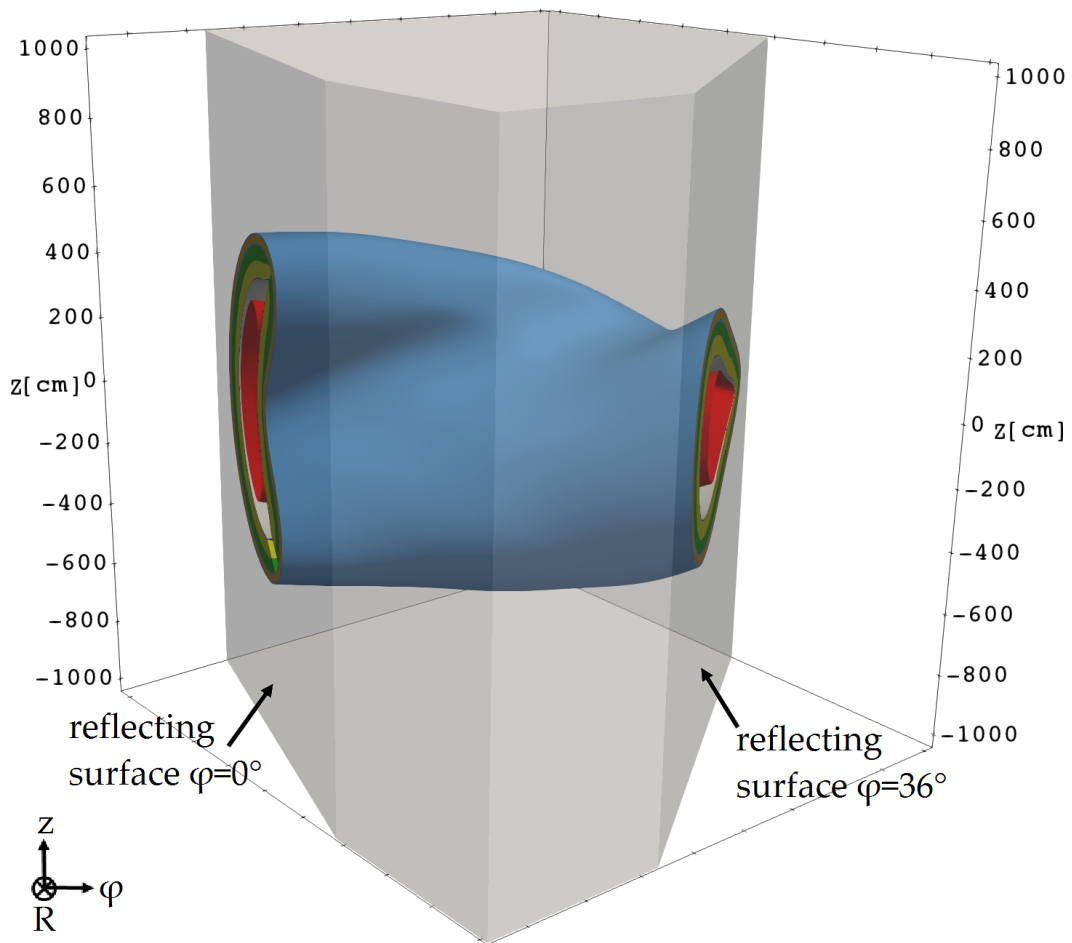


Figure 3.11: CAD bounding box, in light grey colour, representing the whole simulation area. The surfaces on the bean  $\varphi = 0^\circ$  and triangular  $\varphi = 36^\circ$  shape side of the stellarator have reflecting boundary conditions in the MCNP simulations.



### 3.4 Analysis of different options to represent a stellarator geometry

Three different CAD to MCNP geometry transfer options are considered to generate a stellarator neutronics model, which are CSG, UM, and DAGMC. The requirement of a geometry transfer is an error-free CAD model. Error-free means, that the CAD model has no overlaps, no intersections, no gaps and no undefined spaces. An overview of the transfer approaches is presented in table 3.3, which describes the necessary steps executed for each approach. The bottom of table 3.3 refers to the resulting MC geometry which needs to be checked and compared with the used CAD geometry. The volumetric comparison proves that the resulting MC geometry volumes have a low deviation to the CAD data. Thus, the accuracy of the geometry transfer is guaranteed. Another quality test is the investigation of the lost particle rate in the particle transport simulation which is necessary to decide if the geometry can be used in particle transport simulations. An acceptable rate for the ITER tokamak neutronic calculations is ‘generally below 1 in  $10^7$ ’ [Lei18] starting particles, and the DAGMC developers recommend a rate ‘below 1 in  $5 \times 10^6$ ’ [The16] starting particles. Further details about each geometry transfer option and the resulting quality assurance for the MC geometries is given in the appendix A.

The steps presented in table 3.3 are applied to the HELIAS CAD geometry. The results of the MC geometry preparation are presented:

**CSG** The HELIAS envelope model, containing a single material layer, is used to transfer into the CSG representation. The CAD model consists mainly out of spline surfaces which are replaced with first- and second-order surfaces. This ends in a fine segmentation of the envelope layer to ensure the volume consistency between the CAD and the CSG model. Several lost particle checks show a ratio of  $\sim 20\%$  lost particles in the model, which is a not acceptable rate for a computational model. The surface replacement and volume segmentation leads to problems, especially if more than three surfaces connects at one edge, or if tiny gaps between the edges occur. The traditional CAD to CSG geometry translation approach is currently not suitable for modelling a stellarator geometry.

**UM** The hybrid geometry is a mixture of a CSG geometry boundary filled with an UM geometry. This allows to model complex geometries in UM, and combine them with a simple CSG bounding box which provides the surface boundary conditions. MCNP supports only one mesh element type inside the geometry

Table 3.3: Overview of the workflow of three different CAD to MCNP geometry transfer approaches.

| CAD MODEL   |  |  |
|---|--|--|
| CSG   | UM   | DAGMC  |
| Requirements to the CAD model: clean, error-free and low level of details.  |  |  |
| <ul style="list-style-type: none"> <li>• model simplification: replace high-order surfaces with 1<sup>st</sup>/2<sup>nd</sup> order surfaces</li> <li>• decomposition of the CAD model: cut solids into sign-constant solids</li> <li>• assign material/density information</li> <li>• assign bounding box as simulation boundary</li> <li>• Geometry translation with McCad [Lu14] to convert into MC geometry including void space generation</li> <li>• check quality and consistency of the CSG geometry</li> </ul> | <ul style="list-style-type: none"> <li>• select mesh element type according to the geometry</li> <li>• imprint the surfaces and generate geometry mesh with ANSYS Workbench [Ansl8]</li> <li>• investigate geometry mesh quality with ANSYS internal checks</li> <li>• associate the mesh to the corresponding CAD geometry</li> <li>• assign material/density information</li> <li>• assign bounding box in CSG geometry as simulation boundary</li> <li>• generate geometry input parameters for MCNP simulation</li> <li>• check mesh geometry quality with MCNP6 tool 'um_pre_op' [Mar14]</li> </ul> | <ul style="list-style-type: none"> <li>• Trellis [Cor20] used for grouping volumes to assign material/density information, execution of the imprint / merge operation, and integration of the bounding box as simulation boundary</li> <li>• export via Trellis DAGMC plugin into faceted surface representation</li> <li>• run 'make_watertight' operation to seal model: ensures no topological weaknesses exists [The16]</li> <li>• check geometry quality with internal DAGMC tests</li> </ul> |
| <p>Geometry checking: model investigation of volume consistency (compared to CAD files), obtain lost particle rate, and investigate for geometry conversion errors like deformed mesh elements or not sealed volumes.</p>   |  |  |

and the tetrahedral mesh elements are used, which fit best inside the bend geometry in the stellarator. The layered HELIAS CAD model is transferred into more than  $1 \times 10^8$  tetrahedral elements, and it shows a volumetric deviation of less than 0.11% to the CAD geometry. All mesh quality checks, provided by ANSYS Workbench [Ans18] and MCNP6 [Mar14], are passed. Lost particles are not detected inside the UM geometry, but a misbehaviour of geometry during the simulations which leads to infinite loops in the particle tracking. The UM geometry is a recent development of the geometry description in MCNP6 and it only supports a limited number of tallies and mesh elements which limits the method. Therefore, it is not the preferred HELIAS geometry transfer approach.

**DAGMC** The layered HELIAS CAD model is used to transfer into the faceted DAGMC representation. In Trelis [Cor20], the geometry pre-processing including imprint / merge, material assignment and introduction of the graveyard as simulation boundary is performed. The resulting DAGMC geometry contains more than  $1 \times 10^8$  facets. The volumetric deviation is for a few solids  $\sim 4\%$ , but most solids have less than 1% deviation. An error-free DAGMC geometry could not be generated, and a lost particle rate of  $\sim 2 - 3$  lost/ $1 \times 10^6$  birth particles has been determined. The lost particles are spread over the whole geometry without an accumulation at a specific place. This rate is considered in general as acceptable for the upcoming simulations. DAGMC is the preferred approach for the generation of the HELIAS MC geometry, because it supports all functions of MCNP and has no limitations in the allowed CAD surface description.

The investigated geometry transfer options have benefits and limitations compared to the traditional CSG method. The most important benefit of UM and DAGMC is, that these approaches can handle the complex stellarator geometry without simplification. Nevertheless, a limitation of UM and DAGMC is that they require additional software to prepare the geometry. The resulting UM and DAGMC geometry require a larger amount of computational resources during the neutronics investigation, and the total runtime of a simulation is by a factor of 2 to 5 higher than in CSG. A drawback of UM are the limitations in MCNP, because only one mesh element type is allowed per mesh geometry, and a limited number of tallies in MCNP supports UM. The DAGMC method do not has these limitation, it supports all functions of MCNP and is currently the preferred approach in stellarator neutronics.

# Chapter 4

## CAD to MCNP Geometry Conversion Method Verification

The chapter explains the verification of three different geometry conversion approaches aimed to apply for the HELIAS geometry using a simplified geometry. First, an overview about the construction of the simplified CAD geometry is given, with a description of the resulting three MC geometries. Second, the MCNP source description, applied to the calculations in this chapter, is provided. Third, the results of MCNP calculations of all geometry conversion approaches are analysed, see also [Hä17].

### 4.1 Construction of the CAD verification geometry

A dedicated CAD verification geometry is designed that fits into all limitations of the three investigated geometry conversion methods. In fact, the traditional CAD to MCNP translation approach has the most constraints, because the CSG description is more limited than the other investigated conversion approaches. Only cylinders, which are second-order surfaces, and planes, which are first-order surfaces, are included in the verification geometry. The verification geometry is based on a bean shape cross-section of the stellarator as shown in figure 4.1. It has a total height of about 1030 cm, a maximum width at the equatorial plane,  $z = 0$  cm, of about 490 cm, a total width of about 640 cm, and a depth of 100 cm ( $\varphi = 4^\circ$ ) [Hä17]. The radial build with a layered structure of the verification geometry along the red line (position:  $R = -520$  cm to  $R = -30$  cm at  $z = 0$  cm,  $\varphi = 2^\circ = 50$  cm), which is used as tally location for future calculations, is shown in figure 4.1 and in table 4.1. The outboard and inboard sides are indicated in figure 4.1 and named by their distance to the central axis, with the inboard side closer to this axis.

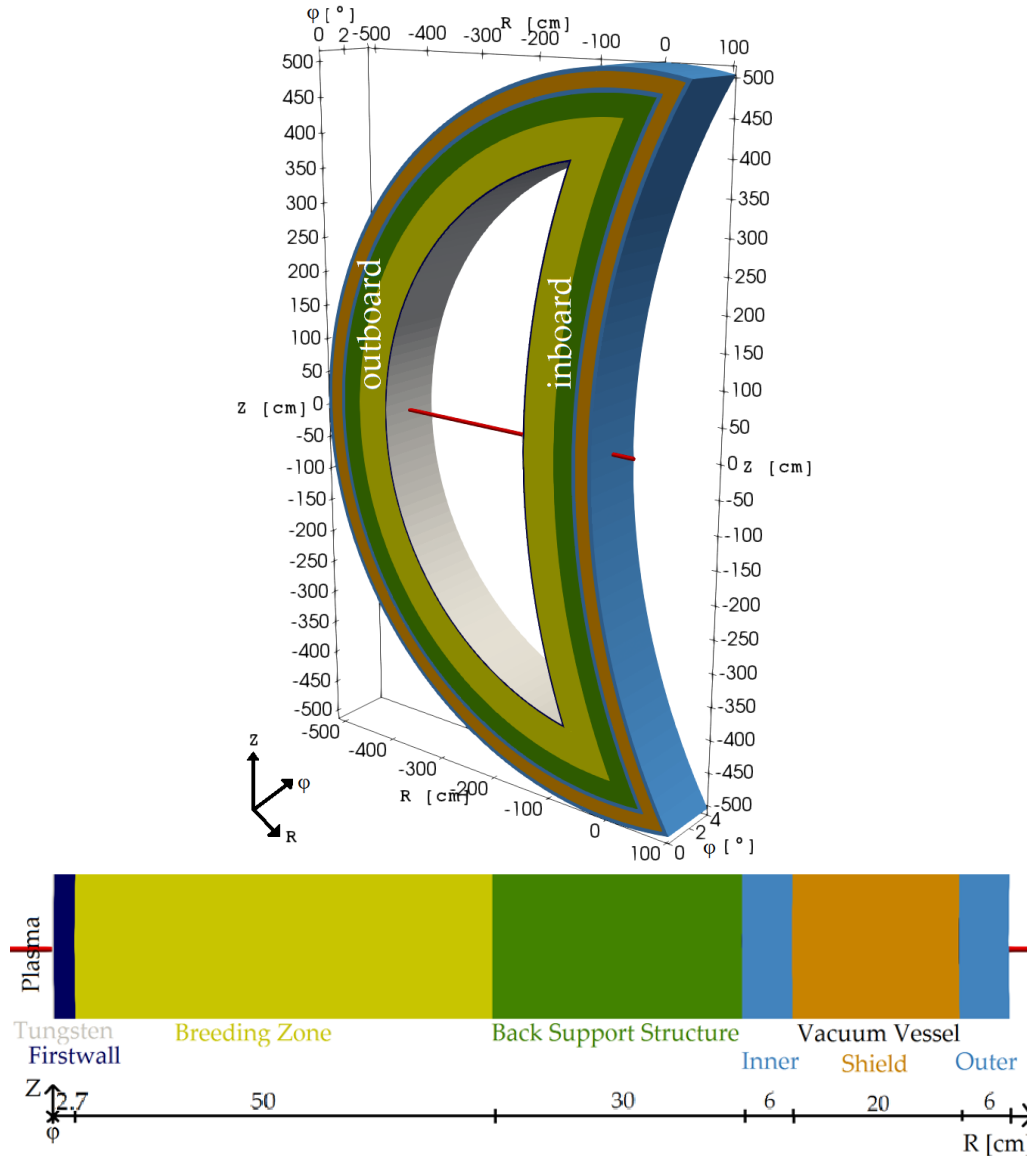


Figure 4.1: Sketch of the simplified CAD geometry and its dimensions used for the geometry verification. Red line, from  $R = -520$  cm to  $R = -30$  cm at  $z = 0$  cm,  $\varphi = 2^\circ = 50$  cm, indicates the mesh tally locations covering inboard and outboard side to obtain the neutron fluence.

The layers in table 4.1 represent the first preliminary geometry set-up for the HE-LIAS 5-B and filled with a homogenised material mixture, taken from [Spa16]. For the breeding zone, the HCPB BB concept [Per17] [Her17] is assumed as one option and represented in the verification geometry. The back support structure is a mixture of the back plate, made of low activation steel, and the manifold. It thus contains mostly steel with a lower density to take the cooling channels into account. As shielding layer inside the vacuum vessel, a mixture of 40 % water and 60 % stainless steel is assumed [Hä17].

Table 4.1: Radial build, layer thickness presented in R direction, of the verification geometry at mid-plane,  $z = 0$  cm, from plasma to outside at inboard and outboard side. The colour scheme is applied to all figures using this geometry.

| THICKNESS [CM] | COMPONENT / MATERIAL   | COLOUR IN FIGURE 4.1 |
|----------------|------------------------|----------------------|
| 0.2            | Tungsten Armour        | grey                 |
| 2.5            | First Wall             | dark blue            |
| 50             | Breeding Zone          | yellow               |
| 30             | Back Support Structure | green                |
| 6.0            | Inner Vacuum Vessel    | light blue           |
| 20             | Vacuum Vessel Shield   | orange               |
| 6.0            | Outer Vacuum Vessel    | light blue           |

A bounding box, needed for all geometry transfer approaches, is created around the geometry. The planes at  $\varphi = 0^\circ = 0$  cm and  $\varphi = 4^\circ = 100$  cm are set as reflecting surfaces. Outside the bounding box is the MCNP graveyard region.

The result of the geometry transfer with three different approaches is presented in table 4.2. Herein, the quality criteria between the original CAD representation and the converted MC geometry has been focused on the volume consistency between CAD and resulting MC geometry. Additionally, the lost particle rate is investigated during the model generation.

Table 4.2: Application of three different CAD to MC geometry transfer approaches to the simplified geometry.

| CSG   | CAD TO MC GEOMETRY TRANSFER   |  |
|---|---|--|
|   | UM  | DAGMC  |
| <ul style="list-style-type: none"> <li>• CAD geometry decomposition</li> <li>• geometry translation with McCad [Lu14]</li> <li>• volume check: less than 1 % deviation between CAD and CSG geometry</li> <li>• no lost particles per <math>10^7</math> histories</li> </ul> | <ul style="list-style-type: none"> <li>• ANSYS Workbench [Ans18] used to generate <math>3 \times 10^4</math> tetrahedral mesh elements</li> <li>• volume check: less than 0.1 % deviation between CAD and UM geometry</li> <li>• no lost particles per <math>10^7</math> histories</li> </ul> | <ul style="list-style-type: none"> <li>• Trelis [Cor20] used to generate faceted geometry</li> <li>• imprint, merge and seal the geometry</li> <li>• volume check: less than 1 % deviation between CAD and DAGMC model</li> <li>• no lost particles per <math>10^7</math> histories</li> </ul> |

The volume deviations between the CAD and the MC model, mentioned in table 4.2, are obtained for all cell volumes. Most difficult to transfer has been the tungsten armour with its 2 mm layer thickness. Such a thin layer with a large surface of  $\sim 8$  m<sup>2</sup> inboard and  $\sim 11$  m<sup>2</sup> outboard side caused the highest deviations between the CAD

and the MC model. The volume deviation of less than 1 % for CSG and DAGMC, and less than 0.1 % for UM, are acceptable to use the models for the verification calculation.

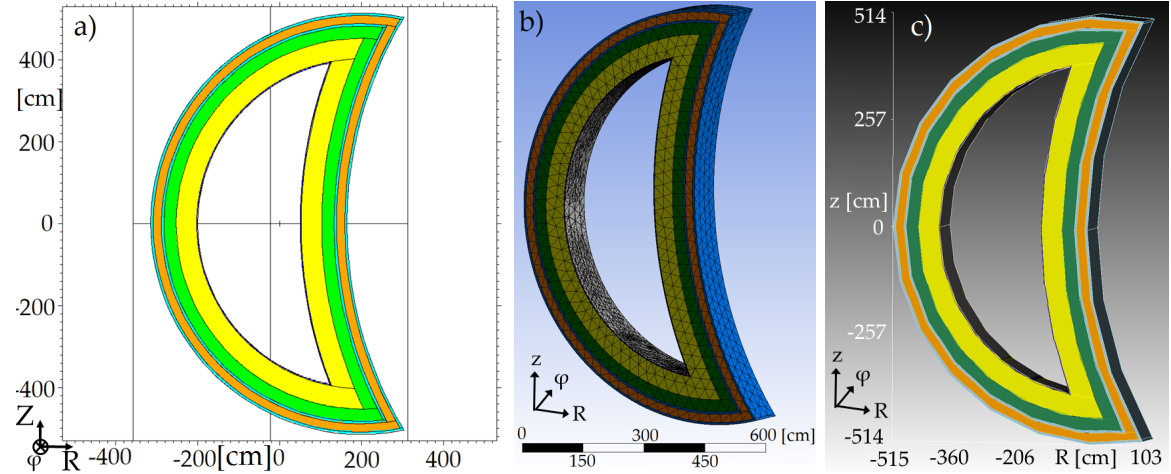


Figure 4.2: Sketch of the resulting geometry in (a) CSG, (b) Unstructured Mesh and (c) DAGMC representation. The material colouring refers to table 4.1.

## 4.2 Neutron source for the verification geometry

A volumetric cylindrical 14.1 MeV neutron source has been developed for the verification calculations which has a total depth of  $\varphi = 4^\circ = 100$  cm in toroidal direction. A minimum distance of 10 cm between the tungsten layer and the neutron source has been considered, which represents the same minimum distance as in the HELIAS geometry. In total, four different neutron emission probability areas are defined in the source to represent a similar behaviour as the plasma source of the HELIAS 5-B [Hä16]. The size and the emission probability of the separate areas are presented in table 4.3 and its position inside the geometry is illustrated in figure 4.3.

Table 4.3: Radial extension from the source centre and corresponding emission probabilities of the verification source.

| RADIAL EXTENSION FROM SOURCE CENTRE [cm] | CORRESPONDING EMISSION PROBABILITY |
|--|------------------------------------|
| 0.00 – 11.5                              | 0.50                               |
| 11.5 – 46.0                              | 0.30                               |
| 46.0 – 80.5                              | 0.15                               |
| 80.5 – 115.0                             | 0.05                               |

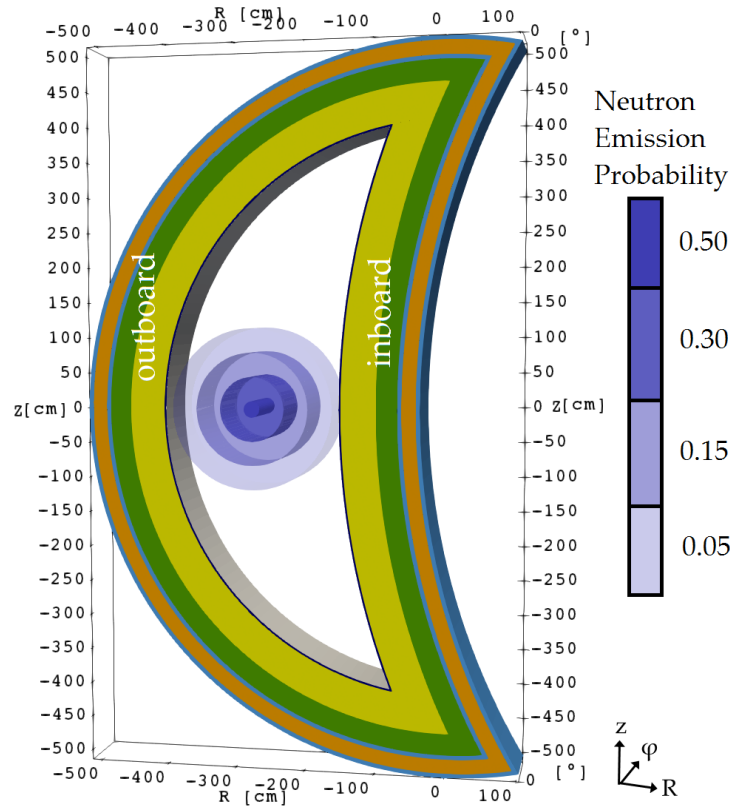


Figure 4.3: Neutron source with corresponding neutron emission probability inside the verification geometry at the RZ plane at  $\varphi = 0^\circ$ , the material colouring refers to table 4.1.

### 4.3 Computation and Results

In the unstructured mesh geometry, only a limited number of standard tallies in MCNP6 are supported. These are cell tallies for ‘Flux averaged over a cell’ and ‘Energy deposition averaged over a cell’ [Mar14]. In addition to the cell tallies, two different mesh tallies are superimposed over the geometry during the simulations. One mesh tally covers the whole verification geometry with a resolution of  $1 \times 1 \times 1 \text{ cm}^3$ . The other mesh tally is parallel to the R axis from  $R = -520 \text{ cm}$  to  $R = -30 \text{ cm}$  and crosses the  $\varphi$  axis at  $2^\circ = 50 \text{ cm}$  and the Z axis at  $0 \text{ cm}$ . It has also a resolution of  $1 \times 1 \times 1 \text{ cm}^3$  and is indicated as red line in figure 4.1. In order to get tally results for all single material zones, the cell tallies are applied on all of the 14 solids of the geometry. The obtained tally results are compared to each other to find differences in the results between the different MC geometries.

In total  $10^9$  particle histories are used in each calculation, and significant differences in the computational time have been obtained. The CSG method needs  $\sim 2.9 \times 10^4$  CPU minutes, UM  $\sim 5.7 \times 10^4$  CPU minutes and DAGMC  $\sim 5.8 \times 10^4$  CPU minutes.



This is a factor of two higher computational time of UM and DAGMC geometry description compared to the calculations with the traditional CSG geometry.

In figure 4.4 the neutron fluence per source neutron and the corresponding relative error in the whole verification geometry is shown. The results presented are on the RZ plane at  $\varphi = 2^\circ = 50$  cm.

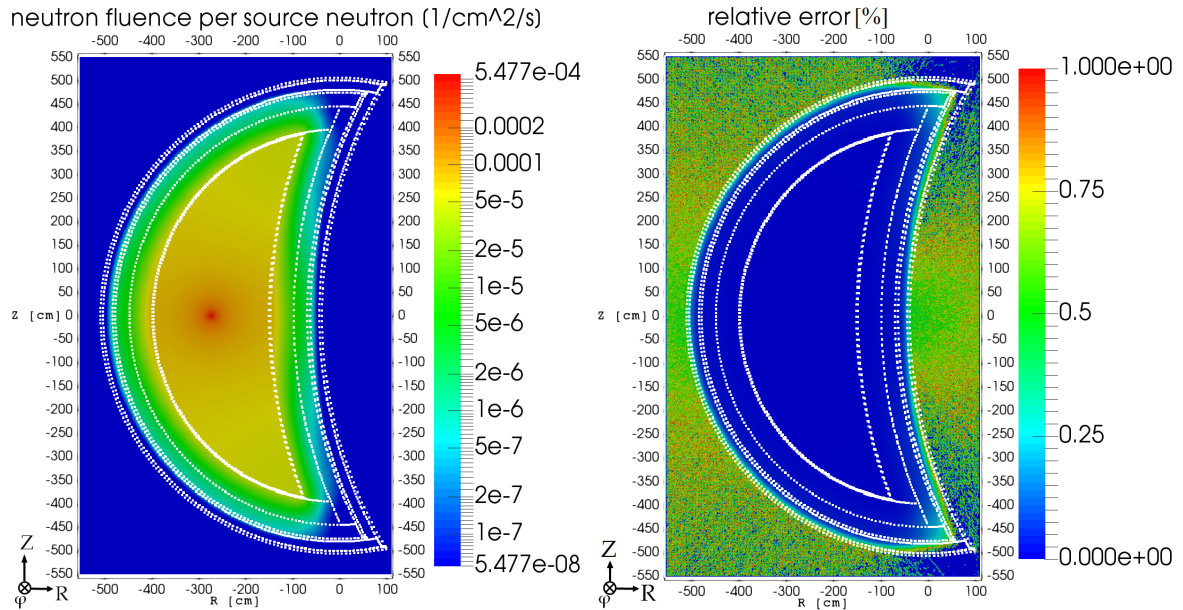


Figure 4.4: Neutron fluence per source neutron at the RZ plane at  $\varphi = 2^\circ = 50$  cm, and corresponding relative error in the verification geometry calculated with the CSG model.

The distribution of the neutron fluence shows a peak in the centre of the neutron source with its attenuation in direction from the plasma chamber to the vacuum vessel. The homogenised material compositions show a decreasing of the neutron fluence in each material layer. In the regions far away from the neutron source, the neutron fluence is lower which is an effect of neutron interaction with the material, like scattering and capture. The described behaviour can be seen for the outboard side in figure 4.5 and for the inboard side in figure 4.6. Both figures show the neutron fluence along the straight at  $z = 0$  cm as a function of the radial distance from the first wall, indicated in figure 4.1. It can be seen that the neutron fluence is decreasing from the plasma side towards the vacuum vessel by almost five orders of magnitudes. The profile is related to the radial build, mainly to the layer thickness and the material composition, as shown above. The radial thickness at the investigated outboard and inboard position is the same, therefore the neutron fluence in figure 4.5 and figure 4.6 shows the same trend. The calculated values at both positions are comparable within their statistical uncertainties.

It is noted that all three investigated geometry translation methods yield identical results within the statistical uncertainty. The small differences of DAGMC in the vacuum vessel's outer layer compared to CSG and UM are related to the use of different MCNP versions. The results of DAGMC can be reproduced by running the CSG geometry with MCNP5.

The results for the cell tallies show basically the same behaviour with nearly identical results between all three investigated methods. The largest difference can be detected in the tungsten layer in the outboard side between CSG and UM method. For the flux tally a difference of 1.75 % and for the heating tally a difference of 1.58 % has been obtained. All other differences between the methods are much smaller and negligible with respect to the corresponding relative error.

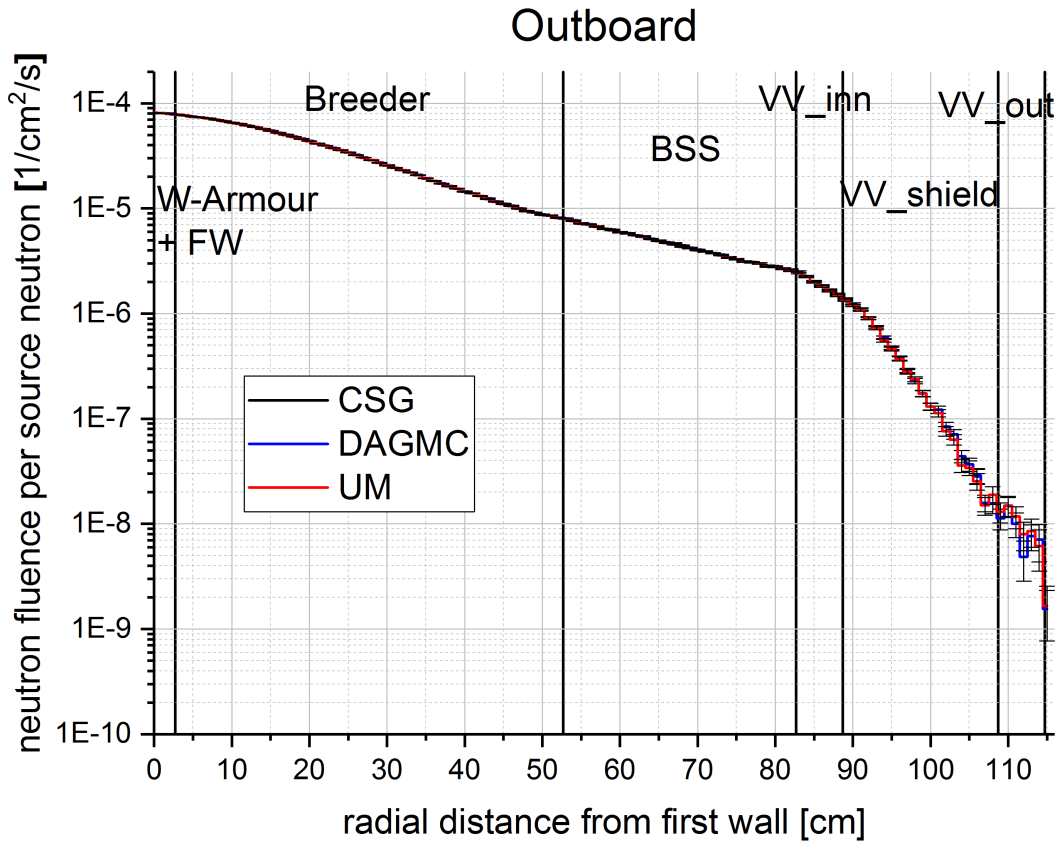


Figure 4.5: Calculated neutron fluence per source neutron as a function of the radial distance from the first wall, including relative statistical error [%], at the outboard side of the verification geometry at position  $z = 0$  cm,  $\varphi = 2^\circ = 50$  cm, and the radial point 0 cm in the graph refers to the position  $R = -400$  cm in figure 4.1. Results are presented as function of the radial distance from the first wall.

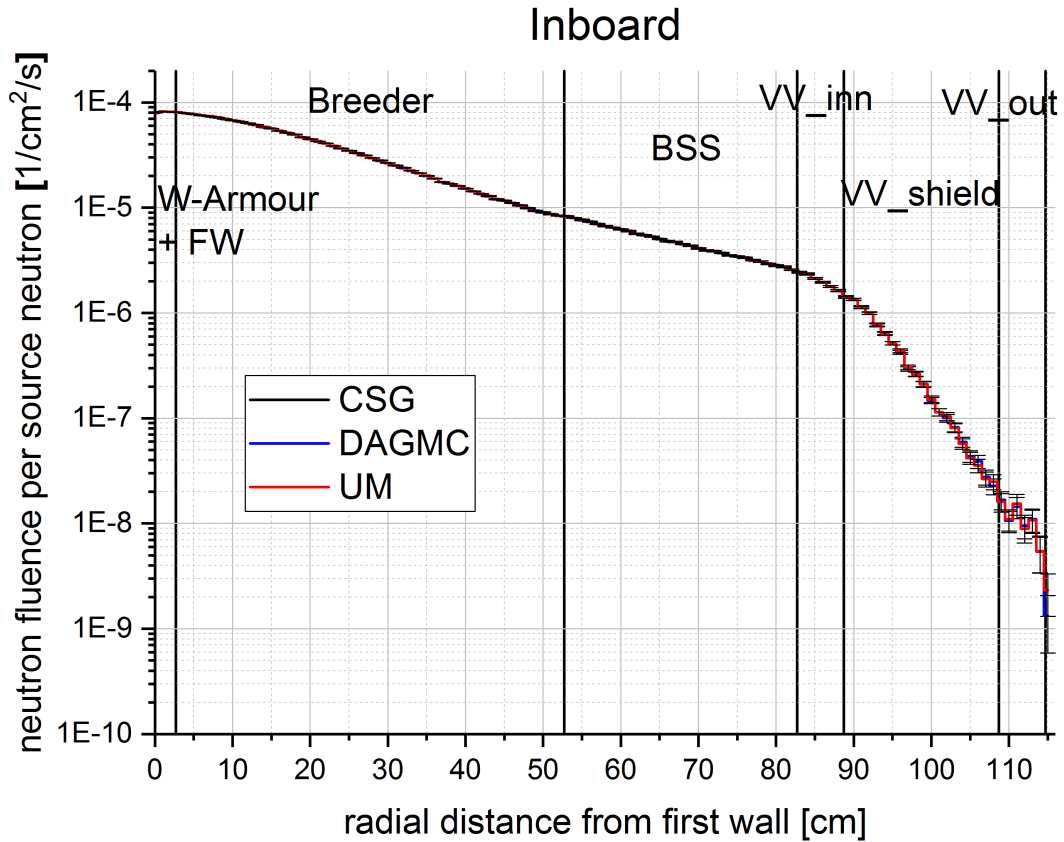


Figure 4.6: Calculated neutron fluence per source neutron as a function of the radial distance from the first wall, including relative statistical error [%], at the inboard side of the verification geometry at position  $z = 0$  cm,  $\varphi = 2^\circ = 50$  cm, and the radial point 0 cm in the graph refers to the position  $R = -150$  cm in figure 4.1. Results are presented as function of the radial distance from the first wall.

## 4.4 Conclusion of the investigated approaches

Three different geometry transfer approaches for the generation of a CAD based MC geometry representation for nuclear analyses have been investigated and successfully tested on a simplified geometry model. The result of the method verification is that comparable neutronic results within statistical uncertainties can be obtained with all three translation approaches, despite significant differences in the geometry set-up. Differences between the methods are found in the supported tallies and in the computational time needed to generate the requested results. The DAGMC approach is currently the preferred method, because it can handle very complex CAD models and it supports all tally types of MCNP. The differences in the computational time are, with respect to the benefits of DAGMC, tolerable.

# Chapter 5

## Neutron Source development for HELIAS

The accuracy of a nuclear simulation depends strongly on the correct definition of the particle source. The fusion plasma in a stellarator is fully three-dimensional shaped, following the magnetic field lines generated by the non-planar shaped superconducting magnetic field coils. The plasma distribution must be converted into an MCNP source definition to represent the real conditions as close as possible in the nuclear simulations. This chapter presents the neutron source development for a HELIAS-type stellarator power reactor. The developed source can easily be adapted to other fusion devices. The chapter is separated into two parts. While the first part presents the development of an MCNP5 and MCNP6 user specific source description, and the second part shows its verification.

### 5.1 Procedure of the MCNP Neutron Source development

The predominant fusion reaction of the stellarator power reactor using a Deuterium-Tritium (DT) plasma is the reaction which produces a helium nucleus and a neutron with energy of approximately 14.1 MeV, shown in equation 1.1. Other fusion reactions, like the Deuterium-Deuterium (DD) and the Tritium-Tritium (TT) reaction, are not typical under the conditions of the DT fusion reaction because of their lower reaction probabilities. Therefore, only the DT fusion reaction has been considered for all upcoming investigations.

Neutrons produced in the fusion reaction are not trapped by the magnetic field, they

escape from the plasma chamber and interact with the atomic nuclei of the surrounding components. The non-planar shaped field coils model the magnetic cage, which leads to complex spatial plasma distribution in a stellarator, is challenging for the generation of a neutron source representation.

The primary distribution of the DT source neutrons is provided by the IPP Greifswald, Germany. It is generated by applying a plasma physics simulation using a transport code [Tur11] to obtain the plasma density and temperature profiles. As these quantities are assumed to be constant on magnetic flux surfaces, the neutron emission rate can be calculated using a field representation from the equilibrium VMEC code [War14]. The result of the calculation is a volumetric 3D distribution of the neutron emission rate density which is constant on each individual magnetic flux surface. To obtain the neutron emission rate, the plasma density is integrated over the magnetic flux surface coordinates which are the poloidal angle, the toroidal angle and the flux surface label [War14]. This yields a spatial 3D distribution of the emission rate with a constant value in each element. The corresponding neutron emission probability within an element is related to a source data point representing this element. The resulting data is stored in tabular form in a file which contains more than  $2 \times 10^6$  3D source points for the halfmodule of HELIAS 5-B, but can be adjusted to any accuracy if needed.

Figure 5.1 shows the source points and emission probabilities in two different vertical planes through the plasma. On the left is the bean shape side at  $\varphi = 0^\circ$  and on the right is the triangular shape side at  $\varphi = 36^\circ$ , both represent the extrema of the plasma variation in the half-module of the stellarator. The neutron emission probabilities, which varies from  $10^{-6}$  to  $10^{-16}$ , are normalised to the accumulated probability of 1.

A source description is necessary to perform calculations with MCNP. It can be provided to the code in different ways, while in this work only two possibilities are investigated and presented. The easiest and most straightforward way is to utilise the standard source definition in the MCNP input file for the problem calculation. In contrast to that is the development of a user specific source subroutine in Fortran90, which can handle a more complex source description compared to the standard source but needs to be compiled with the MCNP source code.

In both cases it is required to give source specifications like particle type, starting point, energy and weight of the particle. Additional information like angular distributions or emission probabilities can also be specified in the source description.

The user specific source description approach is mainly used in this work, because the plasma distribution in the stellarator reactor is not possible to model as a standard

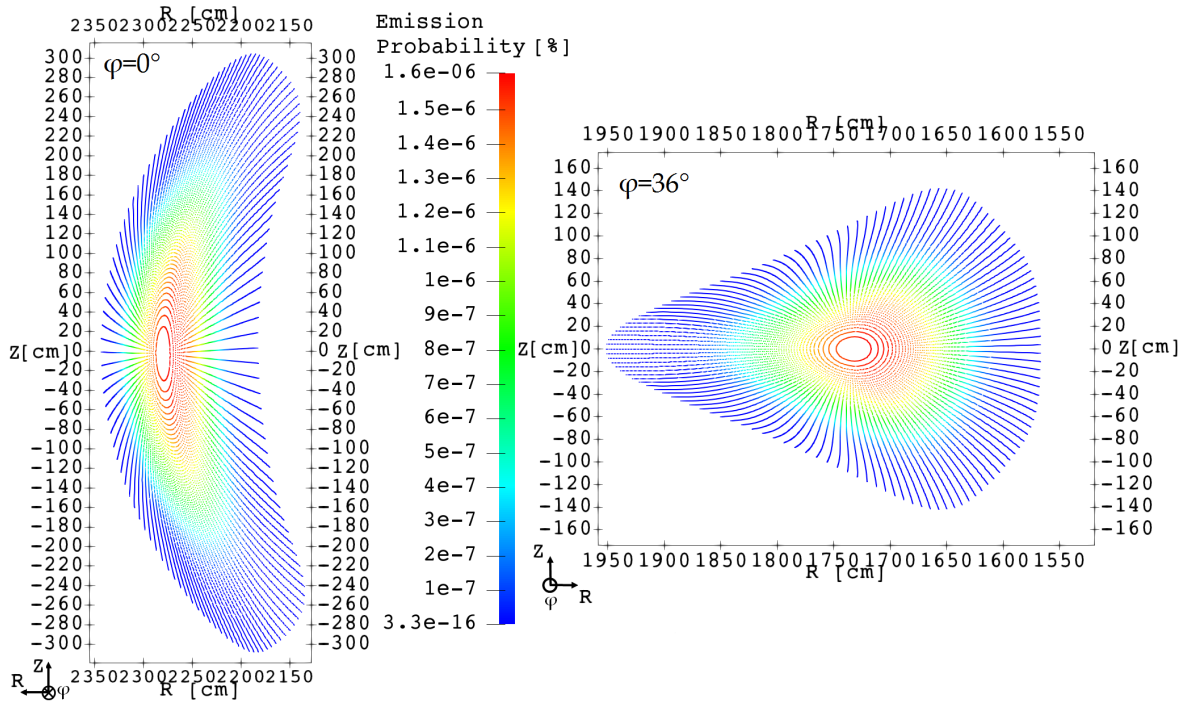


Figure 5.1: Emission Probability of the source perpendicular to the toroidal angle  $\varphi$  at the bean shape ( $\varphi = 0^\circ$ , left) and triangular shape ( $\varphi = 36^\circ$ , right) side.

source definition in MCNP. The major restrictions of the standard source definition are that it cannot describe the shape of the stellarator plasma and it does not allow the import of external data. In contrast to that, the user specific source subroutine reads and processes the external stored data from plasma physics calculation. For the source point sampling procedure, the Cumulative Probability (CP) of the emission probability is calculated and each value of the CP is associated with its corresponding source point. This approach allows the sampling of the source position through the CP. Each CP can be seen as a specific bin for one source point. A larger CP leads to a larger bin width for one specific point and to a higher sampling frequency of regions with a higher emission probability.

Figure 5.2 compares the CP for the emission of source neutrons in HELIAS 5-B as obtained from the emission rates provided with the plasma physics calculation and represented with the developed sampling algorithm in a Fortran90 program for the source subroutine. It is shown that both graphs fit perfectly to each other. The CP distribution as represented with the sampling algorithm can thus be used with confidence in the source subroutine and neutronics calculations for HELIAS 5-B.

Two different search algorithms, to find the correct CP, are compared to improve the search speed inside the source subroutine. These are the linear search and the binary

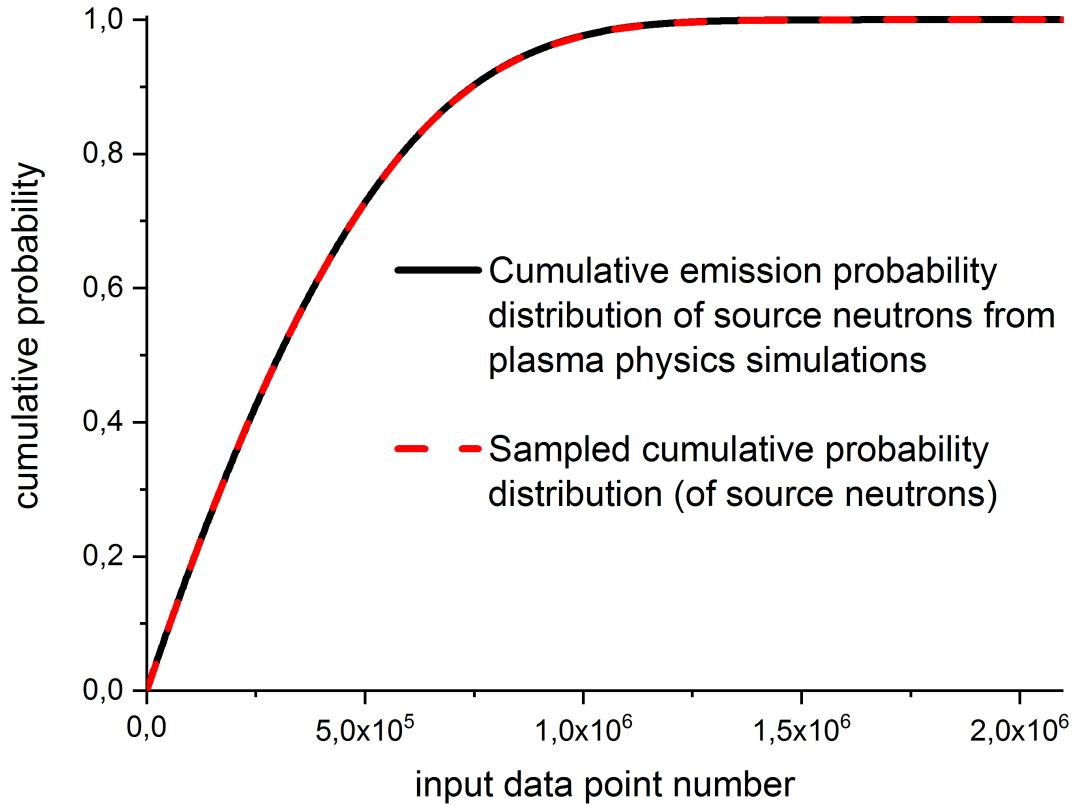


Figure 5.2: Cumulative probability for the neutron emission in HELIAS 5-B: plasma physics simulation vs. source sampling algorithm. The input data point number refers to the plasma distribution of HELIAS 5-B with more than  $2 \times 10^6$  3D source points [Hä16].

search. The linear search is a straightforward search starting each search operation with the first value in the array, while the binary search is a half interval search and starts in the middle of an interval between a lower and an upper bound. The linear search has no requirements with respect to the provided data, while the binary search needs a sorted list from lowest to highest value which is guaranteed by the calculation of the CP.

Figure 5.3 presents a visualisation of both investigated search algorithms, with an example of searching the value 10 (red) within a sorted, equidistant array of 16 elements. Both algorithms are tested in a dedicated Fortran90 program before implementing them to the source subroutine. The target of the test has been to return the array position of the CP in an output file. A Random Number (RN) generator, used for providing the search value, is addressed in the program with the same start random number and the same randomisation factor to provide the same boundary conditions for both search algorithms. In total, more than  $2 \times 10^6$  RN have been calculated to search the corresponding CP and write its array position in an output file. Both

search algorithms have produced the same output file, but with a significant runtime difference showing that the binary search is more than 22 times faster. Due to this reason, the binary search has been used for the development of the user specific stellarator source subroutine for MCNP.

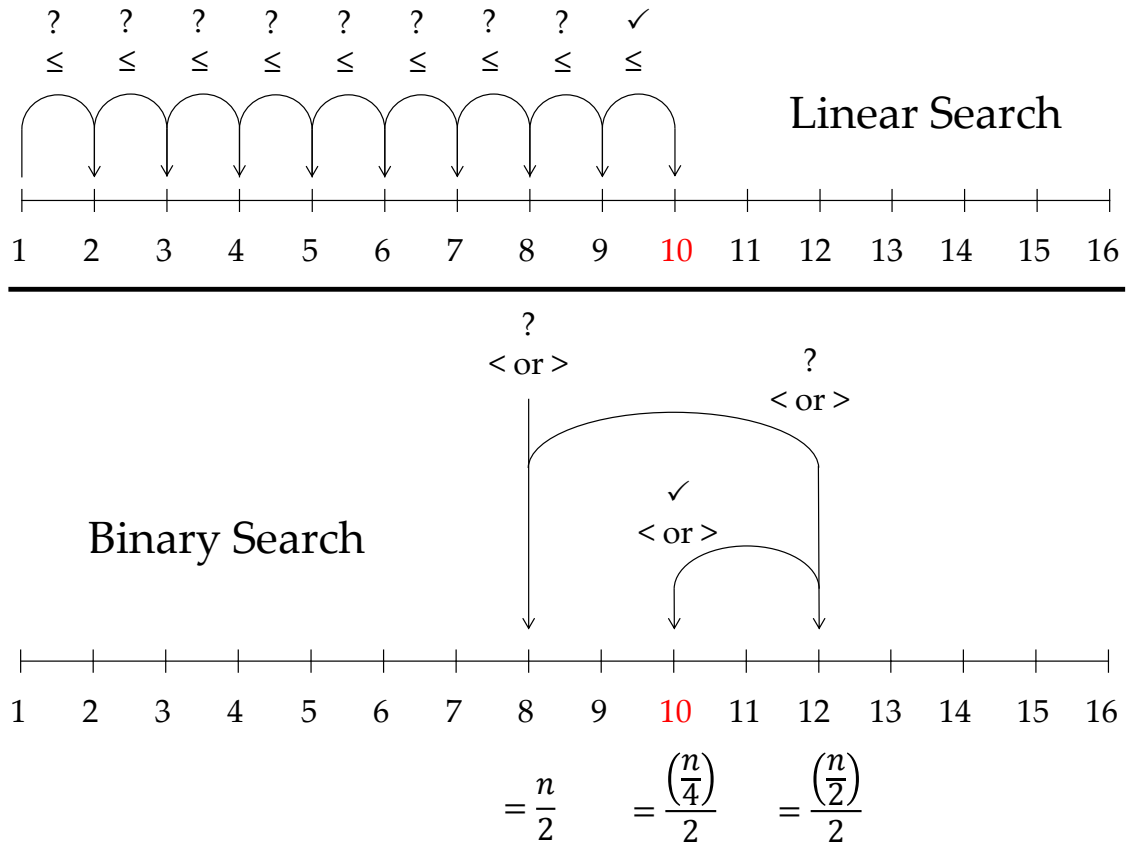


Figure 5.3: Comparison of linear search and binary search algorithm with the example of searching the value 10 (red) within a list of 16 sorted elements.

Figure 5.4 shows a schematic representation of the source sampling algorithm that is implemented in the user specific source subroutine for HELIAS 5-B. The external data as result of the plasma physics calculation is read and processed. During the processing step, the source points are stored in the computer memory and the emission rates of the original data is processed into a CP and is stored in the memory as well. This procedure is carried out only once and the data is stored in the memory for the whole execution of the neutronics calculation. All following steps are repeated for each emitted neutron.

Each source point assignment starts with the generation of a RN in MCNP, which is needed in the search loop to find the corresponding CP. Inside the search loop  $n$  represents the total number of elements in the CP and is an important information



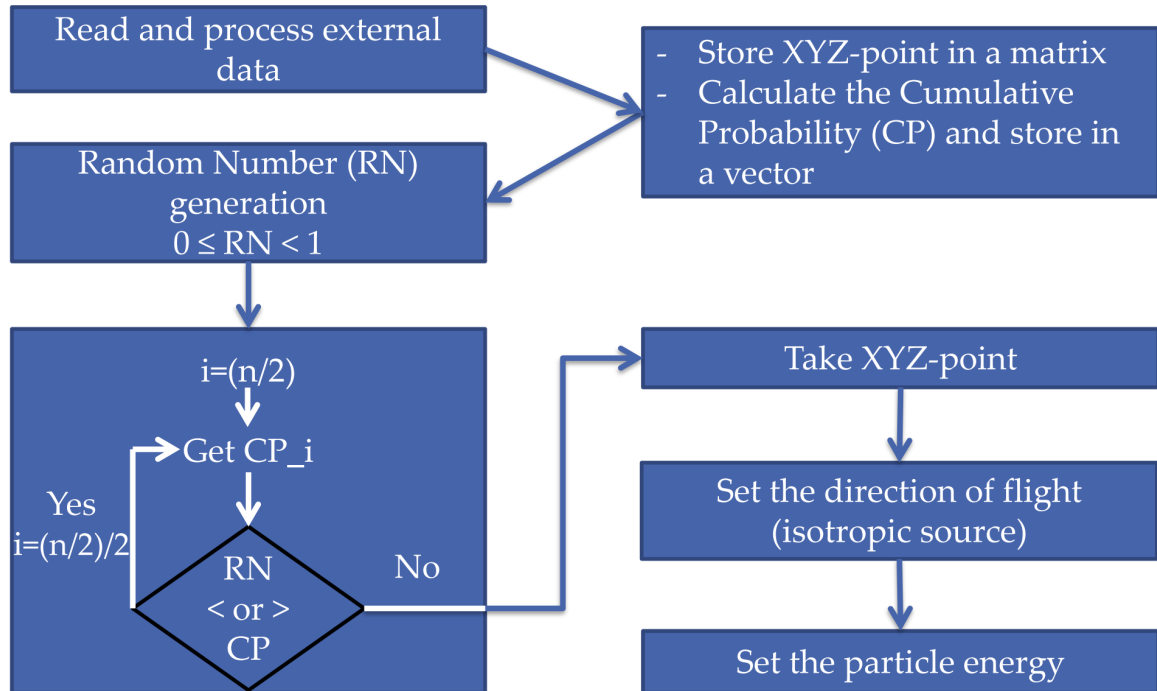


Figure 5.4: Schematic representation of the neutron source sampling implemented in the user specific MCNP source subroutine for 3D stellarator specific geometry, while  $n$  in the search algorithm represents the total element number of the Cumulative Probability [Hä16].

for the binary search algorithm. The control variable ‘ $i$ ’ is set equal to  $(n/2)$  at the beginning and the search algorithm starts. If the RN at position ‘ $i$ ’ of the CP is smaller or greater, ‘ $i$ ’ will decrease by  $(n/2)/2$  and the binary search jumps to the next search interval. This loop runs until a CP is found which is larger than the RN, but its precursor is smaller than the RN, and no jump to a new search interval is possible. At that point ‘ $i$ ’ is used to fetch the corresponding source point in the matrix stored earlier.

The source point thus found is defined as emission point for a neutron. The direction of flight is set automatically by MCNP assuming an isotropic distribution of the neutron emission at each source point. Finally, the initial neutron energy is set to an energy of 14.08 MeV and the particle transport calculation in MCNP for the sampled neutron starts.

## 5.2 Verification of the MCNP Neutron Source Subroutine

The developed MCNP source subroutine needs to be tested and verified before it can be applied for neutronic calculations of HELIAS. The test has to show an agreement of the normalised frequency of the source point sampling in MCNP, and the emission probabilities as given by the plasma physics calculation.

For the test, a simple void sphere has been used that covers the whole plasma volume. To obtain the sampling frequency on each source point, the capability of MCNP in recording the emission point of a particle has been utilised.  $10^9$  particles have been sampled and their emission points are detected, which are preserved in an MCNP output file with a data size of  $\sim 115$  GB. To carry out the comparison, the sampling frequency of each emission point is processed from the file and divided by the total number of sampled particles. This value is termed emission frequency.

In figure 5.5, the MCNP calculated frequency per neutron history (emission frequency) is plotted against the emission probability of the original data. The emission frequency is an integer value of  $n/\text{Number of sampled particles}$ , where  $n$  is the number of hits (frequency) of one source point. This results in discrete steps that are visible in the low frequency region.

Additionally, a linear fit of the emission frequency is also shown in the diagram. The gradient of the linear fit is  $0.99997 \pm 2.4 \times 10^{-5}$ . The linear fit confirms the expectations of equality between the emission frequency and the original emission probabilities.

This verification calculation has been performed for two different MCNP versions, MCNP5 1.60 [MCN03] and MCNP6 1.0 [Goo12]. The results of the verification calculations from both different code version match completely, while using the same random number generator and the same random number seed. This means that the user specific source subroutine can be used both in MCNP5 and MCNP6 for neutron transport calculations.

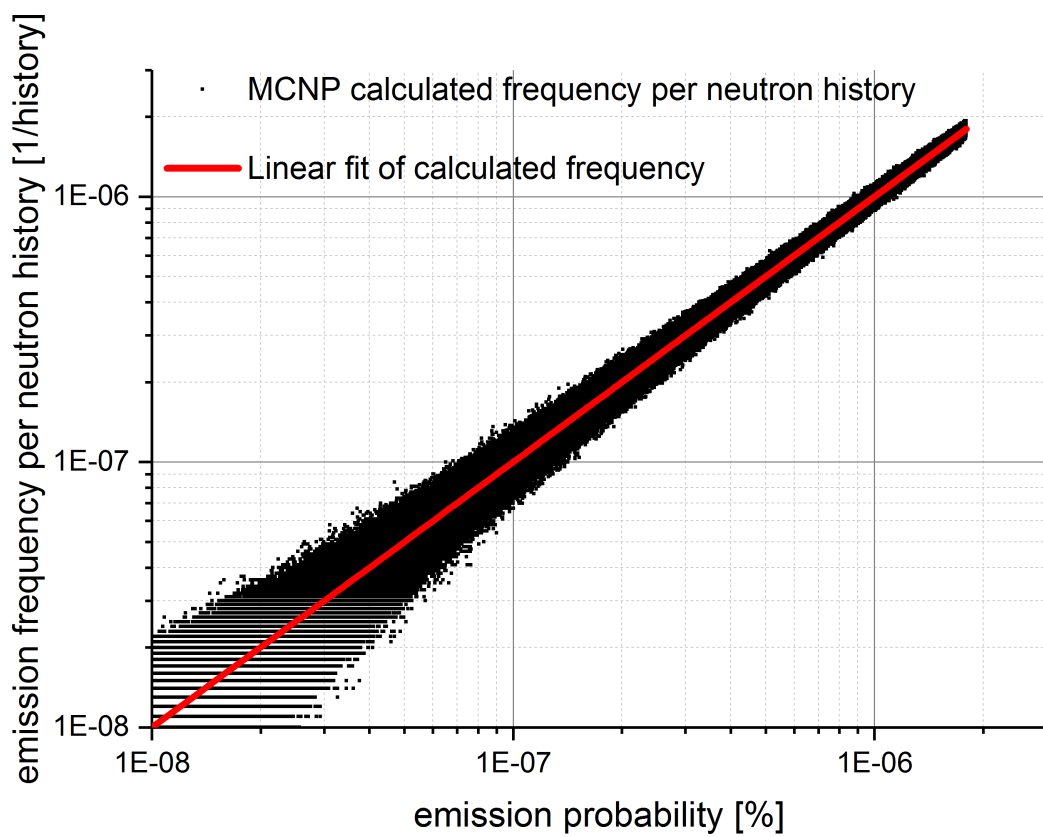


Figure 5.5: Calculated emission frequency of the MCNP source positions as a function of the original emission probability [Hä16].

# Chapter 6

## Variance Reduction Technique applied to the Stellarator

Variance Reduction (VR) techniques improve the decrease of the relative statistical error during the generation of calculation results in MCNP significantly. The application of these techniques target to provide reliable results in areas far away from the plasma chamber. A few selected VR techniques are discussed here for its application to the stellarator. For this purpose, the simplified stellarator geometry is used mainly to get a better understanding of the non-analogue MC technique. Parts of this chapter are published in [Hä18a].

### 6.1 Identification of suitable Variance Reduction Techniques

An analogue simulation, without applying the VR technique, typically requires an increase of the emitted source particles to get an acceptable relative statistical error in areas far away from the source region. This approach leads to a massive increase of the computational effort and though probably not to sufficient statistics in such regions. The target of VR techniques is a decrease of the relative statistical error for the nuclear design calculations in the area of interest and simultaneously a not significantly increase of the computational effort.

The question is: How to identify and proof an adequate variance reduction technique to apply for the stellarator? In total, three criteria are taken into account to judge the suitability:

1. computational time,

2. number of source particles,
3. relative statistical error in the tally.

The computational time and the number of emitted particles are easily adjustable in the MCNP simulation. Instead of that, the relative statistical error needs to be read at the output data after each successfully performed MCNP simulation. This means that only an iterative approximation of the relative statistical error can be done which is a very time consuming task. It must be decided if an additional continue run is needed after each calculation and which break-off criteria are suitable to choose. These criteria can be either additional computational time or a larger number of emitted particles.

Several different VR techniques can be applied in MCNP. Here, the cell based importance sampling technique with particle splitting / Russian Roulette and the super imposed mesh based weight window method are investigated.

## **6.2 Application of cell based importance sampling technique to the CAD verification geometry**

The cell based importance sampling technique with particle splitting / Russian Roulette and manual specification of the cell importance is a straightforward applicable VR method. The layered construction of the stellarator and no angular dependency of the plasma source offers the adaptation of this method. Solid cells close to the plasma chamber have a lower cell importance compared to regions far away. MCNP will automatically split particles entering from a lower cell importance to a higher and lowering the weight of each particle while preserving the total weight of the original particle and distribute it equally to the newly generated during these operations. The particle split / weight adjustment only takes place in material cells. The particle splitting has the advantage that a higher number of particles can contribute to the result in areas far from the plasma chamber and therefore decrease the relative statistical error. This method provides a good particle splitting, if the step from one cell importance to another is not too large. The general approach is to increase the number of emitted particles as the particle population decreases across a distance, which corresponds to the average mean free path of a neutron. Instead, it is possible to choose the increase of the cell importance from one cell to the neighbouring cell not larger then by a factor 4 [MCN03]. The higher this difference, the more particles are generated when crossing the cell boundary. This might generate results with low relative statistical error, but

with an extraordinary high particle population and biased tally results when applying a too large step size. The particle population should be equally distributed in the whole geometry.

The neutron flux and its corresponding relative error on the outboard side in the CAD verification geometry, seen in figure 4.5 and figure 4.6, can be used to investigate the change of the solid cell importance. The decrease of the neutron flux and simultaneously increase of the corresponding relative error is typical for an analogue simulation without using VR methods. It can be seen that the neutron flux decreases in the breeding layer and the back support structure by one order of magnitude, respectively. The decrease in the vacuum vessel shielding layer is the largest by approximately three orders of magnitude. The rise of the relative statistical error in areas beyond the back support structure can be investigated and indicates that a lower number of particles contributes to the result. These are the regions of interest to apply variance reduction methods, because the particles are guided in these areas to lower the relative statistical error.

Different solid cell importance settings are considered for applying a cell based variance reduction technique in this work. The general approach is to obtain a homogeneous distributed neutron population and thus increase the cell importance in a way as the neutron flux decreases. Two of the options are applied to the geometry in figure 4.1 without additional cell splitting, and one option is applied with additional cell splitting of 5 cm in the breeding zone, back support structure and vacuum vessel shield. Each of these options uses an increase of the cell importance by a fixed factor. The options are: double and quadruple (original geometry), and refined (with cell splitting). As the name indicates, the cell importance increase factor for double is two, for quadruple is four, and for refined is two. An overview is shown in table 6.1.

Table 6.1: Parameter range of the different cell weighting importance choices depending on the radial material domains.

| COMPONENT              | IMPORTANCE SETTINGS |        |           |                                |
|------------------------|---------------------|--------|-----------|--------------------------------|
|                        | normal              | double | quadruple | refined                        |
| Tungsten Armour        | 1                   | 1      | 1         | 1                              |
| First Wall             | 1                   | 2      | 4         | 1                              |
| Breeding Zone          | 1                   | 4      | 16        | 1, 1, 2, 2, 4, 4, 8, 8, 16, 16 |
| Back Support Structure | 1                   | 8      | 64        | 32, 32, 64, 64, 128, 128       |
| Inner Vacuum Vessel    | 1                   | 16     | 256       | 256                            |
| Vacuum Vessel Shield   | 1                   | 32     | 1024      | 512, 1024, 2048, 4096          |
| Outer Vacuum Vessel    | 1                   | 64     | 4096      | 8192                           |

The presented cell importance changes in table 6.1 are used in different calculations with the CSG description of the CAD verification model. Material compositions, the random number generator, and all other settings stayed the same for all performed calculations. A FMESH4 tally with a resolution of  $1 \times 1 \times 1 \text{ cm}^3$  is applied to detect the neutron flux and its corresponding relative statistical error. It is indicated in figure 4.1 as red line, but only the outboard side is investigated which refers to the position  $z = 0 \text{ cm}$ ,  $\varphi = 2^\circ = 50 \text{ cm}$ , and the radial distance from first wall  $0 \text{ cm}$  to  $116 \text{ cm}$  refers to the position  $R = -400 \text{ cm}$  to  $R = -516 \text{ cm}$ . Two different run time criteria have been chosen to compare the relative statistical error of the simulations. First, a fixed number of emitted particle histories,  $N = 10^9$ , has been used and results are presented in table 6.2 and figure 6.1. Second, fixed computational time has been set to 24h on 200 CPU cores and the results are presented in table 6.3 and figure 6.2.

It can be seen in table 6.2 that the computational time increases up to a factor of  $\sim 16$  between the ‘Normal’ and ‘Quadruple’ cell importance setting. Also, a decrease of the relative statistical error between the two previously mentioned importance settings with a factor of  $\sim 66$  at the outside of the vacuum vessel at the radial distance from the first wall at  $116 \text{ cm}$  in figure 6.1 is presented. The highest decrease factor of the relative statistical error can be found between ‘Normal’ and ‘Refined’ setting with a factor of  $\sim 95$ . This means, an analogue calculation would approximately need 95 times more emitted particles to obtain the same results as in the ‘Refined’ case. This is because the relative statistical error  $R = 1/\sqrt{N}$  decreases by an increased number of starting particles. The mentioned values for ‘Quadruple’ and ‘Refined’ are significantly higher compared to the increase of computational time. In figure 6.1, the introduced cell splitting in the ‘Refined’ case is visible which corresponds to the different cell importance within one material layer.

Table 6.2: Comparison between the increases of the computational time and the decrease of the relative statistical error of the neutron flux at the outside of the outer vacuum vessel of different cell importance settings by a fixed number of particle histories.

| IMPORTANCE SETTING | COMPUTATIONAL TIME [ <i>min</i> ] | TIME INCREASE FACTOR [compared to ‘normal’] | RELATIVE ERROR AT OUTSIDE ‘VV_OUT’ | ERROR DECREASE FACTOR [compared to ‘normal’] |
|--------------------|-----------------------------------|---|------------------------------------|--|
| normal             | $2.4 \times 10^5$                 | 1   | 0.50382                            | 1  |
| double             | $9.9 \times 10^5$                 | 4.13  | 0.05932                            | 8.49   |
| quadruple          | $4.0 \times 10^6$                 | 16.67                                       | 0.00769                            | 65.52  |
| refined            | $2.1 \times 10^6$                 | 8.75  | 0.00529                            | 95.24  |

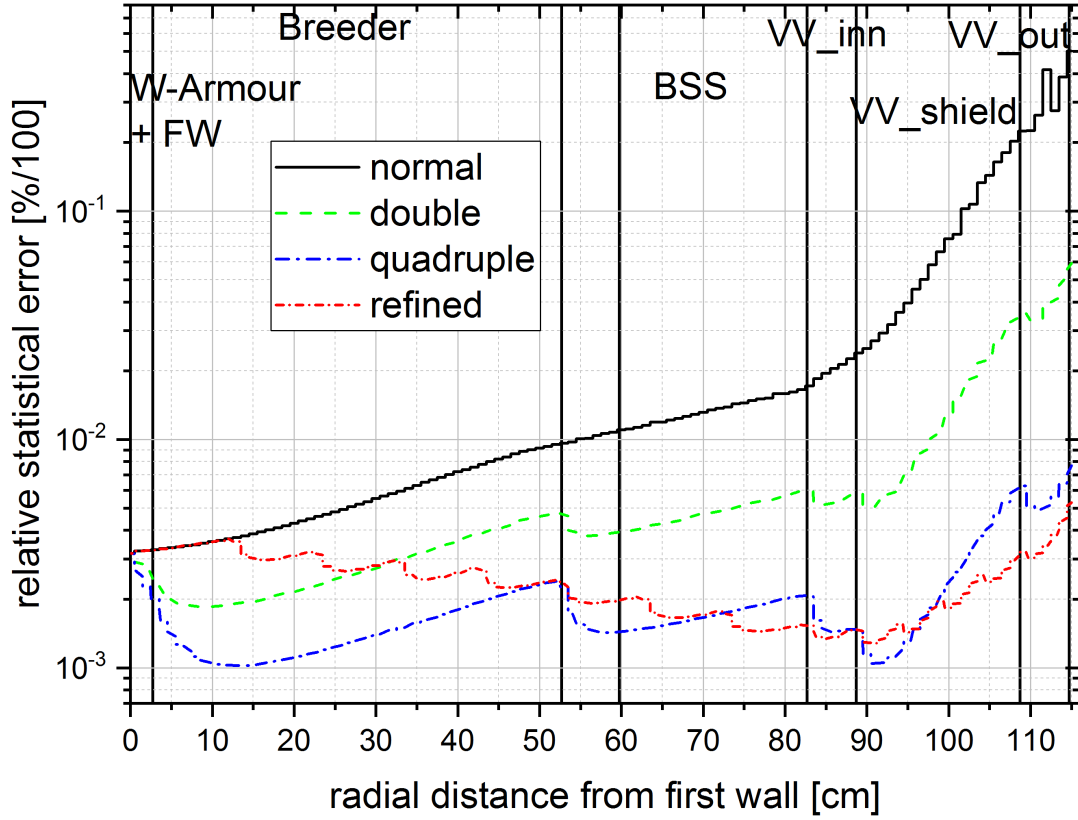


Figure 6.1: Computed relative statistical error at the outboard side of the MCNP calculation using three different weighting schemes with  $10^9$  source particles as a function of the radial distance from the first wall in the plane  $z = 0$  cm,  $\varphi = 2^\circ = 50$  cm,  $R = -516$  cm to  $R = -400$  cm indicated in figure 4.1.

Nevertheless, the comparison of the computational time with a fixed amount of starting particles is not the best-suited criteria. If the VR method is applied sufficiently for the calculation, it can decrease the relative statistical error in less computational time, but this is not a main criterion in the selection of the best-suited approach. The second approach investigates a fixed computational time to  $t = 2.88 \times 10^5$  min, which represents 24 h on a cluster with 200 CPU cores, to compare the evolution of the relative statistical error. The result is shown in table 6.3 and figure 6.2.

The initial starting point, which is the radial distance from first wall at 0 cm of the curves in figure 6.2, is different for each investigated case. This is related to the different number of starting particles, shown in table 6.3. The lower the number of starting particles, the higher the relative statistical error at this position. The graph ‘Refined’ shows the same behaviour in figure 6.2 as in figure 6.1 due to the very similar amount of starting particles for this cell importance setting. It can be seen that the



graph ‘Refined’ shows its potential to decrease the relative statistical error in regions far away from the plasma, but not in regions close to the plasma, which is expected in the continuous increase of the importance setting by a factor of 2. The contrary of that is the graph ‘Quadruple’, where the relative statistical error is decreased significantly in each material layer, except in the vacuum vessel shield. This case has the advantage that no additional cell splitting is required in the material cells.

Table 6.3: Comparison between the decreases of the number of starting particles and the decrease of the relative statistical error of the neutron flux at the outside of the outer vacuum vessel by a fixed computational time.

| IMPORTANCE SETTING | NUMBER OF STARTING PARTICLES | TIME INCREASE FACTOR [compared to ‘normal’] | RELATIVE ERROR AT OUTSIDE ‘VV_OUT’ | ERROR DECREASE FACTOR [compared to ‘normal’] |
|--------------------|------------------------------|---|------------------------------------|--|
| normal             | $1.5 \times 10^{10}$         | 1   | 0.11961                            | 1  |
| double             | $3.6 \times 10^9$            | 4.17  | 0.03080                            | 3.88   |
| quadruple          | $6.6 \times 10^8$            | 22.73                                       | 0.00946                            | 12.64  |
| refined            | $1.1 \times 10^9$            | 13.64                                       | 0.00499                            | 23.97  |

The conclusion of the cell importance setting is that this method can be applied for the stellarator without any further geometry modification and helps to improve the relative statistical error in all material layers. The results show a significant difference between non-VR and VR cases. The non-VR results are not acceptable in areas far away from the plasma chamber, in respect to the MCNP quality assurance criteria. For such regions, the VR methods must be applied to generate suitable results. Furthermore, the application of VR methods decreases the computational effort needed to obtain acceptable statistics in regions far away from the plasma.

Nevertheless, this VR technique is not the preferred solution to apply for HELIAS, because a mismatch in the particle importance can happen in the complex geometry. The layers in HELIAS have some gaps, especially at the divertor openings, where the particles can hit areas with higher importance and a step-size higher than the factor 4 can be obtained. This leads to a shift in the neutron population and returns non-acceptable results. Another drawback of this method is, that it must be applied for the whole geometry without being able to specify a specific region that might be important for the neutronics investigation. The application of a mesh based weight window for VR can overcome these drawbacks and is preferred for the stellarator.

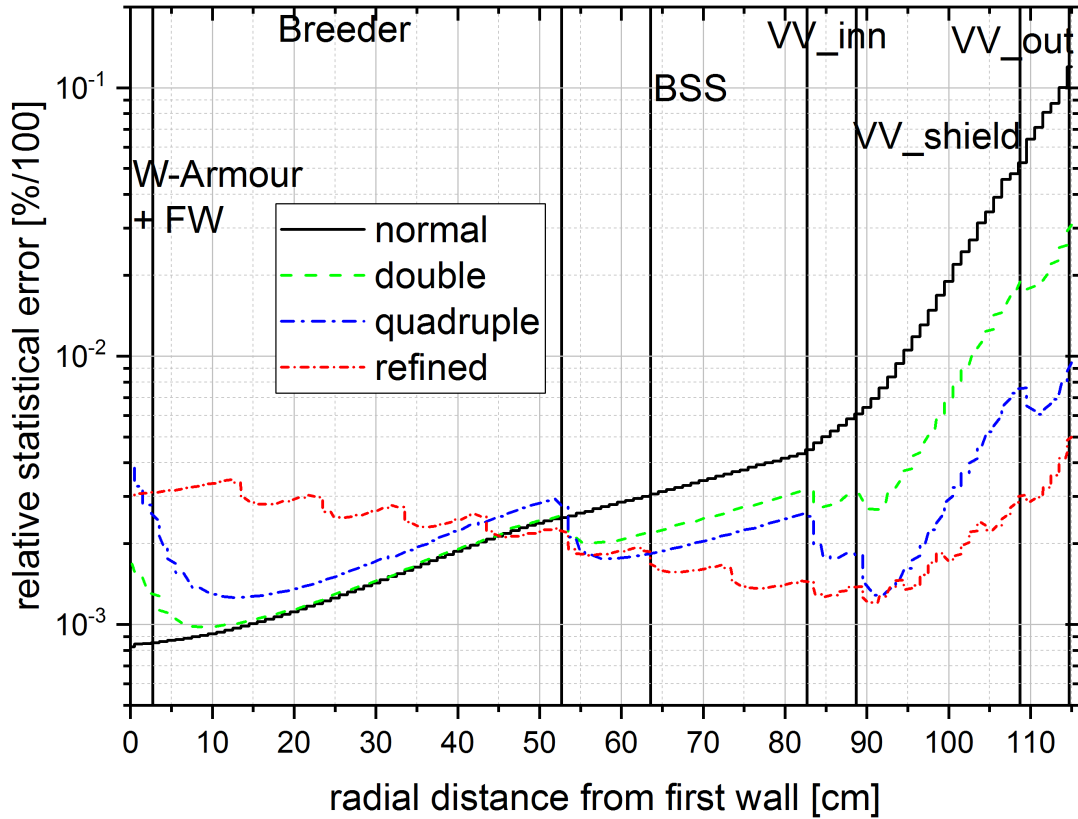


Figure 6.2: Computed relative statistical error at the outboard side of the MCNP calculation using three different weighting schemes, with 24 h computational time and 200 CPU cores, as a function of the radial distance from the first wall in the plane  $z = 0$  cm,  $\varphi = 2^\circ = 50$  cm,  $R = -516$  cm to  $R = -400$  cm indicated in figure 4.1.

### 6.3 Generation of mesh based weight windows

The generation of a weight window for a stellarator reactor is time consuming. Two different methods to generate the weight window mesh are investigated. First, the standard WW generator provided by MCNP, and second, the application of the Automated VARIance reduction Generator (ADVANTG) to benefit from an automated WW mesh generation. The usage of the standard MCNP weight window generator returned into a not applicable WW, therefore only the ADVANTG mesh is described.

The WW in this work is generated as a quadratic mesh. The bend geometry of the stellarator prevents the application of a cylindrical WW mesh. The quadratic WW mesh can be adjusted in its size to each coordinate direction, and it should be chosen as a fine mesh in the region of interest and as a coarse mesh in the regions which have minor contributions to the calculation results. This arrangement of the WW mesh

cells must be specified before generating a WW mesh. That means, the WW mesh generation is an iterative process to obtain a suitable WW mesh for application in neutronics calculations.

ADVANTG is a tool which automates the process of generating variance reduction parameters for continuous-energy MC simulations of fixed-source neutron, photon, and coupled neutron-photon transport problems using MCNP5 [Mos15]. The tool employs a deterministic transport solver to calculate the adjoint particle flux [Mos15]. This is comparable with a backwards simulation from the region of interest to the particle source. The limitation on MCNP5 implies immediately restrictions, that only CSG geometry and fixed-source problems (the MCNP standard source description), are supported. The main benefit of ADVANTG is the generation of a WW mesh in only one calculation. Therefore, no iteration calculations are needed, and the whole process is much faster compared to the standard MCNP weight window generator. A simple application of ADVANTG use for the complex stellarator geometry is not possible and a simplified approach must be utilised.

The input data for ADVANTG must be prepared, before the generation of the WW can start. ADVANTG needs, besides the definition of the WW mesh, an extra mesh which covers the area of interest. Both meshes are independent from each other in their definition, meaning their size and shape do not need to be similar. The region of interest is the area, where the WW mesh will be optimised for. It is important to know exactly the usage of the WW for the productive calculations afterwards. If this is not clear, a suitable WW cannot be generated.

Different scenarios have been analysed with ADVANTG, which represent an iterative approach to generate a suitable WW. These scenarios are a mixture out of:

- two different fixed-sources  $\rightarrow$  line source and LCFS source volume,
- two different WW mesh resolutions  $\rightarrow$  uniform and non-uniform,
- two different WW particle registration  $\rightarrow$  only neutron and coupled neutron-photon,
- two different CSG geometries to generate the WW.

These aspects are discussed to obtain a WW setting for the HELIAS shielding calculations.

Due to the restrictions of ADVANTG in using CSG geometry and a fixed source, a simple approximation of the stellarator model must be created. The HELIAS envelope CAD model is reused to convert it with McCad into CSG representation to fulfil

the ADVANTG requirements. As described before, this model is only an envelope containing one material layer and has had approximately 20% lost particles. This value is not acceptable and a clean-up in the CAD model has been needed before its conversion. It was not that important to keep the volume consistent between the original envelope model and the cleaned-up CAD model. Moreover, it was important that the cleaned-up CAD model has a very low lost particle rate and that the final shape represents the original CAD model with a deviation of less than 10%.

A CSG model has been generated exhibiting 12 lost particles per  $10^9$  starting particles when using a surrounding sphere as surface source sending the particles inside the voided geometry. The drawback of this model is, that the radial thickness of the material layer is only around 70 cm. A gap between the envelope model and the vacuum vessel outside layer of around 50 cm is seen in figure 6.3 on the left side. The gap size depends on the radial and toroidal position in the stellarator. This means that this cleaned-up model CAD model is extended to the boundary of the vacuum vessel outside layer. After successful conversion into CSG geometry, no lost particles have been obtained by per  $10^9$  starting particles. Both geometries, including the real vacuum vessel outside layer, are presented in figure 6.3.

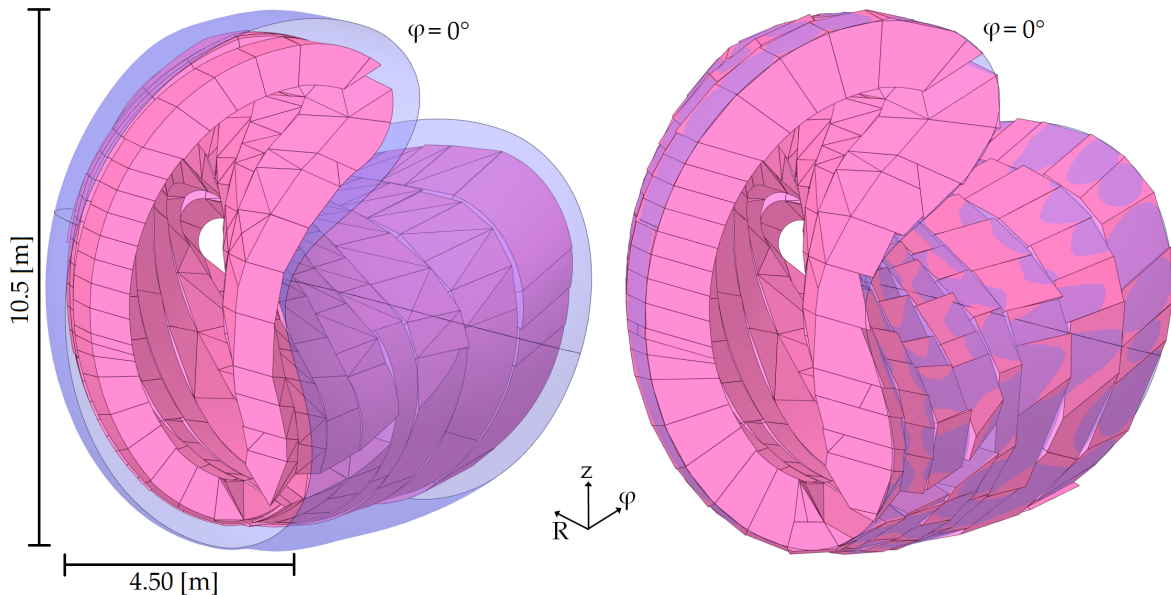


Figure 6.3: CSG geometry of HELIAS containing only one material layer, left original envelope model and right the extended model. The vacuum vessel outside layer (blue) is shown for visualisation purpose only.

A suitable material definition must be created for the one layer CSG model before using it in ADVANTG. The HELIAS reactor consists of different homogenised material mixtures, represented in table 2.5. The new material mixture contains all original

materials weighted by their volumetric representation in HELIAS. The new material has a density of  $4.487 \text{ g cm}^{-3}$  and is used to fill all material cells in the CSG model for the generation of a WW with ADVANTG.

The plasma fusion source could not be used for this approach, because it is an MCNP user specific source subroutine which is not supported by ADVANTG. A standard MCNP source must be defined instead. Two different approaches for the fixed-source definition are considered: a line source at the midplane ( $z = 0 \text{ cm}$ ) from  $R = 2200 \text{ cm}$ ,  $\varphi = 0^\circ$  to  $R = 1600 \text{ cm}$ ,  $\varphi = 36^\circ$ ; and a volumetric plasma representation using the LCFS as outside surface. Both source representations emit the neutrons equal and isotropic.

The line source is represented as cylindrical source with a radius of  $0.01 \text{ mm}$ . This source indicates immediately, that only emitted neutrons from midplane are taken into account during the generation of the WW. This is not the case inside the HELIAS plasma where the particles are emitted from whole plasma volume. The line source introduces a systematic error to the WW by underestimating the particle emitting area beside the midplane. An increase of the radius of the line source is possible up to  $\sim 50 \text{ cm}$ , a larger radius hits the material cells. This means that the line source could not be applied and a volumetric source definition is needed.

The source definition in MCNP allows to define a source cell, which sends out the particles. Another advantage is, that a volumetric source can cover this cell and this volumetric source can also cover other parts of the CSG model without influencing them. Inside the source definition can be defined, that only particles sampled in the source cell are used as source particles for the calculation. This means, other particles sampled in the volumetric source get rejected and a re-sampling starts. Regarding this feature, a second definition for the fixed-source has been created. The LCFS is used as a boundary layer with two planes at  $\varphi = 0^\circ$  and  $\varphi = 36^\circ$  to generate a volumetric representation of the source cell. A direct conversion of the source cell into CSG representation is not possible, because it is constructed with the LCFS which includes more than 5500 triangles at the surface and McCad cannot convert this solid. The simplification is therein to separate the large source cell volume into several sub-volumes and replace the triangles either with planes or cylinders. The simplified model contains at the end less than 200 planes and 21 cylindrical surfaces, separated into 25 solid bodies. McCad has the ability to create one CSG cell out of the 25 CAD solids, which can be used as source cell. The CAD model can be seen in figure 6.4.

Two different WW mesh resolutions are used, an uniform mesh with a resolution of  $20 \times 20 \times 20 \text{ cm}^3$ , and a non-uniform mesh with a higher resolution in the area of interest

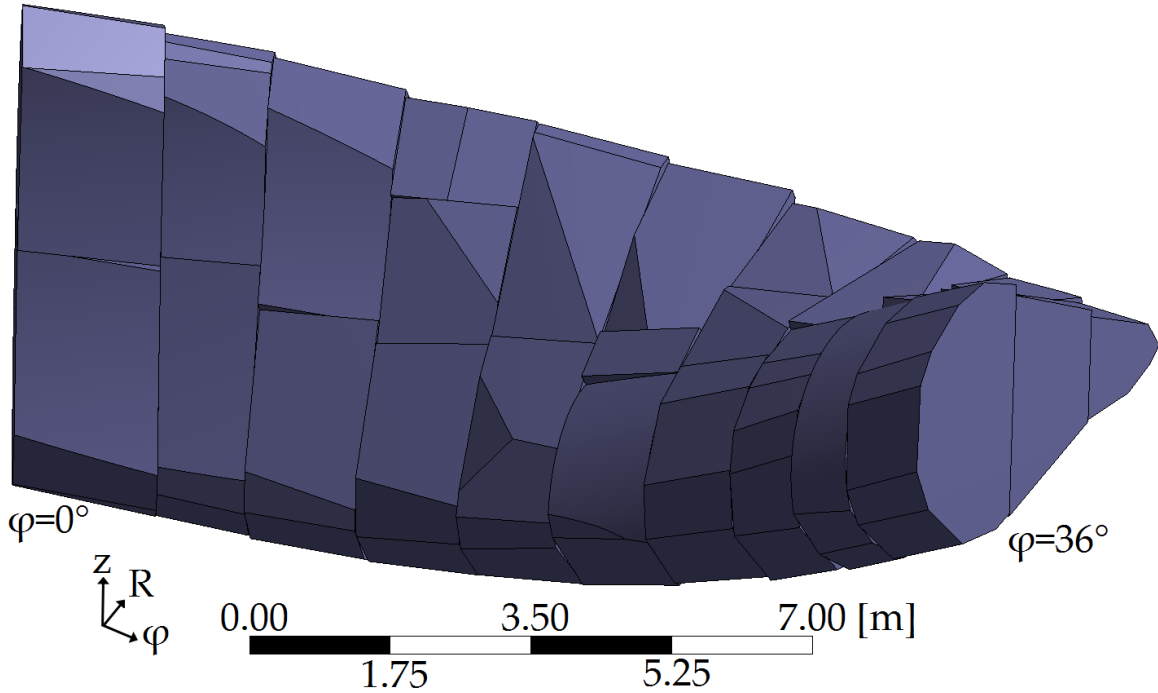


Figure 6.4: CAD model of the source cell, based on the LCFS as outer boundary layer, to represent the source volume for the ADVANTG calculation.

of  $5 \times 5 \times 5 \text{ cm}^3$  and a coarser resolution in the other areas. Both different meshes are defined in a way that the total number of mesh cells not exceeded  $10^6$  elements. Larger total mesh cells lead to a crash in ADVANTG. The area of interest, which need to be specified for the WW generation, is at the bean shape side inboard at  $R = 2245 \text{ cm}$  to  $R = 2142 \text{ cm}$ ,  $z = -30 \text{ cm}$ , and  $\varphi = 5^\circ$ . This area has a thickness of  $103 \text{ cm}$  and a neutron wall load of about  $1.35 \text{ MW m}^{-2}$ . This area has a reduced thickness compared to the outboard side and the calculation of the shielding performance in such an area is very important for improving the reactor design developments. The different meshes including the area of interest are shown in figure 6.5 and figure 6.6. The area of interest (blue) covers the complete area where the tally for the shielding calculations is located. The tally has a resolution of  $10 \times 10 \times 1 \text{ cm}^3$ , where the  $1 \text{ cm}$  step is in radial outward direction from plasma to the vacuum vessel outside. The tally used here to check the generated WW detects neutron and photon heating to achieve a detailed resolution of the nuclear heating in dependence of the radial distance. The foreseen final position of the tally has been obtained inside the envelope CAD model, because the coordinate difference for the tally transformation card could be measured inside the CAD model. Therefore, a box surrounding the tally position has been created in the CAD model, and the MCNP plane definition for each side of the box is generated.

This MCNP box definition has been used in a small MCNP input, containing only the box, a surrounding sphere to define the graveyard region, and the transformed and rotated mesh tally. The result of the test is that the transformed tally inside the box is exactly at the position where it is expected.

All heating calculations are performed with the WW's generated by ADVANTG, applied to HELIAS. The runtime criteria of all calculations is set to  $5 \times 10^6$  starting particles, only the WW changes from calculation to calculation. The tally applied here is only investigated by its relative statistical error to evaluate which of the generated WW is best suited for the shielding calculations. It is important to use coupled neutron photon transport, because the secondary photons, generated by neutron interaction with matter, have a large impact on the nuclear heating. Therefore, the influence of a WW, which is only optimised for neutrons during its generation, and a WW, which is optimised for neutrons and photons, must be investigated. The coupled neutron photon transport for a WW, optimised for both particles, decreases the calculation speed. Other than that the coupled neutron photon transport, with a neutron only WW, generate the responses of interest slightly faster. A heating calculation with the described boundary conditions is performed without using a WW to see how much impact the application of VR methods have on the calculation.

The WW's generated with the envelope geometry is investigated at first. Herein, both different source definitions and WW mesh sizes are used to generate the WW in ADVANTG. The particle transport optimisation in ADVANTG is focused on neutron transport only, except for the case using the volumetric source cell with non-uniform WW mesh definition. The names used to present the results are self-explaining in the sense that 'lcfs non-uni np' is a WW generated with the source cell using the LCFS as boundary, the non-uniform WW mesh size and coupled neutron photon transport during its creation. Results of the relative statistical error of the neutron and photon heating can be seen in figure 6.7.

The great impact of applying the mesh based VR method to the calculations can be seen in figure 6.7. The two different WW mesh sizes and the two different fixed sources have a huge influence on the generated WW and its herewith calculated relative statistical errors. The uniform WW mesh is too coarse in the area of interest, which disqualifies this mesh for further investigations. Additionally, the line source is not representing the plasma source well enough during the generation of the WW, which leads to a higher relative statistical error in the heating calculations. Both, the line source and the uniform WW mesh, are not considered for further calculations.

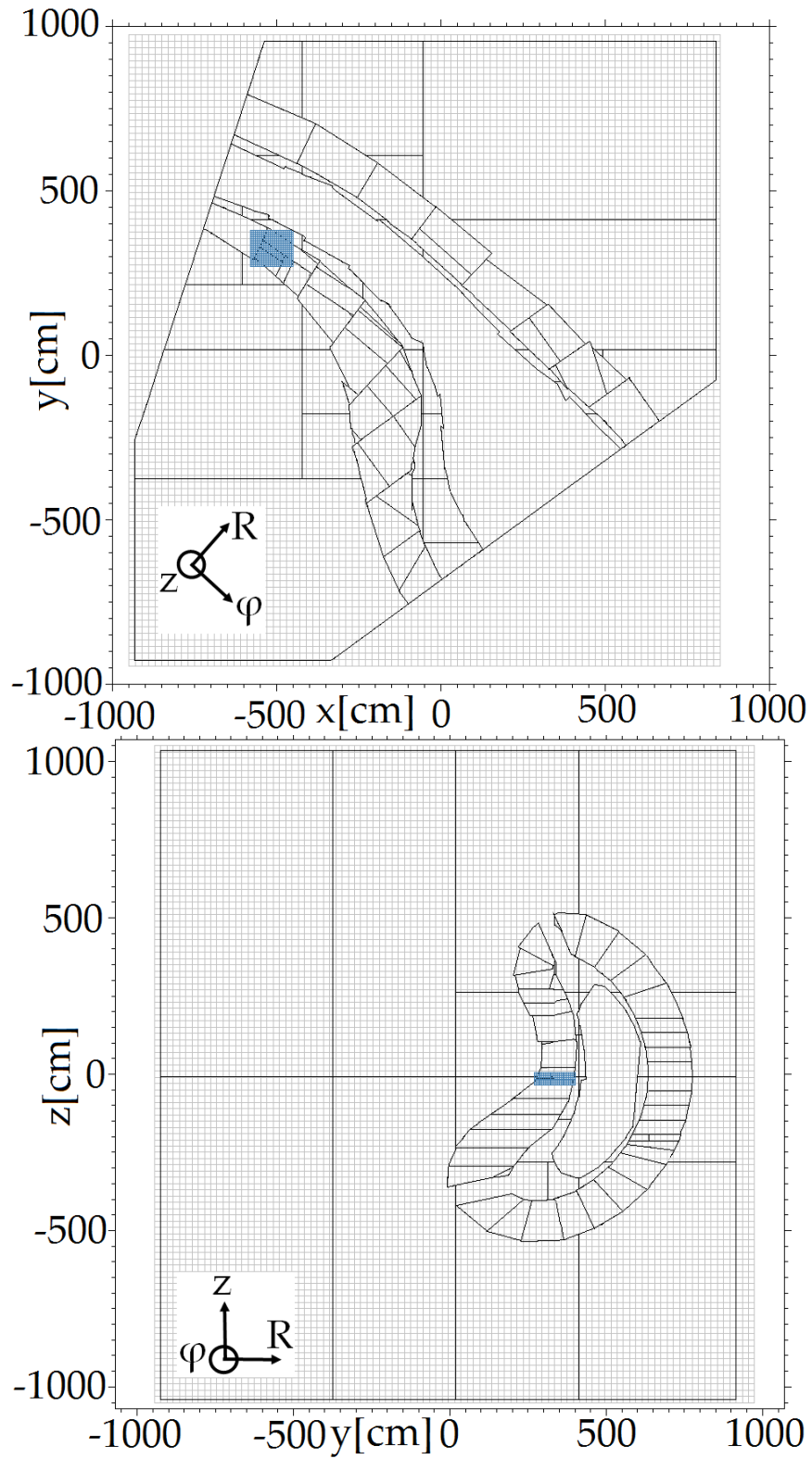


Figure 6.5: Uniform weight window in light grey covering the whole calculation geometry, including area of interest (blue square). On the top: XY-plane,  $z = 0$  cm and on the bottom: YZ-plane,  $x = -550$  cm. The axis scaling represents a scale and provides the point for the cutting plane, but does not refer to real geometry coordinates.



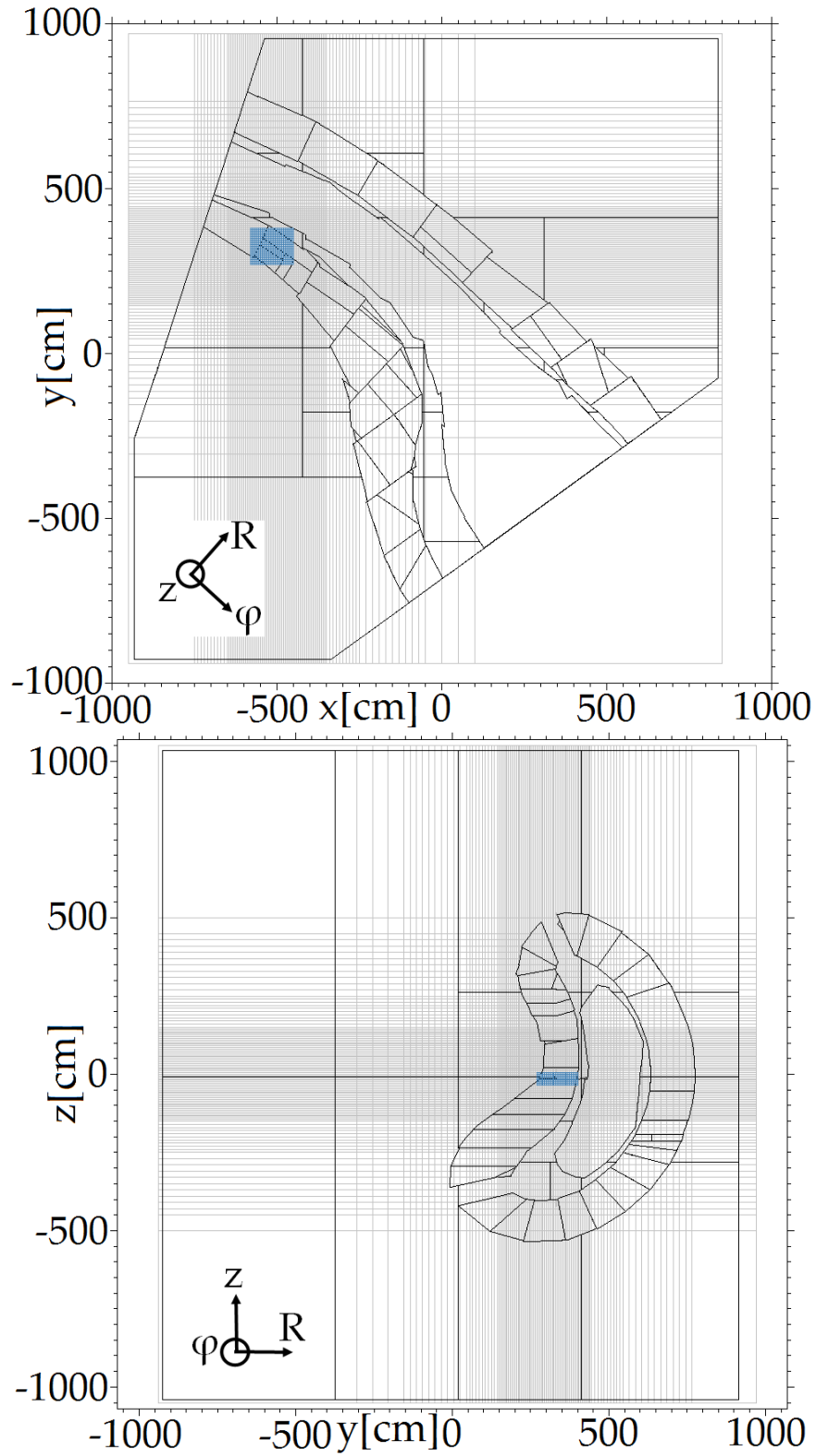


Figure 6.6: Refined weight window in light grey with a non-uniform resolution in the area of interest (blue square) covering the whole calculation geometry. On the top: XY-plane,  $z = 0$  cm and on the bottom: YZ-plane,  $x = -550$  cm. The axis scaling represents a scale and provides the point for the cutting plane, but does not refer to real geometry coordinates.

An investigation in figure 6.7 is, that the use of the coupled neutron photon transport optimisation during the WW generation has a significant impact on the relative statistical error of the photon heating. The photons, created as secondary particles via interaction of the neutrons with matter, must be tracked because they have a significant impact on the nuclear heating. If the optimisation for photons during WW creation is switched off, the created photons donate all their energy at the point of creation and are not tracked through the geometry. If the optimisation for photons is switched on, the photons are tracked from their creation place up to its death, e.g. via inelastic scattering. This leads to photons from outside the area of interest in the ADVANTG WW generation being tracked, if they are created or scattered inside the area of interest. The coupled neutron-photon tracking in the WW generation provides a realistic representation of the secondary particles in the weight windows.

The results generated with the envelope geometry in the ADVANTG WW generation needs to be proven with the extended geometry. Hereby, the scenario only using the source cell volume using the LCFS as boundary layer is investigated, once with neutron optimisation only and then with coupled neutron-photon optimisation. Results can be seen in figure 6.8, in comparison to the non-VR case and to one case which uses the envelope geometry.

Figure 6.8 shows that the graphs of the relative statistical error for neutrons nearly match in all VR cases. The graphs of the relative statistical error for photons show that only the photon optimised WW's are useful. Nevertheless, there is a geometrical influence of the envelope and extended geometry seen and the difference between the cases with coupled neutron photon optimisation during WW creation is by a factor of around 2 – 3 in the area of the VV shield and VV outside layer.

All the results for the application of the WW method for the stellarator show a significant improvement of the relative statistical error compared to a non-VR case. The case 'LCFS source, refined WW, extended WW generation geometry and coupled neutron-photon optimisation' shows very good results in improvement of the relative statistical error and in respect to its computational time. This WW is further used for the shielding calculation in respect to the non-planar shaped field coils at the outside of the VV.

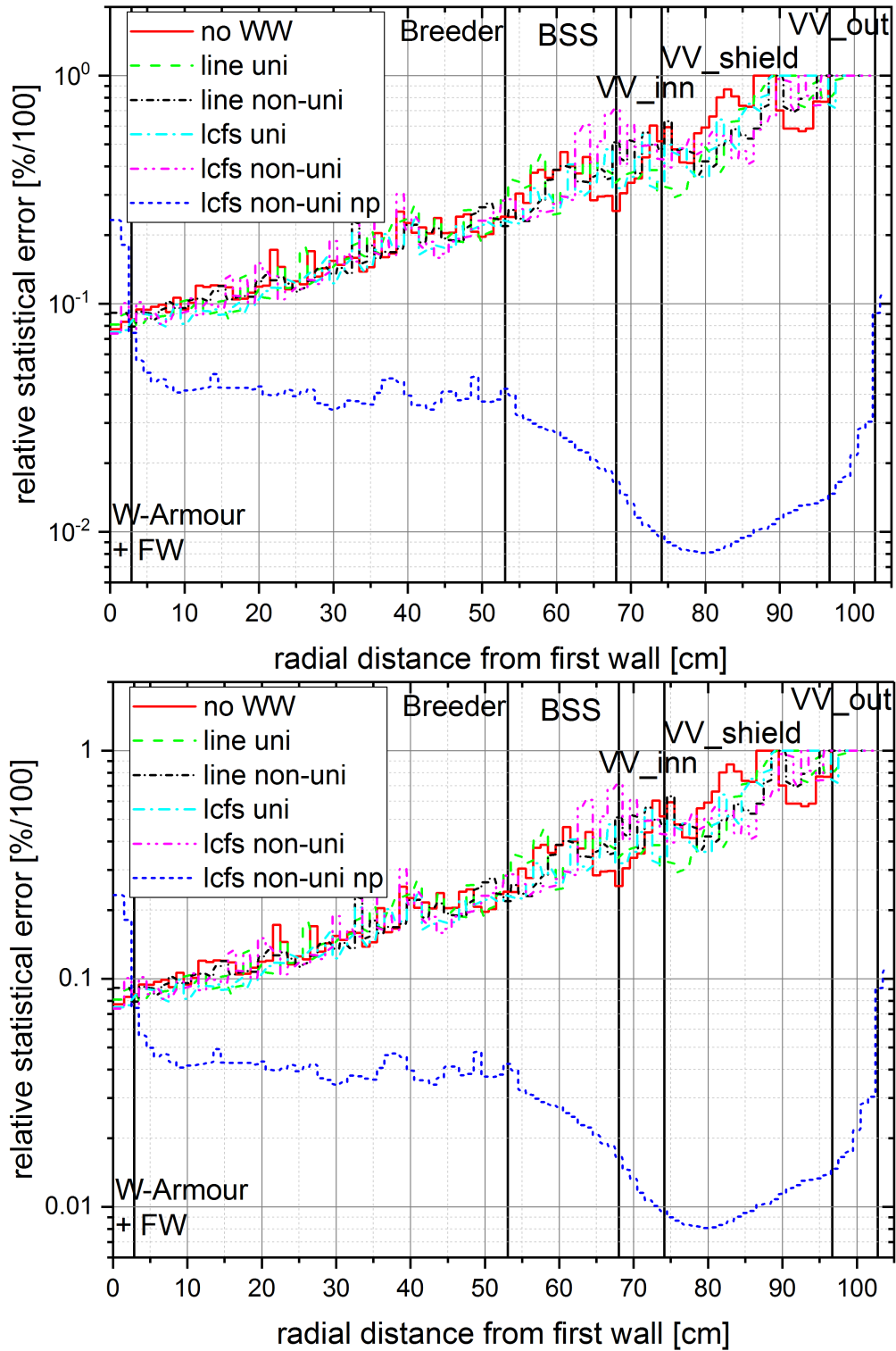


Figure 6.7: Calculated relative statistical error for neutrons (top) and photons (bottom) of the heating calculation as a function of the radial distance from the first wall [cm] with  $5 \times 10^6$  particles for different computational approaches while using the envelope model for the weight window generation. The abbreviations in the legend mean: ‘no WW’ = no weight window used; ‘line’ = line source; ‘lcfs’ = volumetric cell source with the LCFS as boundary; ‘uni’ = uniform weight window mesh; ‘non-uni’ = refined weight window mesh; ‘np’ = coupled neutron-photon WW optimisation.

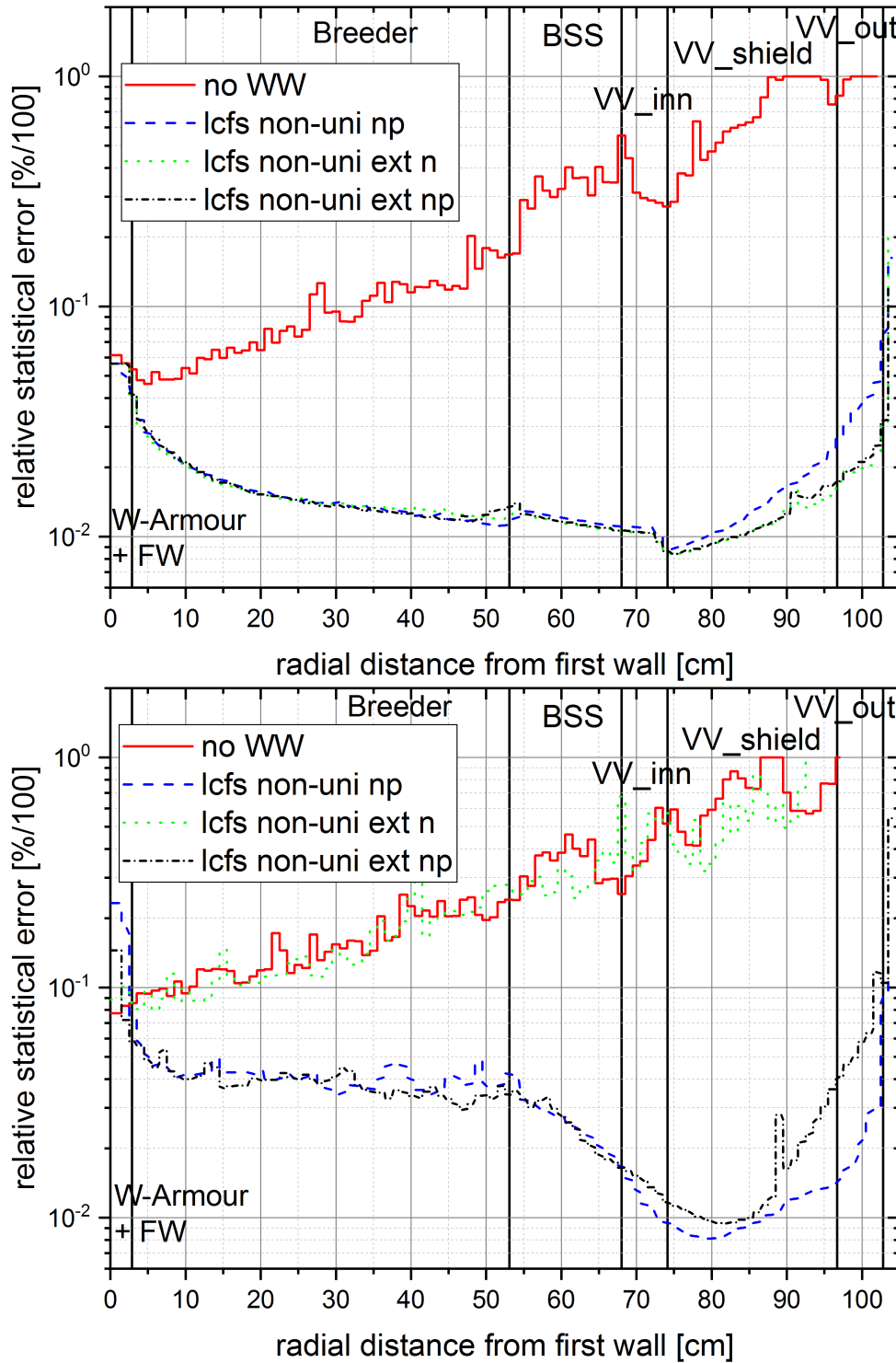


Figure 6.8: Calculated relative statistical error for neutrons (top) and photons (bottom) of the heating calculation as a function of the radial distance from the first wall [cm] with  $5 \times 10^6$  particles for different computational approaches while using the envelope model and the extended model for the weight window generation. The abbreviations in the legend mean: ‘no WW’ = no weight window applied; ‘lcfs’ = volumetric cell source with the LCFS as boundary; ‘non-uni’ = refined weight window mesh; ‘np’ = coupled neutron-photon WW optimisation; ‘ext’ = extended geometry model in WW generation.

## 6.4 Summary of variance reduction methods for HELIAS

A significant difference in the relative statistical error between the non-VR and VR cases is obtained. Thus the use of VR methods for calculations in areas far away from the fusion plasma is necessary to perform a reliable shielding analysis to protect the superconducting magnetic field coils. Two different VR methods are investigated, the cell based importance sampling and the superimposed weight window mesh.

The cell based importance sampling shows very good improvements of the relative statistical error for the CAD verification geometry. Nevertheless, the method could not be applied to the HELIAS model because of the geometrical complexity. Additionally, the method, including CAD geometry adaption, must be applied to the whole geometry and not only in a specific region which might be important for a neutronic analysis. Hence, this method is not suitable for productive runs of HELIAS.

The superimposed weight window mesh method overcomes these problems and allows the specification of the mesh resolution according to the calculation problem. Two different weight window mesh resolutions, a uniform mesh covering the whole geometry and a refined mesh with a higher resolution in the area of interest, are investigated. The WW is generated using ADVANTG, which requires a dedicated CSG geometry and an MCNP fixed source. The coupled neutron-photon optimisation during the WW generation ensures that secondary particles, eg. photons created through scattering events, are taken into account. To this end, a mesh based WW is generated which shows a significant improvement of the relative statistical error compared to the non-VR calculation, and the generated WW can be applied in shielding calculations for HELIAS.

# Chapter 7

## Nuclear Responses for a generic HELIAS reactor design

The nuclear analysis of the HELIAS stellarator is the main target of the present work. This comprises the Neutron Wall Loading (NWL), Tritium Breeding Ratio (TBR), neutron flux distribution, and a shielding analysis of the facility, see also [Hä18a],[Hä18b] and [Hä19].

### 7.1 Neutron Wall Loading (NWL)

The Neutron Wall Loading (NWL) is an important characteristic for the nuclear analysis of the fusion reactor. It denotes the fusion power loaded on the first wall due to neutron irradiation calculated per unit area and it represents the neutron current carried through the plasma facing surfaces of the plasma chamber. This feature takes into account the fusion power, the spatial distribution of the source neutrons and the reactor geometry.

The special normalisation of the MCNP tally is applied in this case to account for the plasma neutron source intensity [Fis18]:

$$N_{fus} = \frac{P_{fus}}{E_{fus}} = 1.065\ 22 \times 10^{21} \text{ s}^{-1}, \quad (7.1)$$

where  $N_{fus}$  is the neutron source intensity in  $\text{s}^{-1}$ ,  $P_{fus} = 3000 \text{ MW}$  is the reactor fusion power, and the total energy released per one fusion reaction  $E_{fus} = 17.58 \text{ MeV}$ . It must be noted that the HELIAS reactor model discussed in this work corresponds to one tenth of the full reactor resulting in  $N_{fus} = 1.065\ 22 \times 10^{20} \text{ s}^{-1}$ .

A simple assessment of the average NWL can be made by making use of the neu-

tron plasma source intensity and the total area of the plasma facing surfaces. This assumption is not correct for the MCNP simulation, because in the computational model openings for the divertors are present. The simple NWL can be calculated by:

$$\text{NWL}_{\text{simple}} = \frac{P_{\text{fus}} \cdot E_{\text{neutron}}}{E_{\text{fus}} \cdot A_{\text{surfacearea}} \cdot 10} = 0.971 \text{ MW m}^{-2}, \quad (7.2)$$

where  $P_{\text{fus}} = 3000 \text{ MW}$ ,  $E_{\text{neutron}} = 14.08 \text{ MeV}$  is the neutron energy per one fusion reaction,  $E_{\text{fus}} = 17.58 \text{ MeV}$  and  $A_{\text{surfacearea}} = 247.7 \text{ m}^2$  is the total area of the plasma facing surface. The factor 10 in the denominator takes into account that only one tenth of the HELIAS reactor geometry is investigated here.

### 7.1.1 Procedure for NWL assessment

The NWL is calculated only on the plasma facing surface of the blanket because of a missing divertor geometry for HELIAS. In the divertor regions are only openings. Only the tungsten layer, which protects the first wall, is used for this calculation and the neutrons are killed after crossing the plasma facing surface to estimate the energy only coming from the plasma and avoiding double counting. The first geometry layout for mapping the NWL is given in figure 7.1. The eight rings are split into smaller rings with the indexing from ring 1-1, which is the bean shape side  $\varphi = 0^\circ$ , to ring 8-5, which is the triangular shape side  $\varphi = 36^\circ$ , with an average ring dimension of  $1^\circ$  or less in some rings. The shape evolution of the stellarator can be seen in figure 7.2 for the closed rings from ring 1-1 to ring 8-5. In the rings 1 to 4 are openings for the upper and lower divertor visible. The current HELIAS design does not include a model for the divertor design, and only indicates the area, where a divertor is foreseen, with these openings.

The NWL is calculated in MCNP using the \*F1 tally to obtain the surface current with the unit of MeV [MCN03]. All plasma facing surfaces, in total 1845, are assigned in the tally including their corresponding surface area to finally provide the results in the unit  $\text{MeV m}^{-2}$ . The quantity  $N_{\text{fus}}$  is used to normalise the tally result to the plasma neutron source intensity.

### 7.1.2 Computational Results

The DAGMC calculation has been performed with a total of  $10^9$  source particles, without lost particles detected, to obtain results with a relative statistical error lower than 0.7%. The highest relative statistical error has been determined in the areas

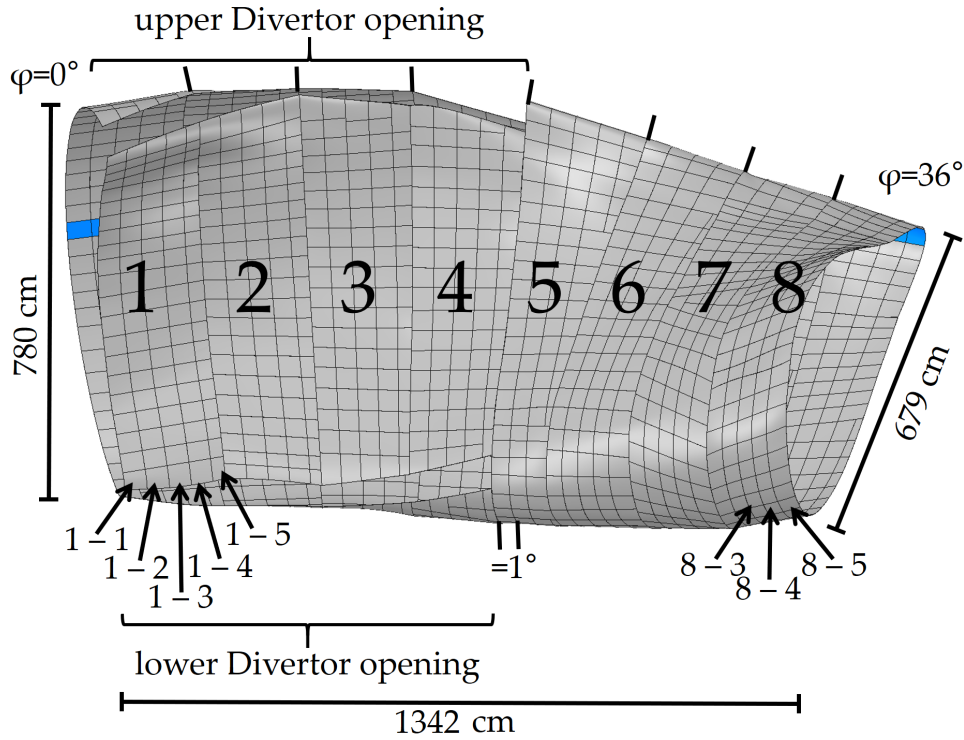


Figure 7.1: Assignment of the stellarator geometry for the NWL calculation including the eight large geometry segments and their separation into smaller rings.

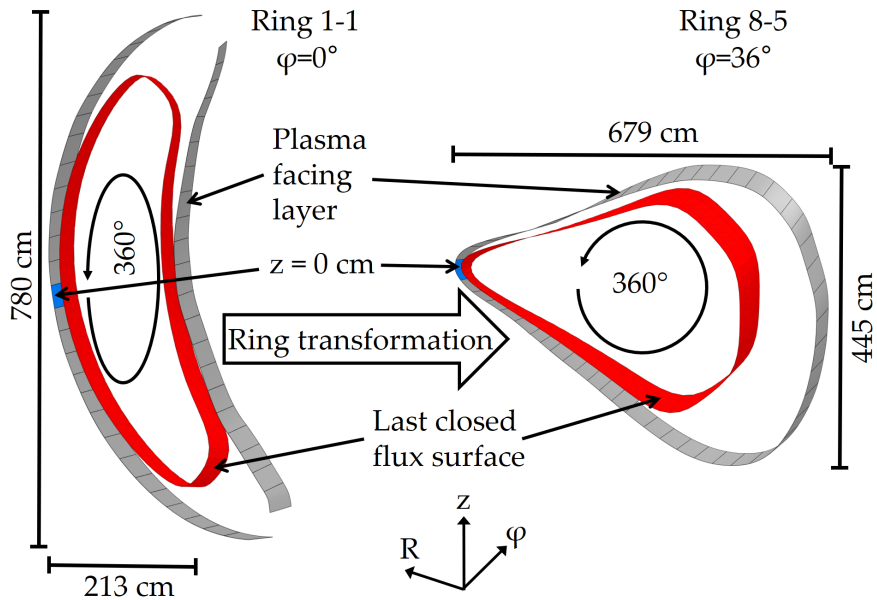


Figure 7.2: Ring transformation from the bean shape ( $\varphi = 0^\circ$ ) to the triangular shape ( $\varphi = 36^\circ$ ) side including a blue mark for the  $z = 0$  cm midplane position at the outboard side.

around the divertor openings, as these areas are the furthest away from the fusion plasma.

To verify the calculation, a second calculation with a different approach from IPP



Greifswald has been performed. The IPP approach utilises the in-house developed plasma physics MC code ‘nflux’ based on the ray tracing technique for the collision-free propagation of the source neutrons emitted from the plasma [Hä18b]. Both approaches use the same plasma distribution for the source description and the same plasma facing surface. The geometry preparation is different in both approaches, as the DAGMC geometry uses a faceted volumetric geometry which is separated into 1845 tiles, and nflux uses a surface mesh with 3800 triangles with different surface areas, interpolated on a  $60 \times 60$  grid. Hence, the results of the ‘nflux’ calculation have a higher resolution compared to the DAGMC calculation. Results for the DAGMC calculation can be seen in figure 7.3 and for the IPP approach with ‘nflux’ in figure 7.4.

The following approach has been applied for the presentation of the calculated results for the stellarator geometry. The NWL results are mapped over a 2D plot with a toroidal angle from  $\varphi = 0^\circ$  to  $\varphi = 36^\circ$ , presented in the figure 7.1. The poloidal coordinate starts at the reactor mid plane outboard side at  $z = 0$  cm, which corresponds to a poloidal angle of  $0^\circ$ , and passes counterclockwise through lower divertor towards inboard side and the upper divertor, back to mid plane outboard side. The divertor openings are indicated in the figure 7.1 as black lines between  $\varphi = 0^\circ$  and  $\varphi = 18^\circ$ . A visual comparison of figure 7.3 and 7.4 shows an agreement of the NWL in spatial distribution and intensity with deviations in some areas. The deviations are due to the different geometry preparation, and the different calculation approaches. Both figures show that the locations with highest NWL are meandering over the whole blanket surface, with an overall maximum at around  $8^\circ$  toroidal and  $26^\circ$  poloidal direction, corresponding to the position  $R = 2448$  cm,  $\varphi = 8^\circ$ , and  $z = -69$  cm in the HELIAS geometry. The location is at the outboard mid plane close to the bean shape side. The distribution of the NWL with the meandering location of the highest NWL is due to the distance between the plasma and the tungsten armour, and due to the neutron emission probability inside the plasma. In areas with less distance from the plasma to the tungsten armour, in combination with higher neutron emission probabilities, are higher NWL obtained.

The results in figure 7.3 and 7.4 show a spread of the NWL between  $\sim 0.06 \text{ MW m}^{-2}$  and  $\sim 1.96 \text{ MW m}^{-2}$ . This means, that the heat load from the plasma to the breeding blanket is unevenly distributed, which must be taken into account in the development of an engineering design of the stellarator breeding blanket. The breeding blanket in the area with a high NWL require a higher coolant flow to ensure the material integrity. Due to the large NWL spread, a difference in the radiation induced material degradation can be expected, which requires a very careful selection of the applied

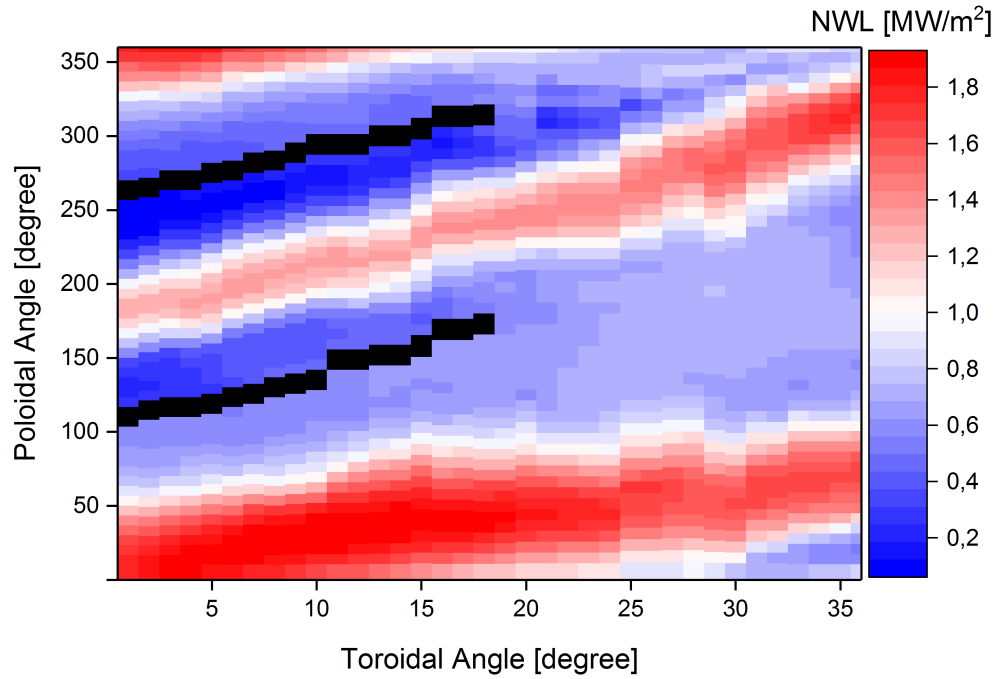


Figure 7.3: Poloidal-Toroidal neutron wall loading distribution calculated with DAGMC. The divertor openings are presented as black line and located from  $\varphi = 0^\circ$  to  $\varphi = 18^\circ$ .

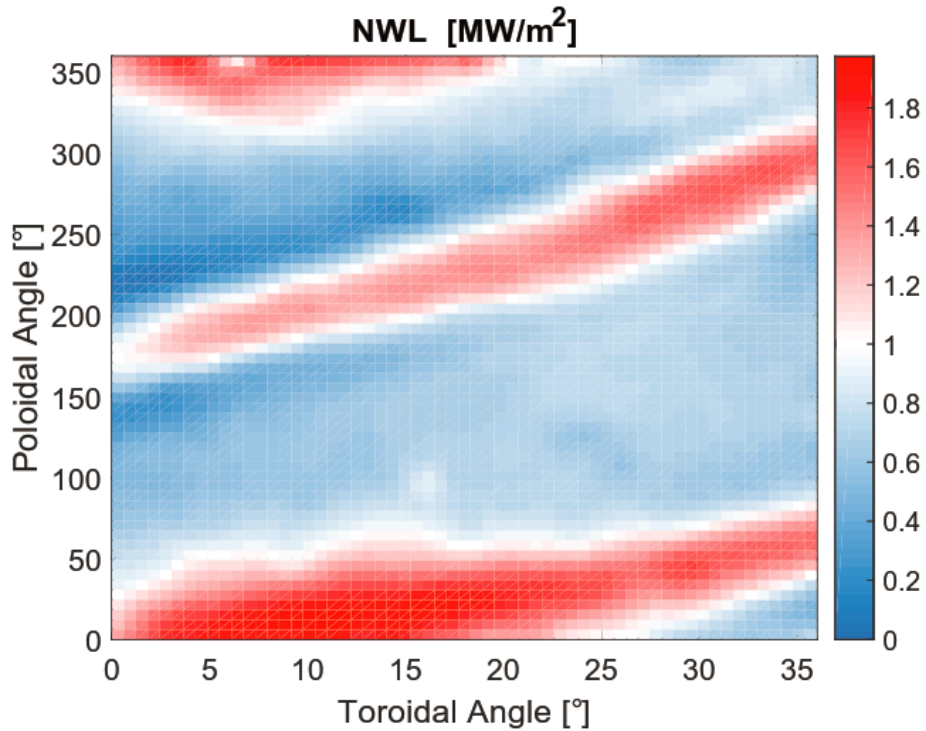


Figure 7.4: Poloidal-Toroidal neutron wall loading distribution provided by the plasma physics simulation with 'nflux' of IPP Greifswald [Hä18b].

materials to withstand the heat load and the radiation damage, and at the same time to provide a sufficient tritium breeding ratio, heat removal and radiation shielding in respect to the non-planar shaped magnetic field coils.

The ‘nflux’ result has been interpolated at IPP Greifswald with the ‘nearest-neighbour’ interpolation method on the geometry used for the DAGMC calculation, which introduces uncertainties to the ‘nflux’ result. The difference between the ‘nflux’ interpolation and the DAGMC approach is obtained and presented in figure 7.5. A total deviation of 4.61% with a maximum deviation of 45.4% at position 5° toroidal / 105° poloidal is obtained between both results. The deviations at the bean (0° toroidal) and triangular (36° toroidal) shape side are due to the missing of reflecting boundary conditions in the ‘nflux’ calculation. The differences at position 10° – 15° toroidal and 350° poloidal are caused by degenerated triangles in the ‘nflux’ calculation. The deviations at the upper divertor opening from 0° – 18° toroidal and 250° – 280° poloidal are noticeable and caused by the interpolation method. Additionally, some fragments, like position 27° toroidal / 340° poloidal, are obtained which are due to the ‘nflux’ mesh uncertainty.

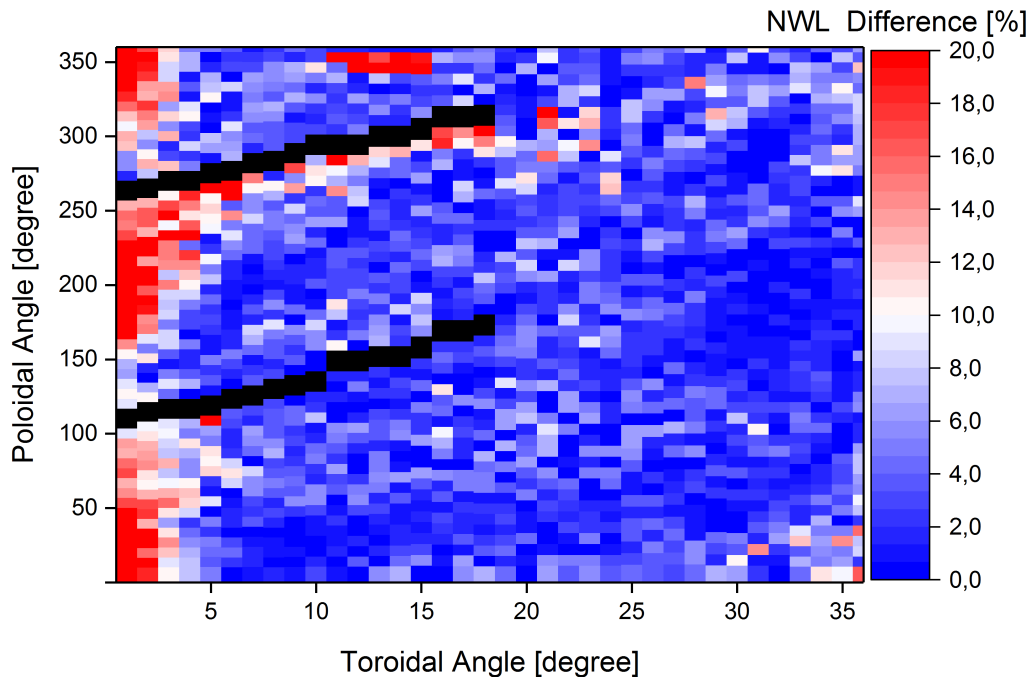


Figure 7.5: Difference of the Poloidal-Toroidal neutron wall loading distribution between the DAGMC and ‘nflux’ approach. A few obtained NWL differences are above 20% in red colour.

The numerical results are given in table 7.1. The results show an agreement within the statistical uncertainties between the two approaches. The calculated average NWL, presented in table 7.1, deviates from the NWL obtained using the simplified approach

previously discussed. This is due to the assumption of a fully closed surface without the opening of the divertor region in the simplified calculation. The agreement of the results obtained with DAGMC and ‘nflux’ is within 3% in the average NWL. This provides confidence that the modelling of the plasma neutron source applied in this work is done in a correct way.

Table 7.1: Comparison of the NWL results generated with two different approaches.

|                                    | KIT<br>(DAGMC)         | IPP<br>(nflux)   |
|------------------------------------|------------------------|--|
| Maximum NWL [ $\text{MW m}^{-2}$ ] | 1.936                  | 1.958  |
| Average NWL [ $\text{MW m}^{-2}$ ] | 0.953                  | 0.926  |
| Statistical Error                  | < 0.7% at each surface | < 0.5% at each surface                                   |
| Geometry Resolution                | 1845 tiles             | 3800 triangles, interpolated<br>on a $60 \times 60$ grid |

The change of the NWL profiles obtained for different toroidal positions is shown in figure 7.6. Each plot represents the the NWL along a specific toroidal angle which corresponds to the ring number. The selection of the rings is to represent the change and the position of the maximum NWL in the different angles. For comparison, the NWL of ring 1-1,  $\varphi = 0^\circ$ , is displayed in dashed light blue colour in each plot of figure 7.6. It can be seen that the poloidal position vary of the two maxima over the ring location and that it is different at each toroidal position. The first three plots contain identification marks for the divertor, which are present in the toroidal angle from  $\varphi = 0^\circ$  to  $\varphi = 18^\circ$ .

The results of HELIAS show a very high maximum NWL of  $1.936 \text{ MW m}^{-2}$ . In comparison, the NWL results of the EU DEMO tokamak, calculated with the 2016 HCPB design [Her17], show a maximum NWL at the inboard side of  $1.08 \text{ MW m}^{-2}$  and at the outboard side of  $1.34 \text{ MW m}^{-2}$ , with an average NWL of  $\sim 1.0 \text{ MW m}^{-2}$  [Per17]. It must be noted that DEMO reactor is investigated with a fusion power of  $2037 \text{ MW}$  [Per17], which is  $\sim 1000 \text{ MW}$  less compared to HELIAS. The material in the plasma facing surface is exposed to the neutron load, and to the heat load from the fusion plasma. The thermal power of the EU DEMO baseline design with a fusion power of  $2796.4 \text{ MW}$  assumes a homogeneous first wall heat flux of  $0.5 \text{ MW m}^{-2}$  [Her17]. The maximum NWL of DEMO, also taking the heat load into account, is already at the design limits of the HCPB breeding blanket in sense of the first wall cooling with high pressure helium of  $8 \text{ MPa}$  [Her17]. This means for HELIAS, that an adapted cooling concept must be developed. Different approaches need to be considered, like

the adjustment of the coolant flow and an improved cooling scheme in the breeding blanket and first wall, presented in [Her19], or the usage of CO<sub>2</sub> as cooling gas, proposed in [Wan19]. All these possibilities have drawbacks and must be investigated in detail in further HELIAS design optimisations.

The structural material in a fusion reactor expands under heat load. Expansion gaps must be introduced between the breeding blanket segments to overcome this problem. At the same time, these gaps must be constructed in a way to avoid neutron streaming to the vacuum vessel.

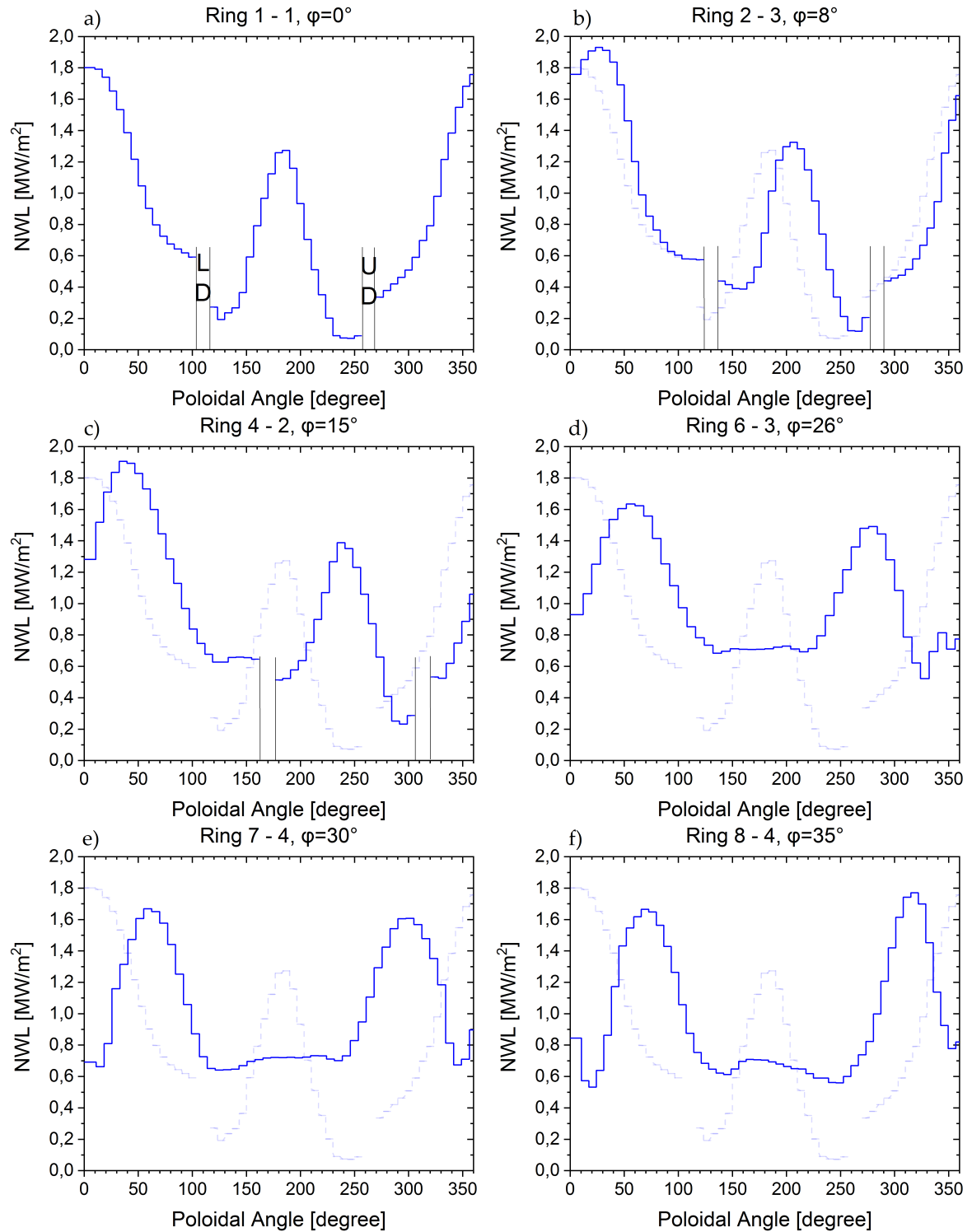


Figure 7.6: Calculated NWL as a function of the poloidal angle  $\phi$  for the HELIAS reactor at nominal conditions at different ring segments  $\phi$ . The light blue dashed lines denote the distribution of the reference segment at  $\phi = 0^\circ$  (ring 1-1). The indication in figure (a) means LD = lower divertor and UD = upper divertor, and corresponds to the indicated divertor openings in figure (b) and (c).

## 7.2 Neutron Flux Distribution

The neutron flux is one of the most important nuclear responses that provides a possibility to justify the efficiency of the engineering solutions used in the reactor design. This means that the neutron flux distribution can be used to detect neutron streaming, evaluate the shielding capability and generate the input for activation calculations. The neutron flux map superimposed over the reactor geometry enables the indication of the hot spots, which are regions with high neutron flux, as well as the weak points, e.g. gaps in the geometry could lead to neutron streaming, in the reactor design. Possible solutions to overcome these problems can be found by using the neutron flux map.

A mesh tally has been utilised providing a Cartesian mesh with a resolution of  $3 \times 3 \times 3 \text{ cm}^3$  for a detailed mapping of the 3D neutron flux distribution over the reactor geometry. This tally contain in total more than  $10^8$  mesh elements and a division into four equal segments is necessary to avoid an overload of the computer memory. The final result has been obtained by their combination, including the further normalisation of the MCNP results with the plasma source neutron intensity  $N_{fus}$ .

The results shown in figure 7.7 on the top a vertical cut of the 3D neutron flux distribution in the bean shape side at toroidal position  $\varphi = 3^\circ$  including the reactor geometry, and on the bottom its corresponding statistical uncertainty. The attenuation of the neutron flux is found with a factor higher than 15 between the flux inside the plasma and at the vacuum vessel outer layer. The attenuation is due to the interaction of the neutrons with the reactor materials, e.g. elastic and inelastic scattering, and neutron capture. The highest neutron flux from the plasma in direction to the reactor components is at the mid plane area at  $z = -200 \text{ cm}$  to  $z = 150 \text{ cm}$ . This corresponds to the neutron emission probability inside the fusion plasma, and also to the distance between fusion plasma and the surrounding components, which is small in this area. Such an area has a high NWL, which translates into a high heat load inside the breeding blanket, and a higher radiation damage. The materials applied for the breeding blankets in such areas must be selected carefully to withstand these conditions.

The results in figure 7.7 show significant neutron leakages through the divertor openings in poloidal direction  $\phi = 113^\circ$  to  $\phi = 120^\circ$  and  $\phi = 266^\circ$  to  $\phi = 273^\circ$ , because no material is specified in this region. The neutron flux is higher with a lower statistical error in the material close to the divertor area because of the missing material. These results do not correspond to the results obtained in the other parts of the reactor.

The statistical uncertainty can reach up to 100 % in the regions outside the plasma,

which is not acceptable. This indicates the importance of applying variance reduction techniques to get the nuclear responses of interest in those regions with acceptable statistical uncertainty. The neutron flux results for the tungsten armour, first wall and most parts of the breeding blanket layer have statistical errors below 10% with an increasing statistical error in areas further away from the fusion plasma.

The results for the neutron flux support the investigations of the NWL. It is important for the engineering design of the reactor components, that high neutron fluxes, high heat loads and the expected higher radiation damage are taken into account.



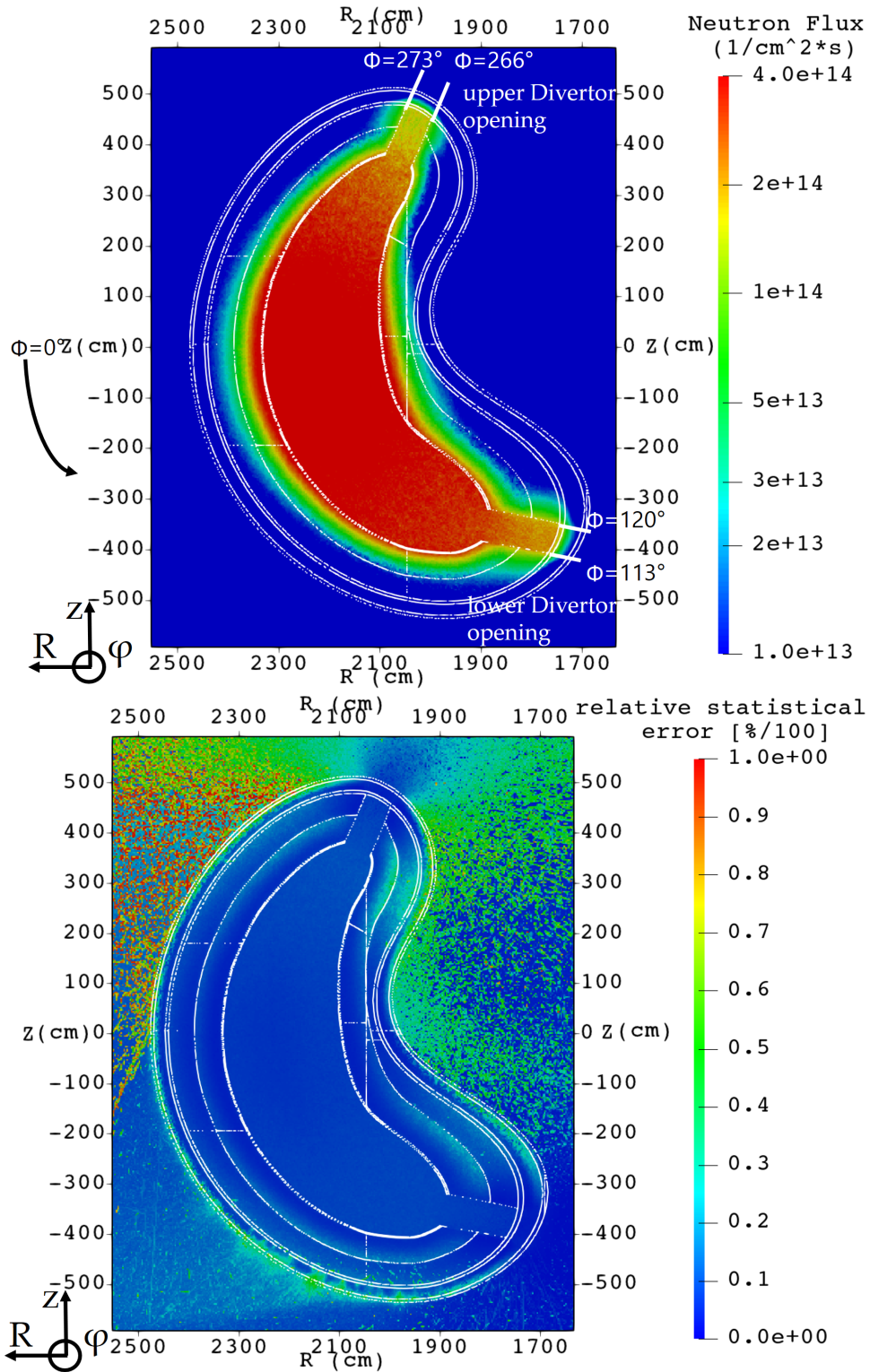


Figure 7.7: Neutron flux distribution with associated HELIAS geometry (top) and corresponding relative statistical error (bottom), calculated in the position  $\varphi = 2^\circ$  without applying variance reduction methods.

## 7.3 Tritium Breeding Ratio (TBR)

The TBR is calculated in MCNP making use of the standard F4 tally and a multiplication factor. The MCNP tally multiplication operator requires a standard nuclear reaction identifier to force MCNP to collapse neutron spectrum in the specific geometry cell with the cross-section. This results in the TBR value in units of atoms/per source neutron. The tritium generation obtained in  ${}^6\text{Li}$ ,  ${}^7\text{Li}$  and  ${}^9\text{Be}$  is then added together resulting in the reactor TBR. The breeding layer, containing a homogenised HCPB material mixture, is shown at the bean shape side in yellow colour in figure 7.8.

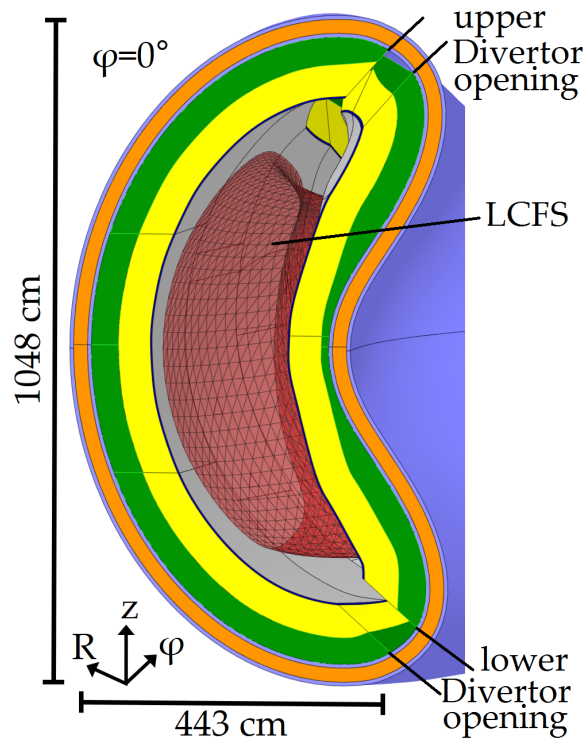


Figure 7.8: Sketch of the bean shape side  $\varphi = 0^\circ$  of HELIAS including the last closed flux surface and the material layers, corresponding to table 3.1. The TBR is obtained in the breeding blanket layer, presented in yellow colour.

A net TBR of  $\geq 1.0$  is required to ensure that one triton is available per D-T fusion reaction for the re-injection in the plasma. Nevertheless, some additional margins must be achieved to take Tritium losses (e.g. radioactive decay) and uncertainties (e.g. statistical errors, nuclear data, modelling errors) into account. This ends in a typical design target for the global TBR in a range of 1.05 – 1.15 [EG09], [Fis15], [Fis20]. Using the technique describe above, the tritium breeding ratio of the HELIAS reactor is estimated to  $\text{TBR} = 1.3863 \pm 0.0001$ . This high TBR value is due to the very idealistic assumption of a full coverage of the plasma facing surface with a breeding

layer filled with a homogenised material mixture, as well as the big radial thickness of 50 cm in the breeding zone applied in the model compared to the EU DEMO tokamak design [Her17]. This high TBR value can be seen for an early version of the 2016 HCPB design with  $TBR = 1.368$ . Furthermore, ports, antennas, diagnostics or the heating system are currently not taken into account in the HELIAS model that typically reduces the breeding zone volume, resulting in a reduced TBR value.

The high TBR value must be verified to proof its correctness. The verification geometry from chapter 4 is used for this purpose to generate TBR values with the HCPB mixture and all three investigated geometry translation approaches. The verification geometry contains a layered structure, like the HELIAS geometry, with a certain thickness of each material layer. However, the HELIAS geometry differs in the thickness of the back support structure layer and HELIAS contains divertor openings. This means that the verification geometry is an even more idealised model compared to the HELIAS model. The TBR values, calculated with the verification geometry, are presented in table 7.2. Only a marginal difference of the computed TBR values can be seen between the three geometry translation approaches. The difference of the TBR value of around 2.5 % between HELIAS and the verification geometry is caused by the different geometries and the divertor openings in HELIAS, which create a gap in the total poloidal angle of  $14^\circ$  and in the toroidal angle from  $\varphi = 0^\circ$  to  $\varphi = 18^\circ$ . Nevertheless, the performed calculations with the verification geometry indicates, that the TBR calculation for HELIAS is reliable.

Table 7.2: Results of the TBR calculations for the verification geometry.

|     | DAGMC              | UM                 | CSG                |
|-----|--------------------|--------------------|--------------------|
| TBR | $1.421 \pm 0.0001$ | $1.424 \pm 0.0001$ | $1.423 \pm 0.0001$ |

The large difference between TBR design target values, defined for the EU DEMO tokamak, and the obtained results give an indication that a HELIAS-type stellarator geometry has the principle capability to achieve tritium self-sufficiency. The TBR value decreases immediately when heterogeneous engineering models for the breeding blanket or the integration of ports, antennas, diagnostic and heating system are integrated in the reactor geometry. The results obtained can be used as a good starting point for further stellarator breeding blanket development.

## 7.4 Analyses of reactor shielding performance

The shielding performance of the HELIAS reactor is mandatory to demonstrate the stability of the superconductor in the non-planar field coils. The total material thickness of HELIAS differs in poloidal and toroidal direction, because the available space between the plasma and the vacuum vessel is not uniform. In the HELIAS model, the BSS is therefore integrated with a non-uniform thickness. This means that the identification of critical domains exceeding acceptable values with less total material thickness and relatively high neutron wall load is important. Such a critical area in HELIAS is shown in figure 7.9. The position is  $R = 2245$  cm to  $R = 2142$  cm,  $z = -30$  cm, and  $\varphi = 5^\circ$  at the inboard side with a total radial material thickness of  $\sim 103$  cm and a NWL of  $\sim 1.35$  MW m<sup>-2</sup>, shown in figure 7.10. The position with high NWL and less radial material thickness is challenging for the radiation shielding. A superimposed mesh tally FMESH4 is implemented in this location with a mesh element size of  $10 \times 10 \times 1$  cm<sup>3</sup>, where the 1 cm step is in radial outward direction from plasma to the vacuum vessel outside. The tally has been set-up for each calculation problem with different tally multiplication cards, or reaction numbers, to generate the nuclear responses. This context can be described in the equation:

$$ReactionRate = \int \varphi(E)\sigma(E)dE,$$

where  $\varphi(E)$  is the energy dependent neutron flux density and  $\sigma(E)$  is the energy dependent nuclear cross-section. The application of the VR method is needed to obtain reliable results, where the WW presented in section 6.3 is used in each calculation.

The assumption is that such a critical area cannot fulfil the shielding design requirements specified for the EU DEMO tokamak, with the current HELIAS design, to protect the superconducting magnetic field coils. The design requirements for the EU DEMO tokamak are defined in [Fis15] and extended with target values in [Bac18], which are taken into account during the discussion of the results for HELIAS. The values are presented in table 7.3, extended with a column to judge if the value is applicable to HELIAS. It must be taken into account that the breeding blanket design and the radiation scenario for HELIAS are not yet defined. The radiation damage requirement for the breeding blanket is based on experimental evaluated data, which must taken into account during the breeding blanket development for HELIAS and are applicable, if Eurofer is used as structural material. All other values can be taken into account because similar technologies, like superconducting field coils or materials, are applied for EU DEMO tokamak and HELIAS.

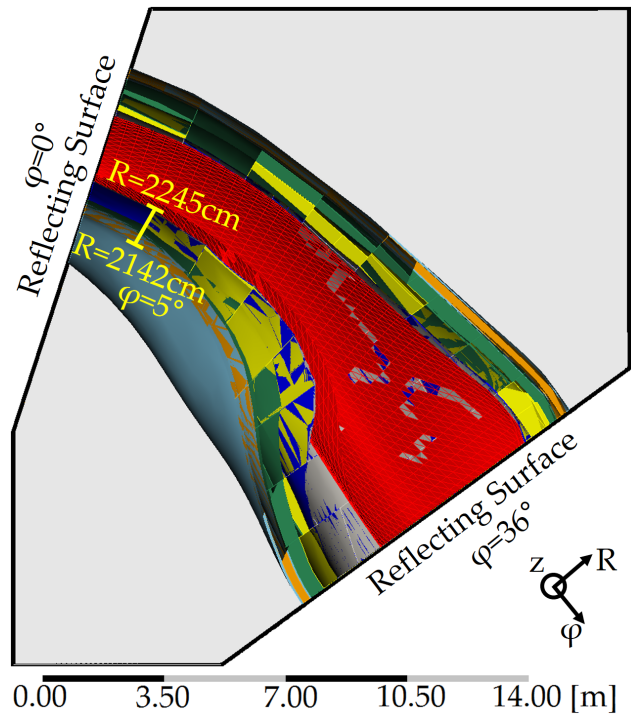


Figure 7.9: HELIAS cross-section at  $z = -30$  cm to present the tally location at  $R = 2245$  cm to  $R = 2142$  cm,  $z = -30$  cm, and  $\varphi = 5^\circ$ , highlighted with a yellow line, applied for the shielding calculations. The material colour coding refers to table 3.1.

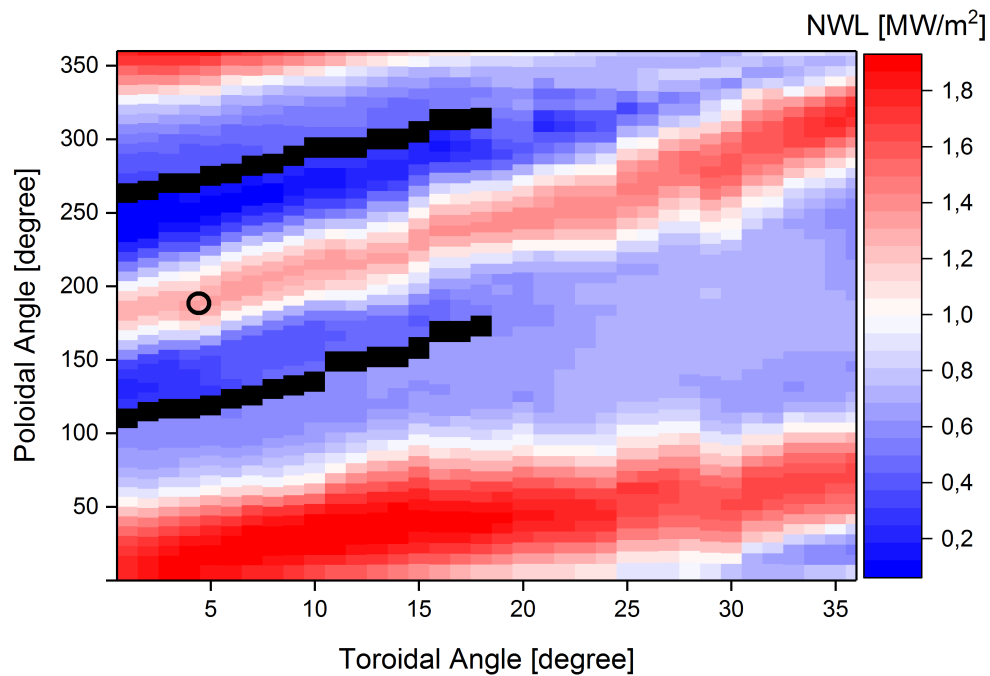


Figure 7.10: Visualisation of the shielding tally location in the NWL map as a function of the toroidal and poloidal angle. The location is highlighted in the black circle at  $\varphi = 5^\circ$  and  $\phi = 190^\circ$  with a NWL of  $1.35 \text{ MW m}^{-2}$ .

Table 7.3: Selected material damage limits, shielding requirements and design targets in EU DEMO tokamak, full table in [Bac18]. The applicability to HELIAS is indicated.

| COMPONENT/<br>LOCATION  | REQUIREMENT                            | LIMIT/<br>TARGET                        | APPLICABLE<br>TO HELIAS |
|---|--|---|-------------------------|
| Superconductors   | Displacement damage to epoxy insulator | $10^{22} \text{ m}^{-2}$                | yes                     |
|   | Nuclear heating in winding pack        | $50 \text{ W m}^{-3}$                   | yes                     |
| Starter blanket FW  | Displacement damage to Eurofer         | 20 dpa                                  | not fully               |
| 2nd blanket FW  |  | 50 dpa                                  | not fully               |
| Vacuum Vessel   | Displacement damage                    | 2.75 dpa                                | yes                     |
|   | Nuclear heating                        | $0.5 - 1 \text{ W cm}^{-3}$<br>(target) | yes                     |
| Cutting / re-welding location in In-Vessel<br>Component cooling pipes | Helium production                      | 1 appm<br>(target)                      | yes                     |

### 7.4.1 Neutron flux

First, the assessment of the neutron flux radial profile has been performed. The mesh tally registers the neutron flux with a separation into two different neutron energy groups, one for thermal neutrons with an energy of  $E_n \leq 0.1 \text{ MeV}$ , and one for fast neutrons with an energy of  $E_n > 0.1 \text{ MeV}$ . The results are shown in figure 7.11 including a target value for the neutron flux density of  $\phi \leq 1 \times 10^9 \text{ cm}^{-2} \text{ s}^{-1}$  which shall not be executed to ensure the integrity of the magnetic field coils due to irradiation damage. This value refers to a EU DEMO tokamak design target ‘If we consider the maximum fast neutron fluence to the copper stabiliser assuming a warming-up of the toroidal field coil after 5 full power year operation’ [Fis08]. The superconducting field coils are outside of the vacuum vessel and not included in the HELIAS computational model. Therefore, the value for the outside vacuum vessel layer is used as indicator for the comparison [Fis18] [Har12]. Nevertheless, the field coils consist of the coil casing, the winding pack and the insulator. The obtained results presents a conservative value of the neutron flux, but more detailed calculations including the superconducting field coils are necessary.

The radial distribution of the neutron flux in figure 7.11 shows in the tally results a relative statistical error below 10% for all values. The attenuation of the neutron flux

in each material is different which is represented by the different decline gradients, from one order of magnitude in the area from plasma to vacuum vessel, and in three orders of magnitude in the vacuum vessel area. The high decrease gradient in the vacuum vessel shield is due to its steel and water mixture. Water is a very good reflector and moderator of neutrons, because the energy transfer per interaction between a neutron and a hydrogen nucleus is high. The back scattering of neutrons is seen in the VV inner shell where the low energy flux has a very low gradient. The EU DEMO tokamak requirements [Fis15] [Bac18] for the neutron flux cannot be fulfilled in the area of the superconducting field coils with the current stellarator geometry. The neutron flux in HELIAS is a factor of 10 higher than the specification of the EU DEMO tokamak requirement. This means that the current HELIAS design does not provide enough neutron shielding outside the vacuum vessel currently to protect the superconducting non-planar shaped field coils.

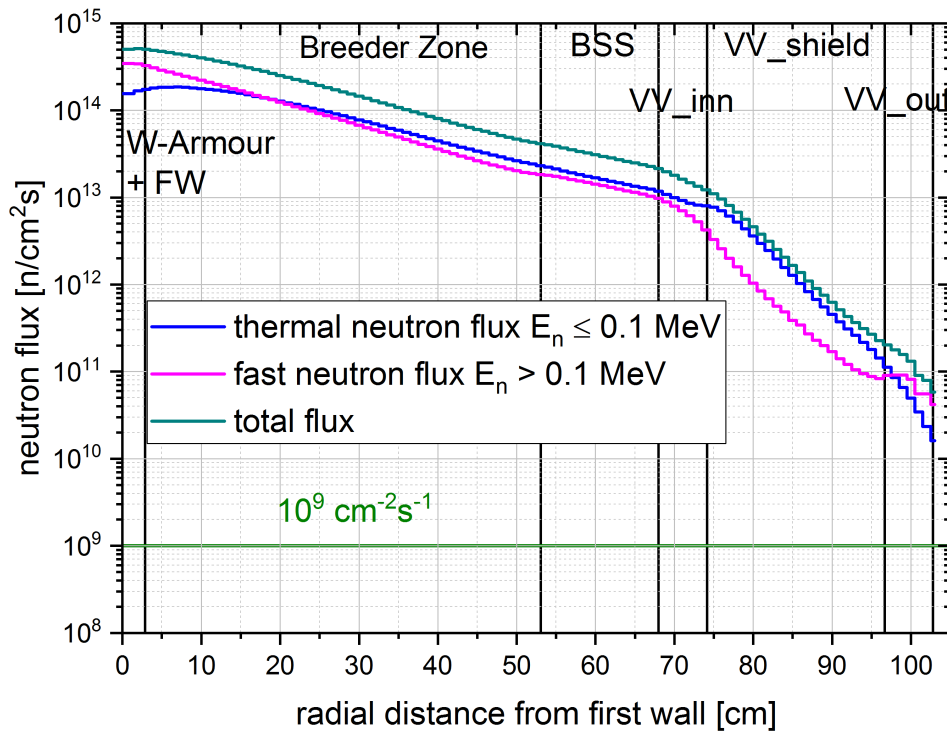


Figure 7.11: Calculated radial profile of the thermal, fast and total neutron flux as function of the radial distance from first wall in the position  $R = 2245$  cm to  $R = 2142$  cm,  $z = -30$  cm, and  $\varphi = 5^\circ$ . The relative statistical error is below 10% for all calculated values. The EU DEMO tokamak target neutron flux of  $10^9 \text{ cm}^{-2}\text{s}^{-1}$  in respect to the superconducting magnetic field coils is indicated as green line.

The available radial space inside a stellarator is defined by the space between the fusion plasma and the superconducting non-planar shaped field coils, which define the form of the vacuum vessel. A radial extension of the vacuum vessel is not possible,

meaning that the required shielding must be provided inside the currently available radial space. A possible solution to solve the shielding problem is the implementation of a larger shielding layer, which leads to a decrease of the breeding blanket zone, and/or the application of different shielding material. The breeding blanket layer in the current HELIAS configuration is uniformly 50 cm. The radial thickness of the breeding zone in the EU DEMO tokamak at the equatorial mid plane inboard side is 22 cm [Per17]. The reduction of the breeding zone in HELIAS will reduce the TBR value, but will provide additional space available for radiation shielding. The additional shielding can be integrated inside the breeding blanket or attached between the breeding blanket and the vacuum vessel. Possible shielding materials like tungsten carbide (WC), tungsten boron (WB), or boron carbide ( $B_4C$ ) [Per20] can be applied. The WC and WB shielding layer will increase the weight drastically and thus cause problems with the remote maintenance capability. Another material option to increase the shielding capability is metal hydride, like yttrium hydride ( $YH_{1.6}$  and  $YH_{1.75}$ ) or zirconium hydride ( $ZrH_{1.6}$ ) [Per20], which must be encapsulated applied in the fusion reactor. All these possible options need to be considered carefully to simultaneously fulfil the tritium self-sufficiency and the shielding requirements.

### 7.4.2 Nuclear power density

The nuclear power density represents the nuclear heating induced by neutrons and secondary particles, created due to the interaction of neutrons with matter. The secondary particles, like photons, neutrons, other particles, have a significant contribution to the nuclear heating. Therefore it is important to set-up an MCNP multiplication cards to register neutron and photon heating.

Design requirement for EU DEMO tokamak is a maximum power density of  $50 \text{ W m}^{-3}$  as peak nuclear heating in the winding pack of the coils [Fis15] [Bac18]. The MCNP result is presented as the summed up result of the neutron and photon heating and can be seen in figure 7.12, in which the EU DEMO tokamak design requirement is indicated. The calculated results in the region of interest in HELIAS significantly exceed the radiation load limits for DEMO. The heating result of the vacuum outside layer of HELIAS is  $1170 \text{ W m}^{-3}$ , which is a factor of 23.4 higher than the DEMO design requirement. The relative statistical error is below 9% for each value obtained in the calculation. The decrease of the nuclear heating corresponds to the total neutron flux behaviour. In the VV shield layer, an increase is observed caused by the water in the shielding layer leading to back scattering of neutrons associated with a higher heat



release at the inner vacuum vessel layer.

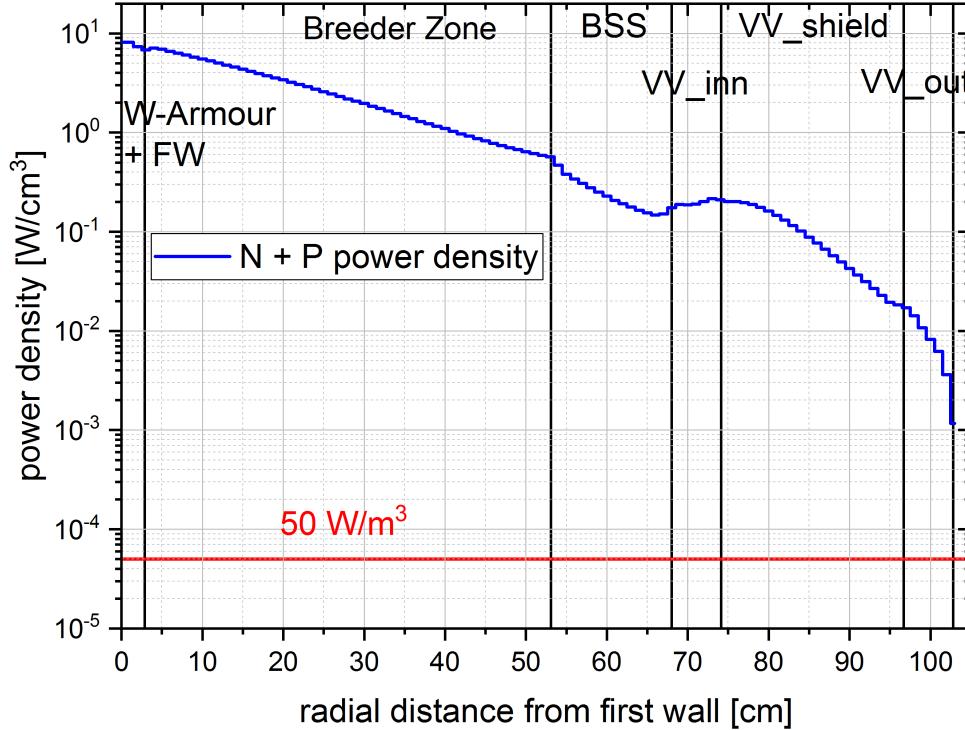


Figure 7.12: Calculated radial profile of the nuclear power density for neutrons and photons as function of the radial distance from first wall in the position  $R = 2245$  cm to  $R = 2142$  cm,  $z = -30$  cm, and  $\varphi = 5^\circ$ . The relative statistical error is below 9% for all calculated values. The EU DEMO tokamak design limit of the peak power density in the winding pack of the magnets of  $50 \text{ W m}^{-3}$  is indicated as red line.

The obtained results can be compared to the results from the EU DEMO tokamak [Per17]. In this paper, the nuclear power density is calculated at the inboard mid-plane with a NWL of  $\sim 1.1 \text{ MW m}^{-2}$ . Different integrated shielding concepts inside the BSS are investigated which are illustrated in figure 7.13. One concept is only using ‘Eurofer steel’ as shielding material that is very similar to the set-up in HELIAS. The curve in [Per17] has the same gradient compared to the HELIAS results with a decrease around one order of magnitude in the layers between firstwall and begin of VV, and a very high gradient inside the VV that includes also a steel and water mixture as shielding material. The same behaviour can be seen in the HELIAS results which provides confidence that the performed calculations are correct. The results in [Per17] show that the EU DEMO tokamak design requirements are fulfilled in a radial distance of  $\sim 145$  cm away from plasma. Transferred to the HELIAS geometry, it can be concluded that sufficient shielding with the current material set-up in the limited space cannot be reached and larger shielding layer and/or more efficient shielding material must be applied. This is possible with a reduction of the breeding zone and introduction of

shielding material like tungsten carbide (WC) or metal hydrides.

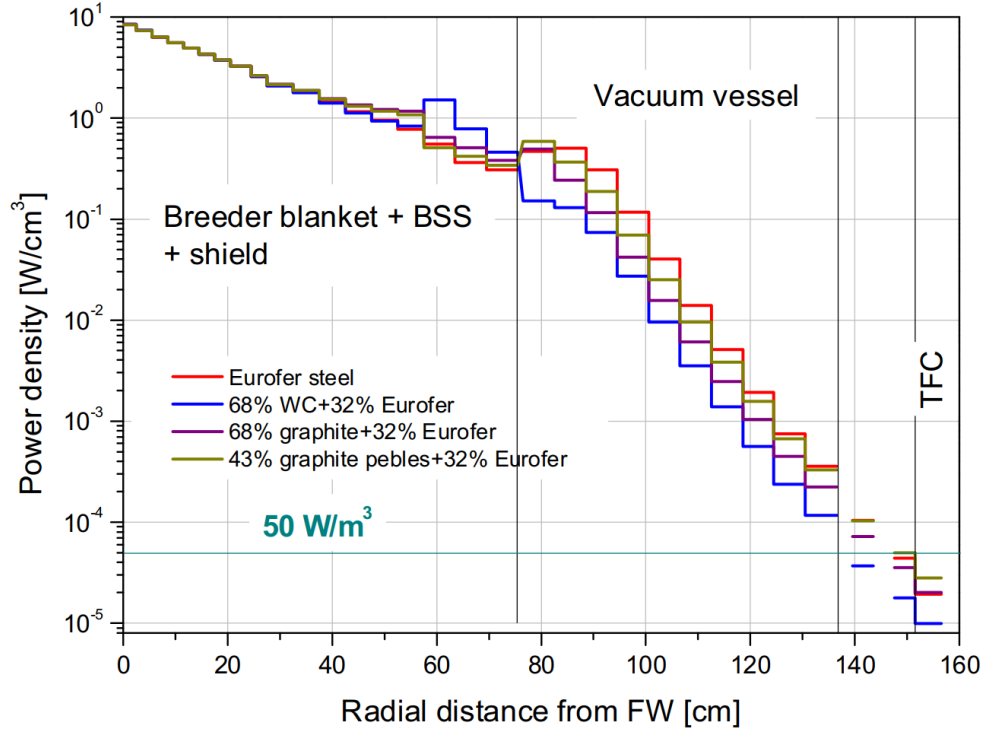


Figure 7.13: Calculated radial power density profile at EU DEMO tokamak inboard mid-plane [Per17].

### 7.4.3 Radiation damage

Neutron induced material degradation is a critical value for in-vessel components, because the displacement damage, together with the component temperature, determine the total lifetime of a reactor component. Additionally, the radiation damage value has an impact on the choice of the reactor materials. The Displacement Per Atom (DPA) concept is developed in material science, based on neutron flux experiments with different materials and correlated to the standard radiation damage Norgett-Robinson-Torrens (NRT) model [Nor75]. This approach ‘calculates the number of atomic displacements produced in a damage cascade by a primary knock-on atom of known energy’ [Nor75] and it is widely used in fusion technology to judge if the components are keeping their structural integrity or their functionality [Fis18].

The calculation of the damage rate per Full Power Year (FPY) can be seen in equation 7.3 [Fis18]:

$$\text{Damage Rate[dpa/fpy]} = \text{Flux[n/cm}^2\text{/s]} \times \sigma_{dpa}[\text{b}] \times 10^{-24} \text{ cm}^2 \text{ b}^{-1} \times 3.1557 \times 10^7 \text{ s/fpy}, \quad (7.3)$$

where the flux is represented by the normalised neutron fluence. The normalisation in MCNP is given by the neutron birth rate per second, to obtain the true neutron flux. The displacement cross-section  $\sigma_{dpa}$  in equation 7.3 is calculated by equation 7.4 [Sim18]:

$$\sigma_{dpa} = 0.8 \times E_{dam}[\text{b MeV}^{-1}] \times 10^6 \text{ eV MeV}^{-1} / (2 \times E_{thresh}[\text{eV}]), \quad (7.4)$$

where  $E_{dam}$  is the damage energy and  $E_{thresh}$  is the threshold energy per reaction. The focus for the radiation damage assessment is the element iron, because iron is the main constituent of the steel used in the breeding blanket and vacuum vessel structure of the HELIAS model. It is an essential element in the reactor life-time components and the damage of iron is the relevant quantity if a component is applicable inside the fusion reactor. The radiation induced material strength degradation, like embrittlement, is an issue for ferritic and austenitic stainless steel, which is assumed for the vacuum vessel. The calculation of the displacement damage returns the artificial number of iron atoms that change their positions in the crystal lattice during the radiation time without taking recombination effects into account. This means that the main focus in this calculation is in respect to the DPA values of the vacuum vessel, because it is a life-time component of the reactor.

The MCNP mesh tally is normalised with a tally multiplication card to obtain the damage rates for the element iron. The normalisation factor for the current HELIAS model is  $3.36240 \times 10^7$  which represents  $\sigma_{dpa}$  for one FPY, as seen in equation 7.3, to return the damage rate in ‘DPA/FPY’. The results of this calculation are shown in figure 7.14. The displacement rate is decreasing in radial direction by a factor of 10 faster than the neutron flux, because the kinetic energy is not exceeding to an increasing fraction the energy threshold necessary to cause radiation damage. The displacement damage in figure 7.14 has a maximum relative statistical error for all obtained values is below 7% in the calculation. Additionally, figure 7.14 refers to the EU DEMO tokamak lifetime limit of  $\leq 2.75$  dpa/lifetime in the vacuum vessel to ensure that the fracture toughness is reduced by no more than 30% [Fis15] [Bac18]. The displacement damage level obtained for the front of the vacuum vessel is  $\sim 0.11$  DPA/FPY. This guarantees operating HELIAS for 25 full power years until the EU DEMO tokamak design limit is reached. For the EU DEMO tokamak first wall, made of Eurofer steel, a target design of 50 DPA is assumed [Fed14] which corresponds to a blanket lifetime of 5 FPY [Fis15]. The DPA value for the first wall in HELIAS is  $\sim 11$  DPA/FPY. The obtained material damage rate in the first wall is sufficient to fulfil an operation of 5 FPY in

HELIAS. This means, that the blanket maintenance scheme, in order to change the breeding blankets after a certain time, developed for the EU DEMO tokamak, can be considered and the DPA is not the limiting factor in the HELIAS design.

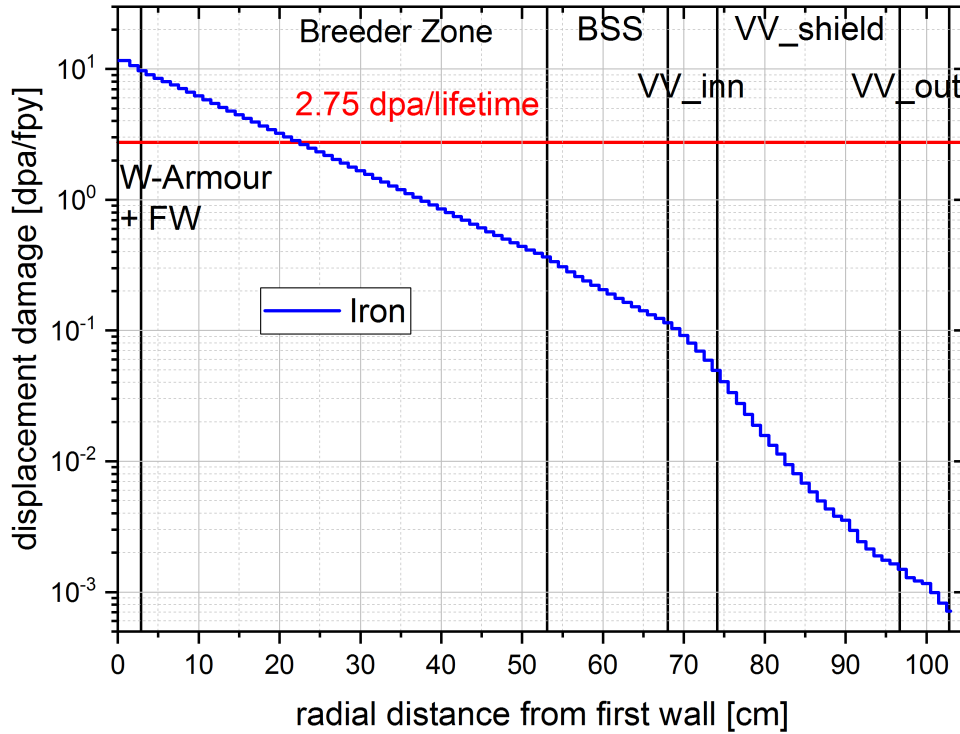


Figure 7.14: Calculated radial profile of the displacement damage of iron for one full power year as function of the radial distance from first wall in the position  $R = 2245$  cm to  $R = 2142$  cm,  $z = -30$  cm, and  $\varphi = 5^\circ$ . The relative statistical error is below 7% for all calculated values. The EU DEMO tokamak design limit of 2.75 dpa/lifetime for the vacuum vessel is indicated as red line.

#### 7.4.4 Gas production

Neutron induced interactions with matter cause gas production, like helium, which can lead to swelling and embrittlement of material [Gil13]. It is thus important to investigate the gas production rate for helium and hydrogen, because both gas molecules are generated by neutron induced material interactions and have an effect on the structural stability.

The criteria for the material stability is the assumption, that ‘re-welding of stainless steel is feasible at He concentrations below 1 appm’ [Bar07], [Bac18]. The EU DEMO tokamak design goal is actually to necessitate re-welding only at such locations where sufficient shielding can be provided, e.g. in the vessel ports or at the bottom of the blanket segments, and do the re-welding during the blanket replacement [Fis15].

The MCNP tally multiplication card for the gas production is similarly constructed as the DPA tally multiplication card. It is set-up to return the gas production for hydrogen and helium in EUROFER [Fin09] in ‘Atomic Parts Per Million (appm) / Full Power Year (FPY)’. The MCNP mesh tally registers the particle flux and it assumes that each mesh cell is filled with EUROFER, independent from the real material configuration in the stellarator geometry. The gas production rate is a conversion factor into ‘appm’ which includes the total radiation time of one FPY and has the value ‘ $3.36240 \times 10^9$ ’.

The obtained result of the gas production of helium and hydrogen is presented in figure 7.15 including the 1 appm limit for the EU DEMO tokamak. Their maximum relative statistical error for all obtained values is below 4% for helium and below 6% for hydrogen respectively. The reduction of the gas production rate in dependency of the radial distance from the plasma is about a factor of 1000 higher than the decrease of the neutron flux. Interestingly, an increase of the helium production in the area between the inner vacuum vessel and the vacuum vessel shield can be seen. This is caused by boron, which is with 0.002 wt.% part of the material mixture used in the blanket, with 0.001 wt.% part of EUROFER used in the first wall and the back support structure, and with 0.001 wt.% part of the SS-316 stainless steel used in the vacuum vessel as well as in the steel-water shielding layer. The cross-section for neutron induced helium production in boron increases significantly for low energy neutrons. In comparison to figure 7.11, the low energy neutron flux increases in the vacuum vessel area as well. A comparison calculation, using EUROFER steel in the mesh tally definition without boron, shown in figure 7.16, reveals that the boron concentration definitely caused the helium production increase in the vacuum vessel area. The hydrogen production is not affected by the boron concentration and is similar in both cases, with a slight difference in the vacuum vessel outside area caused by the Monte Carlo Method in the particle transport calculation.

The HELIAS results can be compared to the results published in [Gil13]. This paper investigates the ‘Neutron-induced dpa, transmutations, gas production, and helium embrittlement of fusion materials’ for the EU DEMO tokamak with a fusion power of  $E_{fus} = 3000$  MW. The gas production is investigated for iron (Fe), which is the primary constituent of steel, and ‘chromium (Cr), which forms around 10% of the composition of the reduced activation steels being proposed for fusion application, has a very similar transmutation profile to Fe’ [Gil13]. The investigated position ‘equatorial plane, inboard side’ for the EU DEMO tokamak in this paper is used for the comparison of the results, because this position is the closest to the investigated posi-

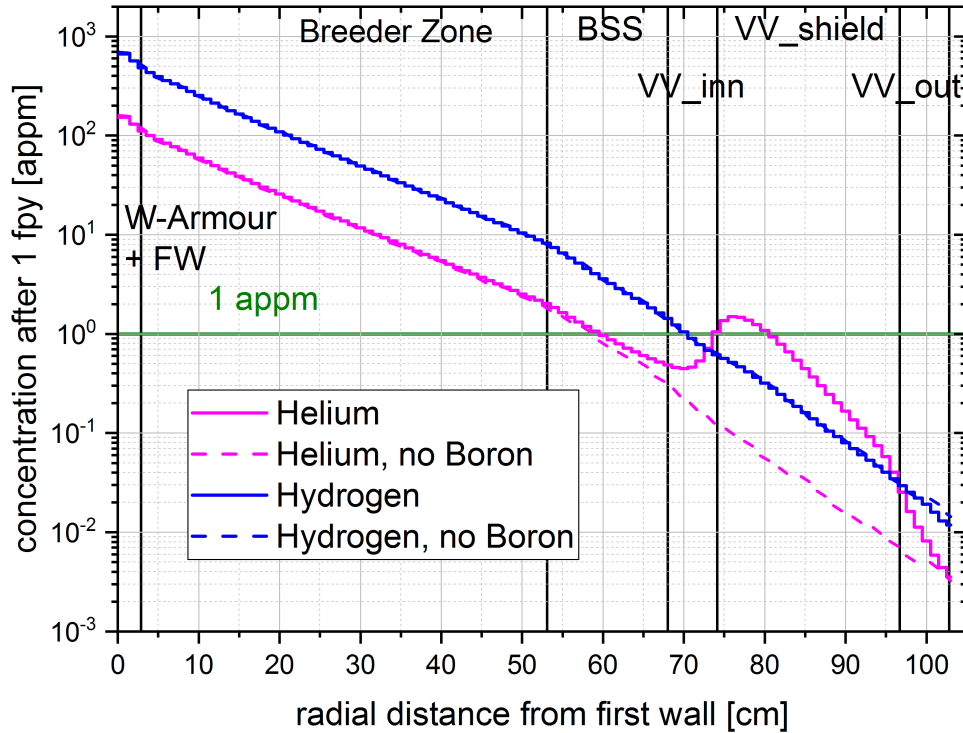


Figure 7.15: Calculated radial profile of the helium and hydrogen production in iron steel for one full power year as function of the radial distance from first wall in the position  $R = 2245$  cm to  $R = 2142$  cm,  $z = -30$  cm, and  $\varphi = 5^\circ$ . The relative statistical error is below 4% for helium and below 6% for hydrogen in all calculated values. The EU DEMO tokamak re-welding design criterion of stainless-steel of 1 appm is indicated as green line.

tion in HELIAS. Two different comparisons for the gas production can be done against the HELIAS results. At first, the helium and hydrogen concentration after one FPY on the first wall surface. These are  $\sim 150$  appm in [Gil13] vs. 154 appm in HELIAS for helium and  $\sim 650$  appm in [Gil13] vs. 665 appm in HELIAS for hydrogen. The results of the two different investigations show that the values are very close to each other. This means that the same gas production rates in a stellarator power reactor can be expected as calculated for a EU DEMO tokamak power reactor of similar fusion power.

The second comparison can be done for the radial helium generation from first wall to the vacuum vessel. This can be seen for [Gil13] in figure 7.17. It must be noted that these results are calculated for three FPY, therefore figure 7.18 is introduced which represents the helium concentration for HELIAS after three FPY.

In [Gil13], the bin sizes are very coarse and non-regular. For example, small bin sizes covering the first wall from 1 to 2 cm and the breeding blanket area in step sizes of approximately 1 to 5 cm. The bin sizes in the backplate, shielding and vacuum vessel are much coarser, between 20 to 70 cm, and large gaps in-between are represented. The comparison between the figures 7.17 and 7.18 shows that the decrease of the helium

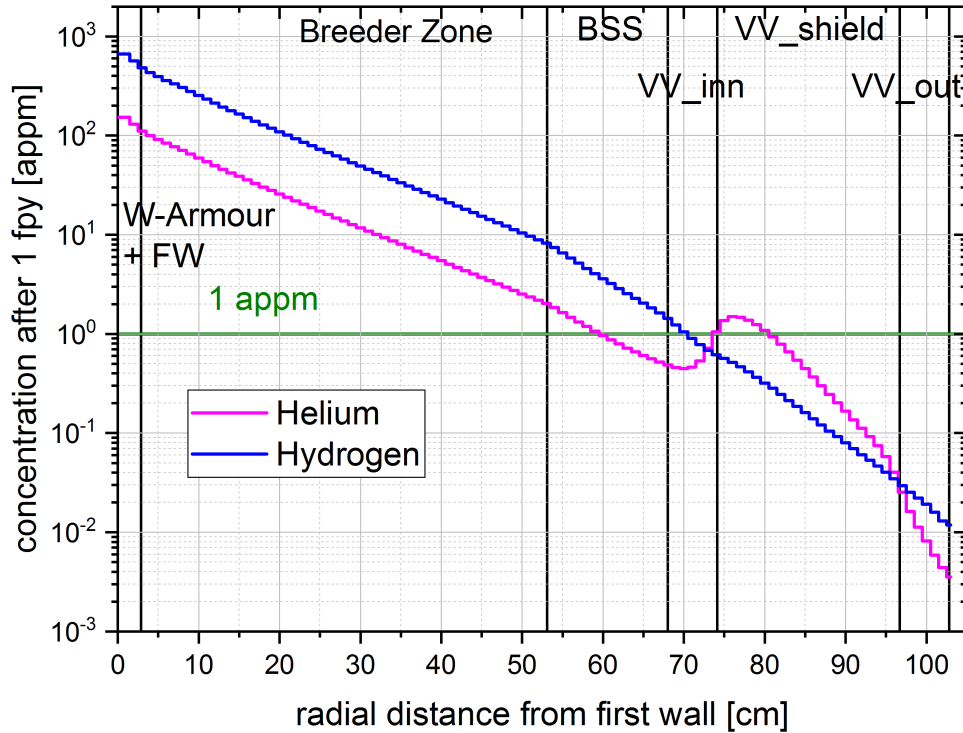


Figure 7.16: Calculated radial profile of the helium and hydrogen production in iron steel in comparison with and without boron content in the homogenised material mixtures for one full power year as function of the radial distance from first wall in the position  $R = 2245$  cm to  $R = 2142$  cm,  $z = -30$  cm, and  $\varphi = 5^\circ$ . The relative statistical error is below 4% for helium and below 6% for hydrogen in all calculated values. The EU DEMO tokamak re-welding design criterion of stainless-steel of 1 appm is indicated as green line.

concentration in radial distance, also in its steepness, is represented for the EU DEMO tokamak and HELIAS. The re-welding criterion of 1 APPM helium can be ensured in both cases for the 62 – 82 cm, if the HELIAS case ‘no boron’ is taken into account.

The gas production in the first wall is above 400 appm in [Gil13] and HELIAS. As comparison, the results for the ‘no boron’ case of HELIAS is used. The paper [Gil13] show the helium for a bin size of 2 cm, resulting in  $\sim 420$  appm. The helium production rate of HELIAS is in the 1<sup>st</sup> cm: 481 appm and in the 2<sup>nd</sup> cm: 392 appm, which is an average helium production rate of 436 appm. The results of [Gil13] and HELIAS are comparable with a deviation of 4%. It must be noted that the helium concentrations in the range of 400 appm are known to cause a change in the fracture behaviour of neutron-irradiated steels compared to those exposed to neutrons alone [Yam06], [Gil13].

The gas production rates can be compared further. For the radial distance from first wall range 62 – 82 cm, which is the backplate in [Gil13], is a gas production rate of 0.5 appm obtained, while HELIAS has a rate of 0.44 appm at 72 cm, corresponding to

the vacuum vessel inner layer, of the radial distance from first wall. A larger difference is visible at the position 92 – 122 cm, which is the shield in [Gil13], and the HELIAS results at this position is 0.05 appm for [Gil13] vs. 0.011 appm for HELIAS ‘no boron’ case. The difference is caused by the radiation shielding, which starts in HELIAS at the radial position of 74 cm containing the water-steel material mixture.

The comparison gives confidence that the HELIAS calculations can reproduce already generated results of the EU DEMO tokamak. The obtained gas production rate for HELIAS has the same order of magnitude as obtained in the EU DEMO tokamak calculations of [Gil13]. The material applied in HELIAS must be selected carefully to withstand the neutron flux, the radiation damage and the high gas production rate in the first wall.

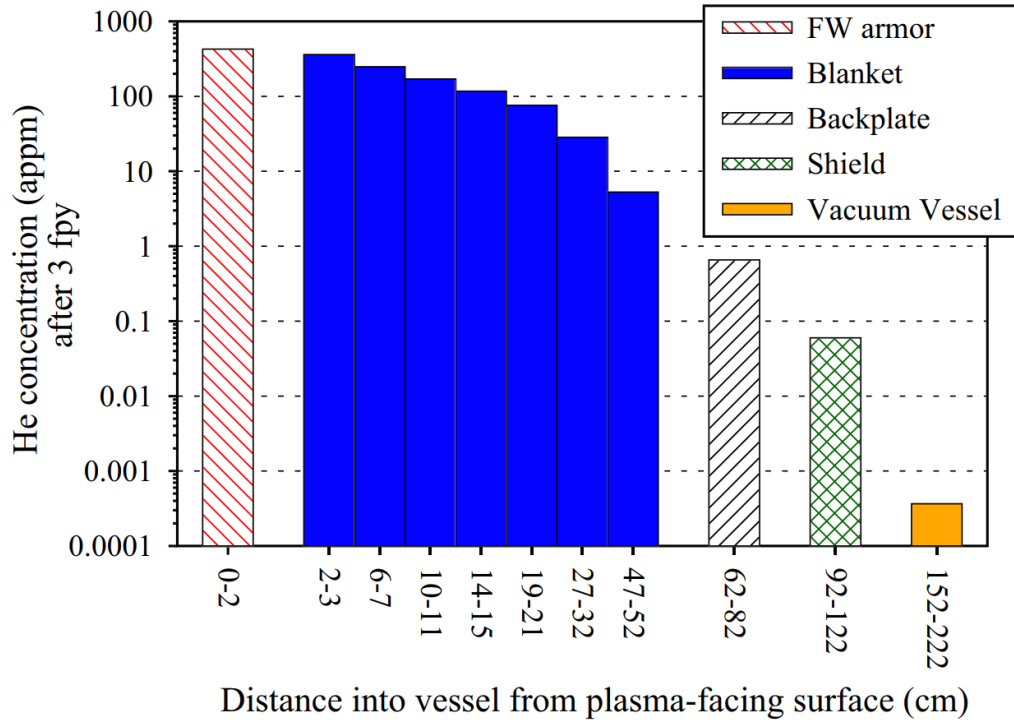


Figure 7.17: Average variation in helium concentration in pure iron after 3 FPY irradiation in different radial zones of a EU DEMO tokamak as a function of the distance from the plasma-facing surface of DEMO at mid plane outboard [Gil13].



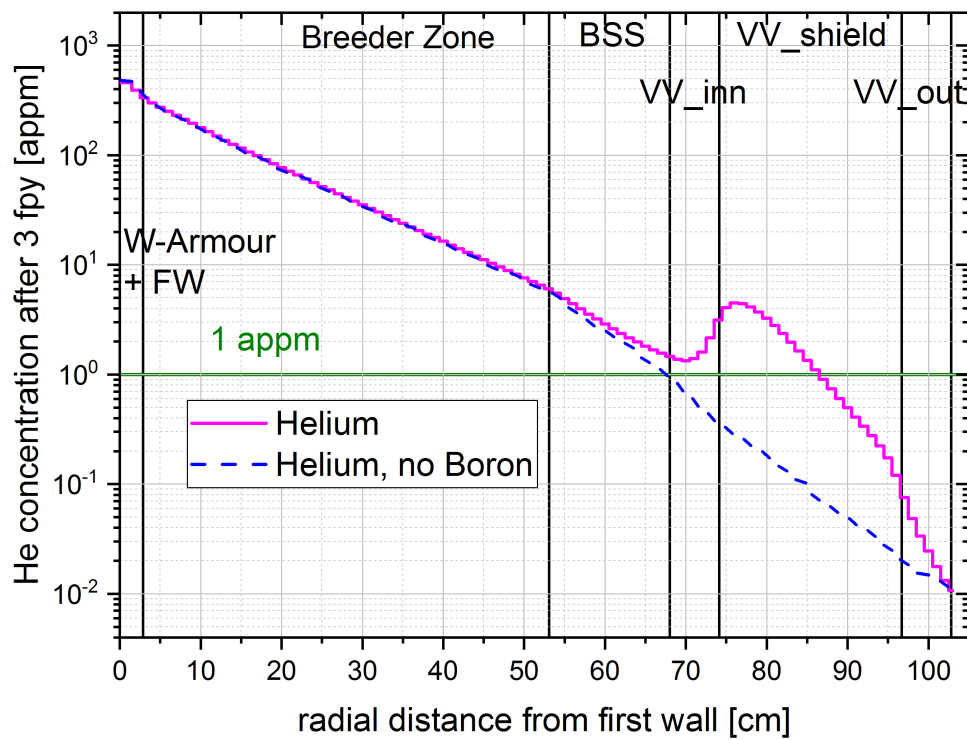


Figure 7.18: Calculated radial profile of the helium production in iron steel in comparison with and without boron content in the homogenised material mixtures for three full power years as function of the radial distance from first wall in the position  $R = 2245$  cm to  $R = 2142$  cm,  $z = -30$  cm, and  $\varphi = 5^\circ$ . The relative statistical error is below 4% in all calculated values. The EU DEMO tokamak re-welding design criterion of stainless-steel of 1 appm is indicated as green line.

# Chapter 8

## Summary and Outlook

An investigation of the stellarator power reactor HELIAS from the neutronics point of view has been presented in the thesis. Compared to a tokamak reactor, the stellarator poses challenges due to its complex geometry requiring substantial modifications of approaches and methods to make it available for neutronic analyses.

The spatial representation of the fusion plasma and the corresponding neutron source distribution is an essential part of an MC particle transport simulation. Here, a neutron source distribution is generated by plasma physics calculations at IPP Greifswald. An MCNP user specific source subroutine has been developed to read the neutron source distribution on a 3D-grid and sample the source particles accordingly. This source subroutine has been tested and verified independently to ensure the representation of the plasma source for neutron transport simulations.

The complex toroidal twisted stellarator geometry is created by higher-order surfaces to follow the shape of the magnetic field. For the transfer of a HELIAS CAD model into a MC geometry, three different geometry transfer options are investigated and tested on a simplified CAD model. This study scopes the CSG approach, the faceted geometry formed by a triangular surface mesh on the CAD geometry, and the unstructured mesh geometry. All options show comparable results within their statistical uncertainty in the neutronic calculations. However, based on the expected need to use more detailed design models, the use of the faceted type geometry in the DAGMC approach is considered to be the most promising option, because it is capable of using complex geometries without any restrictions.

The original CAD envelope model, provided by IPP Greifswald, contains only a single solid layer to represent the in-vessel components of the stellarator. For a more realistic neutronic simulation, the CAD geometry model has been separated radially into different functional layers to represent the breeding blanket, the back supporting

structure, the vacuum vessel and the shielding. Each layer is assigned to a representative homogenised material mixture, which allows a first study of the preliminary design. Here, a helium cooled solid breeding blanket (HCPB) is assumed and in its material composition adapted for HELIAS. The NWL distribution is calculated by two different approaches, one at KIT and one at IPP, which shows a good agreement within statistical uncertainty among them. The NWL on the plasma facing surface exhibit a peak load of  $\sim 1.93 \text{ MW m}^{-2}$  and an average load of around  $\sim 0.95 \text{ MW m}^{-2}$ . The high maximum NWL exceeds the HCPB design limits for the heat removal, which means that an adapted cooling design must be implemented to the stellarator first wall. The cooling design comprise the coolant (e.g gas as He or  $\text{CO}_2$ ), the adjustment of the coolant flow and an improved cooling scheme in the first wall and breeding blanket. These options need to take into account in the HELIAS design iterations. The neutron flux distribution has been obtained on a fine 3D mesh covering a  $36^\circ$  stellarator sector model. It yields a peak flux inside the plasma chamber of  $4 \times 10^{14} \text{ n/cm}^2/\text{s}$ , which is attenuated through the blanket and vacuum vessel down to  $1 \times 10^{10} \text{ n/cm}^2/\text{s}$ . The TBR estimated in this configuration is  $1.3863 \pm 0.0001$ . This is a rather optimistic value due to the assumption of a homogenised material mixture in a specific blanket design and disregarding any wall coverage by e.g. ports for the heating system, vacuum exhaust, diagnostics and other components. Nevertheless, this is a very promising starting point for stellarator breeding blanket development, as the margin to the required TBR value is high and any heterogeneity in the modelling, as well as introduction of ports, will reduce the TBR.

The vacuum vessel and its in-vessel components need to provide sufficient shielding for the radiation protection of sensitive equipment and for radiological protection of the power plant. The attenuation of the plasma neutron flux by four orders of magnitude through the bulk shield of the plasma confinement leads to statistical convergence issues of standard, analogue MC transport simulations. Suitable variance reduction methods are thus required to generate a sufficiently high number of particle tracks in these areas to reduce the relative statistical error to an acceptable value, typically  $\leq 10\%$ . The mesh based weight window technique, as available with the MCNP code and applied with the ADVANTG code, has been studied and successfully applied for the first shielding evaluation of HELIAS. The shielding performance has been assessed with the conservative current design assumption of a NWL of  $\sim 1.35 \text{ MW m}^{-2}$  at an area with minimum radial thickness of  $\sim 1.0 \text{ m}$ . In this case, the requirements specified for the EU DEMO tokamak fusion reactor on the maximum nuclear heat and on the maximum neutron flux, both with respect to protecting the superconducting field coils,

cannot be met by far. The results of the HELIAS shielding evaluation still indicate the need for enhancing the shielding capabilities by increasing the radial thickness of in-vessel and vessel shielding and/or apply advanced shielding materials like tungsten carbide (WC) or metal hydrides.

To summarise, for the first time a comprehensive neutronic investigation of the stellarator power reactor HELIAS has been conducted. It is based on a computational radiation transport methodology which has been carefully tested and successfully verified. The neutronics simulation approach for the stellarator type fusion reactor, presented in the thesis, is applicable to future analyses of engineering designs for this reactor type.

The current available HELIAS CAD geometry is limited and not preferred for design iterations and optimisations. The development of a parametric CAD geometry, which is usable for neutronics and multi-physics investigations, must be developed to ensure the model consistency in the design optimisation process. The parametric model has to be flexible in a sense of the stellarator field-periodicity and the total radial thickness between the firstwall and the vacuum vessel. Additionally, the CAD model must allow the integration of specific engineering design, like a heterogeneous breeding blanket module. The development of such an approach has to take the geometry limitations of the neutronics and multi-physics codes into account to ensure that a change in the CAD design can be easily adapted to the computational model.

# References

- [Ale01] C. Alejaldre, L. Almoguera, J. Alonso, et al.: *Review of confinement and transport studies in the TJ-II flexible heliac*. In: *Nuclear Fusion*, vol. 41 (2001), no. 10, pp. 1449–1457. doi:10.1088/0029-5515/41/10/312
- [Alk05] Z. Alkan, B. Barré, R. Bock, et al.: *Energy Technologies - Subvolume B: Nuclear Energy*. Springer Berlin Heidelberg New York, 2005. ISBN 978-3-540-42891-6
- [And06] R. Andreani, E. Diegele, W. Gulden, et al.: *Overview of the European Union fusion nuclear technologies development and essential elements on the way to DEMO*. In: *Fusion Engineering and Design*, vol. 81 (2006), no. 1-7, pp. 25–32. ISSN 0920-3796. doi:10.1016/j.fusengdes.2005.09.005
- [Ans18] *ANSYS Workbench User Guide*, vol. 19.0. 2018. URL [https://ansyshelp.ansys.com/account/secured?returnurl=/Views/Secured/corp/v190/wb2\\_help/wb2\\_help.html](https://ansyshelp.ansys.com/account/secured?returnurl=/Views/Secured/corp/v190/wb2_help/wb2_help.html). Last accessed on July 19, 2020
- [Bac18] C. Bachmann, S. Ciattaglia, F. Cismondi, et al.: *Overview over DEMO design integration challenges and their impact on component design concepts*. In: *Fusion Engineering and Design*, vol. 136 (2018), pp. 87–95. ISSN 0920-3796. doi:10.1016/j.fusengdes.2017.12.040
- [Bar07] V. Barabash, A. Peacock, S. Fabritsiev, et al.: *Materials challenges for ITER – Current status and future activities*. In: *Journal of Nuclear Materials*, vol. 367-370 (2007), pp. 21–32. ISSN 0022-3115. doi:10.1016/j.jnucmat.2007.03.017
- [Bet08] K. Bethge, G. Walter, and B. Wiedemann: *Kernphysik : Eine Einführung*. Springer-Lehrbuch, 3<sup>rd</sup> edn. Berlin, Heidelberg: Springer-Verlag, 2008. ISBN 978-3-540-74567-9

- [Bla17] T. Blacker, S. J. Owen, M. L. Staten, et al.: *CUBIT - Geometry and Mesh Generation Toolkit, 15.3 User Documentation*. Sandia National Laboratories, Albuquerque, New Mexico 87185 and Livermore, California 94550, 2017. URL [https://cubit.sandia.gov/public/15.3/help\\_manual/WebHelp/cubithelp.htm](https://cubit.sandia.gov/public/15.3/help_manual/WebHelp/cubithelp.htm). SAND2017-6895 W, Printed July 2017. Last accessed on July 19, 2020
- [Boc16] L. Boccaccini, G. Aiello, J. Aubert, et al.: *Objectives and status of EUROfusion DEMO blanket studies*. In: *Fusion Engineering and Design*, vol. 109–111, Part B (2016), pp. 1199–1206. ISSN 0920-3796. doi:10.1016/j.fusengdes.2015.12.054
- [Boo85] T. E. Booth: *A Sample Problem for Variance Reduction in MCNP*. Los Alamos National Laboratory, USA, October 1985. LA-10363-MS
- [Bor11] M. Borlein: *Kerntechnik: Grundlagen*. 2<sup>nd</sup> edn. Würzburg: Vogel Buchverlag, 2011. ISBN 978-3-8343-3253-0
- [Cac10] D. G. Cacuci (Editor): *Handbook of Nuclear Engineering*, vol. I: Nuclear Engineering Fundamentals. Institute for Nuclear Technology and Reactor Safety, Karlsruhe Institute Technology (KIT): Springer Science+Business Media, LLC, Boston, MA, 2010. ISBN 978-0-387-98130-7. doi:10.1007/978-0-387-98149-9
- [Cas17] F. Castejón, D. Alegre, A. Alonso, et al.: *3D effects on transport and plasma control in the TJ-II stellarator*. In: *Nuclear Fusion*, vol. 57 (2017), no. 10, p. 102022. doi:10.1088/1741-4326/aa7691
- [Cor20] Coreform: *Trelis 17.1 User Documentation*, 2020. URL [https://www.coreform.com/trelis\\_help/trelishelp.htm](https://www.coreform.com/trelis_help/trelishelp.htm). Last accessed on July 19, 2020
- [DD91] M. Dalle Donne, C. Adelhelm, H. Baschek, et al.: *Status report KfK contribution to the development of DEMO-relevant test blankets for NET/ITER. Part 2: BOT Helium Cooled Solid Breeder Blanket, Volume 2: Detailed Version*. Tech. Rep., Kernforschungszentrum Karlsruhe, Karlsruhe, October 1991. KfK 4929
- [DD94] M. Dalle Donne, H. Albrecht, L. Boccaccini, et al.: *European DEMO BOT*

- solid breeder blanket*. Tech. Rep., Kernforschungszentrum Karlsruhe, Karlsruhe, November 1994. KfK 5429
- [Don18] T. Donné and W. Morris: *European Research Roadmap to the Realisation of Fusion Energy*. Garching / Munich: EUROfusion Programme Management Unit, November 2018. ISBN 978-3-00-061152-0
- [DS58] G. G. Dolgov-Saveliev, D. P. Ivanov, V. S. Mukhovatov, et al.: *Investigations of the Stability and Heating of Plasmas in Toroidal Chambers*. In: *Proceedings of the Second United Nations International Conference on the Peaceful Uses of Atomic Energy*, vol. 32 (1958), pp. 82–91. United Nations, Geneva
- [Dup02] S. A. Dupree and S. K. Fraley: *A Monte Carlo primer : a practical approach to radiation transport*, vol. 1. New York: Kluwer Academic/Plenum, 2002. ISBN 0-306-46748-8
- [EG09] L. A. El-Guebaly and S. Malang: *Toward the ultimate goal of tritium self-sufficiency: Technical issues and requirements imposed on ARIES advanced power plants*. In: *Fusion Engineering and Design*, vol. 84 (2009), no. 12, pp. 2072–2083. ISSN 0920-3796. doi:10.1016/j.fusengdes.2008.12.098
- [Fed14] G. Federici, R. Kemp, D. Ward, et al.: *Overview of EU DEMO design and R&D activities*. In: *Fusion Engineering and Design*, vol. 89 (2014), no. 7–8, pp. 882–889. ISSN 0920-3796. doi:10.1016/j.fusengdes.2014.01.070
- [Fed19] G. Federici, L. Boccaccini, F. Cismondi, et al.: *An overview of the EU breeding blanket design strategy as an integral part of the DEMO design effort*. In: *Fusion Engineering and Design*, vol. 141 (2019), pp. 30–42. ISSN 0920-3796. doi:10.1016/j.fusengdes.2019.01.141
- [Fin09] Final Report on the EFDA Article 7 contract EFDA/06-1903 on: *Procurement of reduced activation ferritic-martensitic steel type 9CrW<sub>10</sub>TaV (EUROFER) for the TBM fabrication technology trials and mock-ups*. Tech. Rep., EFDA, July 2009. Saarschmiede GmbH
- [Fis08] U. Fischer, P. Pereslavytsev, D. Große, et al.: *Model Generation and Neutronic Design Analyses for the European DEMO Conceptual Study*. Techreport Volume 1.0, Forschungszentrum Karlsruhe, Institut für Reaktorsicherheit, Postfach 3640, 76021 Karlsruhe, Germany, July 2008. URL <https://idm.euro-fusion.org/?uid=2AHVKD&version=v1.0>. Final report on

- EFDA task TW6-TRP-005, Deliverable 1a; Report IDM reference No.: EFDA\_D\_2AHVKD
- [Fis14] U. Fischer, C. Bachmann, B. Bienkowska, et al.: *Neutronic analyses and tools development efforts in the European DEMO programme*. In: *Fusion Engineering and Design*, vol. 89 (2014), no. 9–10, pp. 1880–1884. ISSN 0920-3796. doi:10.1016/j.fusengdes.2014.02.013
- [Fis15] U. Fischer, C. Bachmann, I. Palermo, et al.: *Neutronics requirements for a DEMO fusion power plant*. In: *Fusion Engineering and Design*, vol. 98-99 (2015), pp. 2134–2137. ISSN 0920-3796. doi:10.1016/j.fusengdes.2015.02.029
- [Fis16] U. Fischer, C. Bachmann, J.-C. Jaboulay, et al.: *Neutronic performance issues of the breeding blanket options for the European DEMO fusion power plant*. In: *Fusion Engineering and Design*, vol. 109-111 (2016), pp. 1458–1463. ISSN 0920-3796. doi:10.1016/j.fusengdes.2015.11.051
- [Fis18] U. Fischer: *Guidelines for Neutronic Analyses*. Techreport Volume 1.7, EUROfusion, 2018. URL <https://idm.euro-fusion.org/?uid=2L8TR9&version=v1.7>. Report IDM reference No.: EFDA\_D\_2L8TR9
- [Fis20] U. Fischer, L. Boccaccini, F. Cismondi, et al.: *Required, achievable and target TBR for the European DEMO*. In: *Fusion Engineering and Design*, vol. 155 (2020), pp. 111553/1–111553/6. ISSN 0920-3796. doi:10.1016/j.fusengdes.2020.111553
- [Gat18] D. A. Gates, D. Anderson, S. Anderson, et al.: *Stellarator Research Opportunities: A Report of the National Stellarator Coordinating Committee*. In: *Journal of Fusion Energy*, vol. 37 (2018), no. 1, pp. 51–94. ISSN 1572-9591. doi:10.1007/s10894-018-0152-7
- [Gil13] M. R. Gilbert, S. L. Dudarev, D. Nguyen-Manh, et al.: *Neutron-induced dpa, transmutations, gas production, and helium embrittlement of fusion materials*. In: *Journal of Nuclear Materials*, vol. 442 (2013), no. 1, Supplement 1, pp. 755–760. ISSN 0022-3115. doi:10.1016/j.jnucmat.2013.03.085
- [Goo12] T. Goorley, M. James, T. Booth, et al.: *Initial MCNP6 Release Overview*. In: *Nuclear Technology*, vol. 180 (2012), no. 3, pp. 298–315
- [Goo14] T. Goorley: *MCNP 6.1.1 - Beta Release Notes*. Tech. Rep., Los Alamos National Laboratory, 2014. LA-UR-14-24680



- [Gre03] B. J. Green, I. I. Team, and P. Teams: *ITER: burning plasma physics experiment*. In: *Plasma Physics and Controlled Fusion*, vol. 45 (2003), no. 5, pp. 687–706. doi:10.1088/0741-3335/45/5/312
- [Gri92] G. Grieger, W. Lotz, P. Merkel, et al.: *Physics optimization of stellarators*. In: *Physics of Fluids B: Plasma Physics*, vol. 4 (1992), no. 7, pp. 2081–2091. doi:10.1063/1.860481
- [Gro09] D. Große and H. Tsige-Tamirat: *Current Status of the CAD Interface Program McCad for MC Particle Transport Calculations*. In: *International Conference on Mathematics, Computational Methods & Reactor Physics (M&C 2009)*, (2009). Saragota Springs, New York, May 3-7, 2009, on CD-ROM, American Nuclear Society, LaGrange Park, IL (2009)
- [Har12] J. Harman: *EFDA Work Programme 2012 - DEMO Operational Concept Description*. Techreport Volume 1.3, EFDA, 2012. URL <https://idm.euro-fusion.org/?uid=2LCY7A&version=v1.3>. Report IDM reference No.: EFDA\_D\_2LCY7A
- [Her17] F. Hernández, P. Pereslavytsev, Q. Kang, et al.: *A new HCPB breeding blanket for the EU DEMO: Evolution, rationale and preliminary performances*. In: *Fusion Engineering and Design*, vol. 124 (2017), pp. 882–886. ISSN 0920-3796. doi:10.1016/j.fusengdes.2017.02.008
- [Her19] F. A. Hernández, P. Pereslavytsev, G. Zhou, et al.: *An enhanced, near-term HCPB design as driver blanket for the EU DEMO*. In: *Fusion Engineering and Design*, vol. 146 (2019), pp. 1186–1191. ISSN 0920-3796. doi:10.1016/j.fusengdes.2019.02.037
- [Hir08] M. Hirsch, J. Baldzuhn, C. Beidler, et al.: *Major results from the stellarator Wendelstein 7-AS*. In: *Plasma Physics and Controlled Fusion*, vol. 50 (2008), no. 5, pp. 1–204. doi:10.1088/0741-3335/50/5/053001. Article 053001
- [Hua17] W. Huang, G. Audi, M. Wang, et al.: *The AME2016 atomic mass evaluation (I). Evaluation of input data; and adjustment procedures*. In: *Chinese Physics C*, vol. 41 (2017), no. 3, pp. 1–344. doi:10.1088/1674-1137/41/3/030002. Article 030002
- [Hä16] A. Häußler, U. Fischer, and F. Warmer: *Neutronics source modeling for the Stellarator power reactors of the HELIAS-type*. In: *Compact at the*

- 47<sup>th</sup> Annual Meeting on Nuclear Technology (AMNT), Hamburg, Germany, (2016)*. ISBN: 978-3-926956-97-2
- [Hä17] A. Häußler, U. Fischer, and F. Warmer: *Verification of different Monte Carlo approaches for the neutronic analysis of a stellarator*. In: *Fusion Engineering and Design*, vol. 124 (2017), pp. 1207–1210. ISSN 0920-3796. doi:10.1016/j.fusengdes.2017.04.010
- [Hä18a] A. Häußler and U. Fischer: *Use of the Cell Based Importance Sampling Technique in Neutronics Shielding Calculations of a Simplified Stellarator Model*. In: *Compact at the 49<sup>th</sup> Annual Meeting on Nuclear Technology (AMNT), Berlin, Germany, (2018)*. ISBN: 978-3-926956-95-8
- [Hä18b] A. Häußler, F. Warmer, and U. Fischer: *Neutronics analyses for a stellarator power reactor based on the HELIAS concept*. In: *Fusion Engineering and Design*, vol. 136 (2018), pp. 345–349. ISSN 0920-3796. doi:10.1016/j.fusengdes.2018.02.026
- [Hä19] A. Häußler, U. Fischer, and F. Warmer: *Use of mesh based variance reduction technique for shielding calculations of the stellarator power reactor HELIAS*. In: *Fusion Engineering and Design*, vol. 146 (2019), pp. 671–675. ISSN 0920-3796. doi:10.1016/j.fusengdes.2019.01.052
- [Igi06] Y. Igitkhanov, T. Andreeva, C. Beidler, et al.: *Status of HELIAS reactor studies*. In: *Fusion Engineering and Design*, vol. 81 (2006), no. 23–24, pp. 2695–2702. ISSN 0920-3796. doi:10.1016/j.fusengdes.2006.07.049
- [Iiy99] A. Iiyoshi, A. Komori, A. Ejiri, et al.: *Overview of the Large Helical Device project*. In: *Nuclear Fusion*, vol. 39 (1999), no. 9Y, pp. 1245–1256. doi:10.1088/0029-5515/39/9y/313
- [INT02] INTERNATIONAL ATOMIC ENERGY AGENCY: *ITER Technical Basis*. No. 24 in ITER EDA Documentation Series. Vienna: IAEA, 2002. URL <https://www.iaea.org/publications/6492/iter-technical-basis>. Last accessed on July 19, 2020
- [JEF14] JEFF-3.2: *JEFF-3.2 evaluated data library - Neutron data*, March 2014. URL [https://www.oecd-nea.org/dbforms/data/eva/evatapes/jeff\\_32/](https://www.oecd-nea.org/dbforms/data/eva/evatapes/jeff_32/). Last accessed on July 19, 2020

- [Kau13] M. Kaufmann: *Plasmaphysik und Fusionsforschung*. Springer Fachmedien Wiesbaden, 2013. ISBN 978-3-658-03239-5. doi:<https://doi.org/10.1007/978-3-658-03239-5>
- [Lei18] D. Leichtle, B. Colling, M. Fabbri, et al.: *The ITER tokamak neutronics reference model C-Model*. In: *Fusion Engineering and Design*, vol. 136 (2018), pp. 742–746. ISSN 0920-3796. doi:10.1016/j.fusengdes.2018.04.002
- [Lu14] L. Lu, U. Fischer, and P. Pereslavytsev: *Improved algorithms and advanced features of the CAD to MC conversion tool McCad*. In: *Fusion Engineering and Design*, vol. 89 (2014), no. 9–10, pp. 1885–1888. ISSN 0920-3796. doi:10.1016/j.fusengdes.2014.05.015
- [Mar14] R. L. Martz: *The MCNP6 Book on Unstructured Mesh Geometry: User's Guide*, March 2014. LA-UR-11-05668 Rev 8
- [McC11] R. McConn, C. Gesh, R. Pagh, et al.: *Compendium of Material Composition Data for Radiation Transport Modeling*. Pacific Northwest National Laboratory, Richland, Washington 99352, March 2011. Revision 1, PNNL-15870 Rev. 1
- [MCN03] MCNP: X-5 Monte Carlo Team: *MCNP - Version 5, Vol. I: Overview and Theory*. Los Alamos National Laboratory, 2003. LA-UR-03-1987
- [Mos15] S. W. Mosher, S. R. Johnson, A. M. Bevill, et al.: *ADVANTG An Automated Variance Reduction Parameter Generator*. Oak Ridge National Laboratory, Aug 2015. doi:10.2172/1210162. ORNL/TM-2013/416, Rev. 1
- [Mä88] M. Mäntylä: *An introduction to solid modeling*. Principles of computer science series ; 13. Rockville, Maryland: Computer Science Pr., 1988. ISBN 0-88175-108-1
- [Nor75] M. Norgett, M. Robinson, and I. Torrens: *A proposed method of calculating displacement dose rates*. In: *Nuclear Engineering and Design*, vol. 33 (1975), no. 1, pp. 50–54. ISSN 0029-5493. doi:10.1016/0029-5493(75)90035-7
- [Ped16] T. S. Pedersen, M. Otte, S. Lazerson, et al.: *Confirmation of the topology of the Wendelstein 7-X magnetic field to better than 1:100,000*. In: *Nature Communications*, vol. 7 (2016), pp. 1–8. doi:10.1038/ncomms13493. Article 13493

- [Per17] P. Pereslavytsev, U. Fischer, F. Hernandez, et al.: *Neutronic analyses for the optimization of the advanced HCPB breeder blanket design for DEMO*. In: *Fusion Engineering and Design*, vol. 124 (2017), pp. 910–914. ISSN 0920-3796. doi:10.1016/j.fusengdes.2017.01.028
- [Per20] P. Pereslavytsev, F. Cismondi, and F. A. Hernández: *Analyses of the shielding options for HCPB DEMO blanket*. In: *Fusion Engineering and Design*, vol. 156 (2020), pp. 111605/1 – 111605/6. ISSN 0920-3796. doi:10.1016/j.fusengdes.2020.111605
- [Qiu15] Y. Qiu, L. Lu, and U. Fischer: *Integrated approach for fusion multi-physics coupled analyses based on hybrid CAD and mesh geometries*. In: *Fusion Engineering and Design*, vol. 96 (2015), pp. 159–164. ISSN 0920-3796. doi:10.1016/j.fusengdes.2015.06.118
- [Qiu16] Y. Qiu: *Development of a coupling approach for multi-physics analyses of fusion reactors*. Dissertation, Karlsruher Institut für Technologie (KIT), 2016. doi:10.5445/IR/1000056066
- [Sal16] *SALOME - The Open Source Integration Platform for Numerical Simulation*, 2016. URL <http://www.salome-platform.org>. Last accessed on July 19, 2020
- [Saw09] M. E. Sawan, P. P. H. Wilson, T. Tautges, et al.: *Application of CAD-neutronics coupling to geometrically complex fusion systems*. In: *2009 23<sup>rd</sup> IEEE/NPSS Symposium on Fusion Engineering*. San Diego, CA, 2009. ISSN 1078-8891, pp. 1–6. doi:10.1109/FUSION.2009.5226505
- [Sch13] F. Schauer, K. Egorov, and V. Bykov: *HELIAS 5-B magnet system structure and maintenance concept*. In: *Fusion Engineering and Design*, vol. 88 (2013), no. 9–10, pp. 1619–1622. ISSN 0920-3796. doi:10.1016/j.fusengdes.2013.01.035
- [Sim18] S. Simakov, U. Fischer, A. Koning, et al.: *Iron NRT- and arc-displacement cross sections and their covariances*. In: *Nuclear Materials and Energy*, vol. 15 (2018), pp. 244–248. ISSN 2352-1791. doi:10.1016/j.nme.2018.05.006
- [Spa16] A. Spagnuolo: *Blanket Material Composition For Neutronics - March 2016 (2MU2ZL v 1.0)*. Techreport Volume 1.0, EUROfusion, March 2016.

- URL <https://idm.euro-fusion.org/?uid=2MU2ZL&version=v1.0>. Report IDM reference No.: EFDA\_D\_2MU2ZL
- [Spi58] L. Spitzer: *The Stellarator Concept*. In: *The Physics of Fluids*, vol. 1 (1958), no. 4, pp. 253–264. doi:10.1063/1.1705883
- [Sta10] W. M. Stacey: *Fusion : An introduction to the physics and technology of magnetic confinement fusion*. Physics textbook, 2<sup>nd</sup> edn. Weinheim: Wiley-VCH, 2010. ISBN 978-3-527-40967-9
- [Str11] U. Stroth: *Plasmaphysik - Phänomene, Grundlagen, Anwendungen*. 1<sup>st</sup> edn. Vieweg+Teubner | Springer Fachmedien Wiesbaden GmbH, 2011. doi:10.1007/978-3-8348-8326-1. ISBN: 978-3-8348-8326-1
- [The16] The UW CNERG Team: *DAGMC: Direct Accelerated Geometry Monte Carlo*. University of Wisconsin-Madison, 2016. URL <http://svalinn.github.io/DAGMC/>. Last updated on Oct 17, 2019. Last accessed on July 19, 2020
- [TT07] H. Tsige-Tamirat, U. Fischer, A. Serikov, et al.: *Automatic generation and validation of an ITER neutronics model from CAD data*. In: *Fusion Engineering and Design*, vol. 82 (2007), no. 15–24, pp. 1956–1959. ISSN 0920-3796. doi:10.1016/j.fusengdes.2007.06.038
- [Tur11] Y. Turkin, C. D. Beidler, H. Maaßberg, et al.: *Neoclassical transport simulations for stellarators*. In: *Physics of Plasmas*, vol. 18 (2011), no. 2, 022505. doi:10.1063/1.3553025. Article 022505
- [Wan19] S. Wang, F. A. Hernández, G. Zhou, et al.: *First thermal-hydraulic analysis of a CO<sub>2</sub> cooled pebble bed blanket for the EU DEMO*. In: *Fusion Engineering and Design*, vol. 146 (2019), pp. 2218–2221. ISSN 0920-3796. doi:10.1016/j.fusengdes.2019.03.156
- [War14] F. Warmer, U. Fischer, and C. Guerard: *Design of stellarator-specific breeder blanket and neutronic calculations (2NYFLH v 1.0)*. Techreport Volume 1.0, EUROfusion, 2014. URL <https://idm.euro-fusion.org/?uid=2NYFLH&version=v1.0>. Last accessed on August 16, 2020
- [War17] F. Warmer, V. Bykov, M. Drevlak, et al.: *From W7-X to a HELIAS fusion power plant: On engineering considerations for next-step stellarator devices*.

- In: *Fusion Engineering and Design*, vol. 123 (2017), pp. 47–53. ISSN 0920-3796. doi:10.1016/j.fusengdes.2017.05.034
- [Web17] WebElements: *Lithium: the essentials*, 2017. URL <https://www.webelements.com/lithium/isotopes.html>. Last accessed on July 19, 2020
- [Wil10] P. P. Wilson, T. J. Tautges, J. A. Kraftcheck, et al.: *Acceleration techniques for the direct use of CAD-based geometry in fusion neutronics analysis*. In: *Fusion Engineering and Design*, vol. 85 (2010), no. 10–12, pp. 1759–1765. ISSN 0920-3796. doi:10.1016/j.fusengdes.2010.05.030
- [Wob99] H. Wobig, E. Harmey, F. Herrnegger, et al.: *On Blanket Concepts of the Helias Reactor*. In: *IPP-Report III/244*, (1999). Max-Planck-Institut für Plasmaphysik, D-85748 Garching, Germany, EURATOM-Ass.
- [Wol10] R. Wolf, C. Beidler, R. Burhenn, et al.: *From Wendelstein 7-X to a Stellarator Reactor*. In: *Plasma and Fusion Research*, vol. 5 (2010), pp. 1–6. doi:10.1585/pfr.5.S1011. Article S1011
- [Wu09] Y. Wu and FDS Team: *CAD-based interface programs for fusion neutron transport simulation*. In: *Fusion Engineering and Design*, vol. 84 (2009), no. 7, pp. 1987–1992. ISSN 0920-3796. doi:10.1016/j.fusengdes.2008.12.041
- [Wu18] Y. Wu: *Multifunctional Neutronics Calculation Methodology and Program for Nuclear Design and Radiation Safety Evaluation*. In: *Fusion Science and Technology*, vol. 74 (2018), no. 4, pp. 321–329. doi:10.1080/15361055.2018.1475162
- [Yam06] T. Yamamoto, G. R. Odette, H. Kishimoto, et al.: *On the effects of irradiation and helium on the yield stress changes and hardening and non-hardening embrittlement of  $\sim 8\text{Cr}$  tempered martensitic steels: Compilation and analysis of existing data*. In: *Journal of Nuclear Materials*, vol. 356 (2006), no. 1-3, pp. 27–49. ISSN 0022-3115. doi:10.1016/j.jnucmat.2006.05.041
- [Zho17] G. Zhou, F. Hernández, L. V. Boccaccini, et al.: *Design study on the new EU DEMO HCPB breeding blanket: Thermal analysis*. In: *Progress in Nuclear Energy*, vol. 98 (2017), pp. 167 – 176. ISSN 0149-1970. doi:10.1016/j.pnucene.2017.03.013

- 
- [Zie13] A. Ziegler and H.-J. Allelein: *Reaktortechnik: Physikalisch-technische Grundlagen*. 2<sup>nd</sup> edn. Berlin, Heidelberg: Springer-Verlag, 2013. ISBN 978-3-642-33846-5. doi:10.1007/978-3-642-33846-5

# Appendix A

## Geometry translation approach with McCad

The traditional CAD to CSG geometry translation approach with McCad [Lu14] is investigated first. Defining geometrical regions with first- and second-order surfaces of analytical geometry and elliptical tori, and then combining them with Boolean operators results to the CSG description. McCad is developed at KIT and it is the standard CAD to MCNP geometry transfer option in fusion neutronics at KIT [Gro09]. The suitability of McCad for a stellarator reactor needs to be investigated.

The original blanket envelope model from IPP Greifswald, shown in figure 3.1, is used for the first investigations of the translation approach. The layered model contains much more spline surfaces, which makes a translation into CSG representation more difficult compared to the envelope model. Even the envelope model needs a lot of manual effort to simplify these surfaces.

The restrictions and limitations of MCNP for the CSG geometry description must be taken into account during the preparation of the CAD model. The CSG geometry is constructed mainly out of first- and second-order surfaces, but not of splines. The allowed surfaces in the MCNP geometry modelling are: plane, sphere, cylinder, cone, ellipsoid, hyperboloid, paraboloid, and elliptical or circular torus [MCN03]. In addition to this limitation, McCad does not support ellipsoid, hyperboloid and paraboloid for conversion.

The surfaces of the geometry are manually modified, because an automatic approach to simplify spline surfaces is currently not available. All spline surfaces are preponderant replaced with planes, cones and cylinders, and, at the end, a spline free stellarator model is created. It is also important to investigate and avoid possible topological changes in the model, and to ensure that the original and modified CAD model have similar volume. The volume consistency is an important criterion to be depicted along the entire simplification step.



One decomposed and simplified module, which corresponds to about one-fifth of one ring, is depicted in figure A.1 in comparison with its original shape. During the simplification, every modified part of the blanket envelope model has been tested separately in McCad, if it is feasible to be translated into MCNP geometry. After all modules are simplified, a McCad conversion with all parts has been performed.

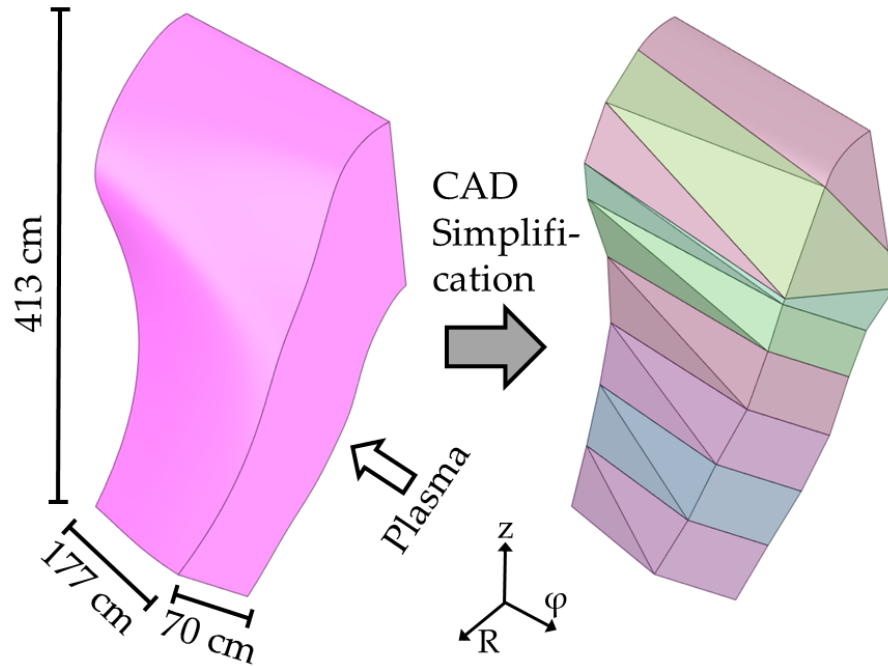


Figure A.1: Example of a CAD envelope module, left original and right after simplification and decomposition for the McCad conversion. Each volume on the right side has a different colour, independent from its material composition.

Preliminary MCNP calculations have been performed with the generated model aiming to demonstrate if the created geometry representation is usable for the simulation. Typically, a check for lost particles is executed for every CSG model generated with McCad. Therefore, a bounding sphere is introduced in the geometry, which is used as surface source to emit neutrons in direction towards the model, which means inside the sphere. The first test is performed with voided CSG model, the second test includes material assigned to the model. Some geometry errors can only be detected if the particles undergo interaction with the material and scattered or secondary particles take another direction in the random walk. Regarding the structure material, the homogeneous EUROFER mixture [Fin09] has been adopted in the tests. MCNP has a termination criteria for lost particles, which has been set to a higher value for these calculations. The MCNP manual [MCN03] advise to check every position where a lost particle occurs. During these simulations, more than 20% of the particles have

been lost. This high number is not acceptable, thus the investigation of the geometry problems has to be carried out. This demonstrated that the simplification of the surfaces leads to massive geometry problems in MCNP, especially if more than three surfaces are connected at the same edge or if tiny gaps between edges occur. Another problem arises from the inaccuracy of the CAD to MCNP geometry translation inside McCad due to the geometry tolerance. This also produces a lot of ill-defined geometry sections in the MCNP input geometry and can only be fixed by reducing the number of connected surfaces at one edge. Due to the large number of ill-defined sections, the manual repair and reconstruction of the geometry has been nearly impossible.

The experiences gained with the envelope model show, that the traditional CAD to CSG geometry translation approach with McCad is currently not suitable for modelling a stellarator.

## Geometry modelling with Unstructured Mesh (UM)

The representation of CAD geometry with UM description in MCNP is studied. A new feature of MCNP6.1.0 allows the mixture of traditional CSG and new UM together as so called ‘hybrid geometry’ [Goo12] [Mar14]. This feature allows any surface description in the CAD model which enables the use of more complex models in MCNP simulation compared to the CSG method. Additionally, a path length estimate of the flux is accumulated as particle track from one element face to another, to obtain the results for each element [Mar14].

The MCNP hybrid geometry is an arrangement with an unstructured mesh embedded inside the CSG geometry [Mar14]. The CSG geometry typically contains an envelope cell which is filled with this mesh geometry while this CSG cell must be slightly larger than the containing mesh geometry for this area. Otherwise overlaps, even coincide on the surface, of the envelope cell and the mesh element will lead to lost particles [Mar14].

UM geometry consists of finite elements. MCNP does only allow a few types of finite elements for the mesh, and a mix of different element types within one mesh is not recommended except pentrahedron and hexahedron. Possible finite elements are tetrahedron, pentahedron and hexahedron, shown in figure A.2. A tetrahedron is a volumetric body constructed by six edges and is bounded by four triangular faces. A hexahedron is a volumetric body constructed by nine edges and is bounded by two triangular and three quadrilateral faces. A hexahedron is a volumetric body constructed by twelve edges and bounded by eight quadrilateral faces [Mar14]. The tetrahedral

mesh is preferred, because it is, compared to both other mesh element types, able to fit better to bend geometry. All meshes used in this work have been generated as tetrahedral elements. Each UM is set-up in Abaqus format, which is currently the only supported mesh format of MCNP.

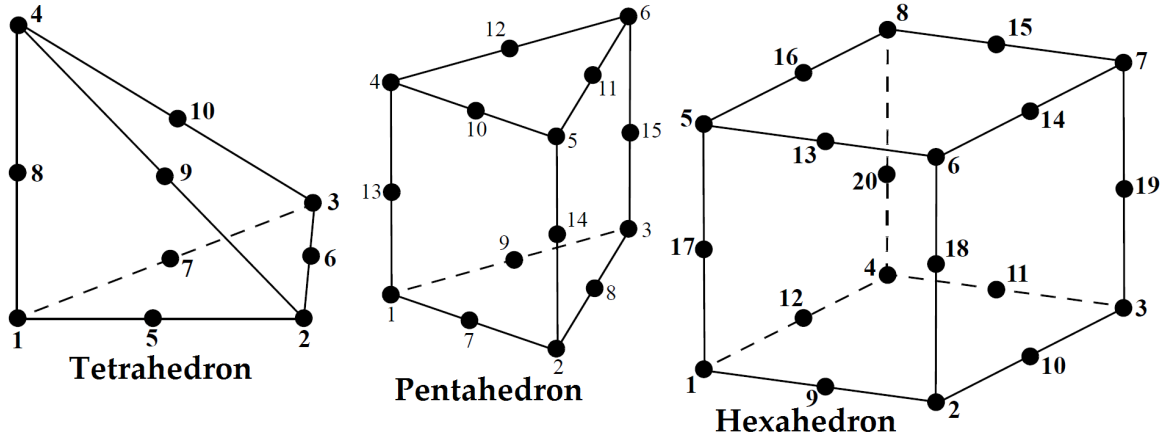


Figure A.2: Schematics of first order finite elements including midpoint nodes to construct an unstructured mesh. [Mar14]

The hybrid geometry has drawbacks compared to the traditional CSG description. Some restrictions and limitations, which might affect this work, are [Mar14]:

- multiple unstructured mesh files are not functional in one simulation geometry,
- an MCNP universe cannot be placed within a mesh universe,
- CSG surfaces must not clip or intersect the unstructured mesh,
- the MCNP plotter will plot limited aspects of the unstructured mesh for the purpose of seeing its position in the hybrid geometry, no cell lines or single mesh elements are plotted,
- reflecting and periodic boundary conditions are not guaranteed to work with the unstructured mesh itself but should work with CSG cells/surfaces that have these conditions,
- surface tallies are not permitted in the unstructured mesh,
- even running parallel on several computer cores with Message Passing Interface (MPI), problem set-up may take considerable time if any one part has many (> 30,000 – 50,000) elements.

These restrictions must be taken into account during the UM geometry preparation. Nevertheless, the benefit of this method is that there are nearly no limitations in respect to the surface description in the CAD model. This means in theory that the layered HELIAS model, including all its spline surfaces, can be used as input for this approach.

It is important to use appropriate software to generate the UM geometry. Any problems in this step can lead to massive problems during the MCNP simulation, which leads to problematic results. The meshing software used must generate an UM which fits into the MCNP limitations and which can be exported into the MCNP UM data format. The KIT in-house developed coupling system for multi-physics analyses of fusion reactors [Qiu15] [Qiu16], based on the SALOME platform [Sal16], is investigated first. The internal mesh generator of SALOME has not been able to generate a geometry mesh due to the complex shape of the stellarator. The second investigated meshing tool is integrated in the ANSYS Workbench platform [Ans18]. The ANSYS package provides SpaceClaim as default CAD software, which has been used for KIT fusion neutronics for many years, and several mesh generation tools for different types of application. A benefit of the ANSYS package is that the internal data exchange is standardised between the different tools which prevents the loss of data. Therefore it is more convenient to manipulate CAD data in SpaceClaim and transfer it into ANSYS Workbench for meshing. This tool package has managed to generate the geometry mesh for HELIAS. All performed quality checks for the mesh are described in the section A.

The most challenging parts in the mesh generation are the 2 mm thick tungsten layer as well as the 25 mm thick first wall. The ratio between its total size of the plasma facing side of around 240 m<sup>2</sup> together with their low thickness causes a lot of issues. A large number of small mesh elements need to be generated to represent these layers, which increases the total number of mesh elements heavily. All other material layers could be transferred into mesh representation without such problems. An example is given in figure A.3 with the tungsten layer on the top and the breeding layer on the bottom side. It can be clearly seen that much more mesh elements are needed to represent the tungsten layer, while the thickness of this layer is much less compared to the breeding zone.

A critical point in the mesh generation is at the interfaces between geometry parts. It must be ensured that nodes on these interfaces used are for meshing of all neighbouring geometry parts to avoid an overlapping mesh geometry. This is important because it could lead to errors in the particle transport simulations later performed.

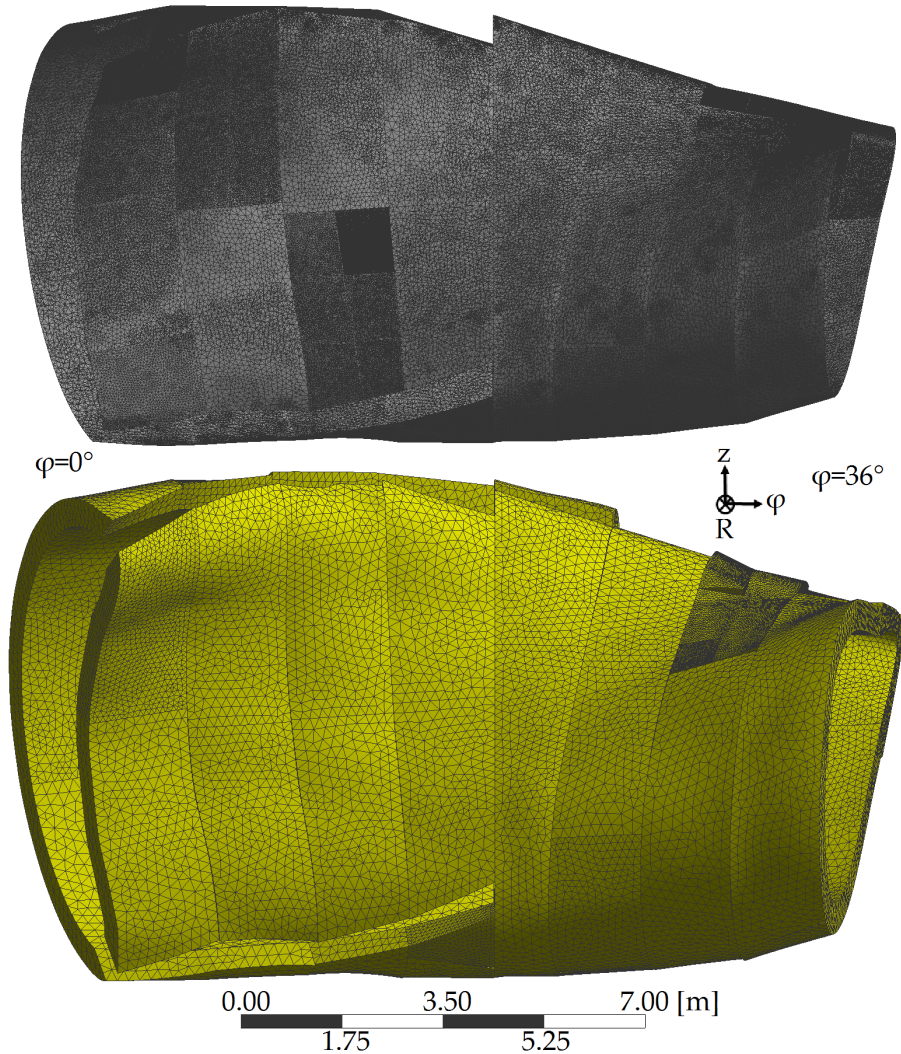


Figure A.3: Tungsten (top, light grey) and breeding zone (bottom, yellow) after generation of unstructured mesh geometry with tetrahedral mesh elements.

## Direct acceleration geometry with DAGMC

The third investigated geometry translation approach is the Direct Accelerated Geometry (DAG) technique implemented in DAGMC. DAGMC is a patch for MCNP in order to allow the use of a facet geometry description in the particle transport simulation. The code was developed at the University of Wisconsin-Madison [The16]. The DAGMC patch for MCNP5 is used in this work, which is well validated and supports most of the MCNP5 functionalities.

DAGMC is a direct geometry acceleration approach, which allows the MC radiation transport operations to be evaluated directly on the CAD model. The internal geometry representation is converted from CAD boundary representation into faceted

surfaces. This method is slower in computational time compared to the traditional CSG description by a factor of 2 to 5, but the DAGMC developers made efforts to accelerate the calculation speed. DAGMC is designed to be integrated with any Monte Carlo radiation transport tool, replacing a handful of the built-in particle tracking methods with those specifically designed for the CAD-generated geometry [Wil10].

DAGMC is based on the Cubit library, which is both a part of the CUBIT Toolkit [Bla17] and a part of Trelis [Cor20]. The Cubit library is a part of a toolkit for robust generation of two- and three-dimensional finite element meshes (grids) and geometry preparation [Bla17]. The Cubit Toolkit is available for US government use only, but for non-US government use Trelis, a commercial version of Cubit, is available [Bla17]. Trelis is used due to this licensing constraint to process the HELIAS CAD geometry.

The CAD data preparation is different compared to the other two approaches. All CAD manipulations, like removing small gaps or tiny overlaps between parts of the geometry, or splitting large and complicated parts into smaller ones, are done in SpaceClaim. The CAD data must be transferred to Trelis, where most of the steps for the generation of the DAGMC geometry are performed. The DAGMC developers recommend the data transfer in ‘ACIS’ format, because it can store information about material, if defined in the CAD file, as well as it is more robust compared to the data transfer in other formats for Trelis. It must be noted, that the data transfer between SpaceClaim and Trelis is not free of errors, sometimes Trelis shows geometry errors while SpaceClaim could not detect them. Therefore a geometry check has been performed in Trelis after every geometry import.

Trelis provides the ability to group parts of the geometry to link them to an MCNP material number, which must be defined in the MCNP input file, and its corresponding density. It is also possible to define boundary condition, like reflecting boundary, and the graveyard area which must be defined to guarantee a working simulation afterwards. Additionally, geometry parts can be linked to a tally, like heating or particle flux [The16]. This is not mandatory to include it during the geometry preparation step, it can be included later in the MCNP input file. It is recommended by the developers to use these abilities in Trelis for the geometry preparation, because the 3D view of the model in Trelis can be used to provide these additional information.

An important step inside Trelis for the geometry preparation is the ‘imprint’ and ‘merge’ step. The geometry imported in Trelis is a so called ‘manifold geometry’ which means that adjacent bodies do not share surfaces, even if those surfaces overlap. To produce a ‘non-manifold geometry’, imprint and merge operations are necessary [Cor20]. If this step is not made correctly with the geometry, the subsequently parti-

cle transport simulations can cause unexpected geometry errors and return incorrect results. An example of the process can be seen in figure A.4, starting from left to right. Here, the two volumes A and B are neighbours which have, due to the machine accuracy, a tiny gap in between. The surfaces 1 and 2 are facing each other, but have different dimensions. The imprint operation shown in figure A.4 middle projects topology differences from one geometry to the other. It creates a new surface 3 during this operation which has the same dimension as surface 2 and is ‘imprinted’ at volume A. The following merging step ‘merges’ the touching surfaces and converts them into one entity [The16] [Cor20]. The result of both operations is shown in figure A.4 right. A drawback of this process is, that it can be very time consuming. The duration of the imprint step is dependent on the model complexity and required for the HELIAS model around 9 h.

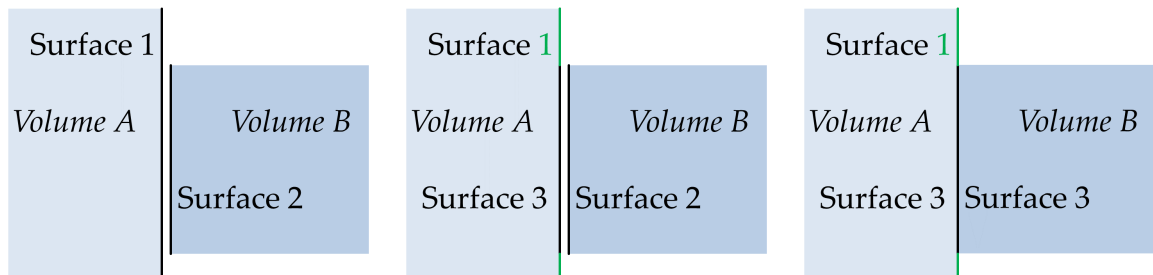


Figure A.4: Geometry before imprint and merge operation (left), after imprint step (middle), and after successfully applied imprint and merge operation (right). [The16]

The imprint and merge step is the last geometry preparation step before exporting the whole geometry into a DAGMC suitable format, requiring a dedicated plugin for Trellis. The time used for the export depends heavily on the chosen ‘`faceting_tolerance`’, which can be manually adjusted and the DAGMC developers recommend a ‘`faceting_tolerance`’ of  $1 \times 10^{-4}$ . This step needs around 2 h for the HELIAS model. Afterwards, the geometry must be sealed by starting the DAGMC tool ‘`make_watertight`’. This tool is doing several steps after starting the task [The16]:

- finding degenerate triangles,
- modifying faceted curve representation and removing small curves,
- identifying coincident curves to be merged,
- zipping loops and removing small surfaces whose curves were all merged as pairs.

The success of this step is proven with the tool ‘check\_watertight’. An adjustment of the parameter and a re-export of the geometry could fulfil the requirements to succeed all the step. The final HELIAS model contains  $\sim 100$  Mio triangles.

Included are in the exported geometry now information like ‘which volume has which MCNP material number’ and the ‘boundary conditions’, but no details about material compositions. Therefore, the tool ‘uwuw\_preproc’ [The16] is needed which links the material numbers inside the geometry with the material composition, provided in a dedicated file by the user, in the whole DAGMC geometry. After this step a DAGMC suitable geometry is reached, which can be used for particle transport calculations. The complete geometry is shown in figure A.5. It shows on the top a view to the model from the centre to the inboard side, where the volume cells are coloured by their corresponding material. On the bottom is a cross-section at the mid-plane, representing  $z = 0$  cm, through the model, including bounding box (light grey) with reflecting boundary conditions at the bean  $\varphi = 0^\circ$  and triangular  $\varphi = 36^\circ$  shaped side. The fusion plasma is represented as large red volume in the middle of the geometry. This volume is needed to guarantee an error free generation of birth neutrons inside the DAGMC geometry.

The MCNP input file for DAGMC looks different, it only contains the data cards without material definition. The information about the cells, surfaces, tallies (if in Trellis defined) and materials are stored in the ‘lcad’ file, which is created automatically at the first run of the geometry by DAGMC using the information provided in Trellis and during the material link step.



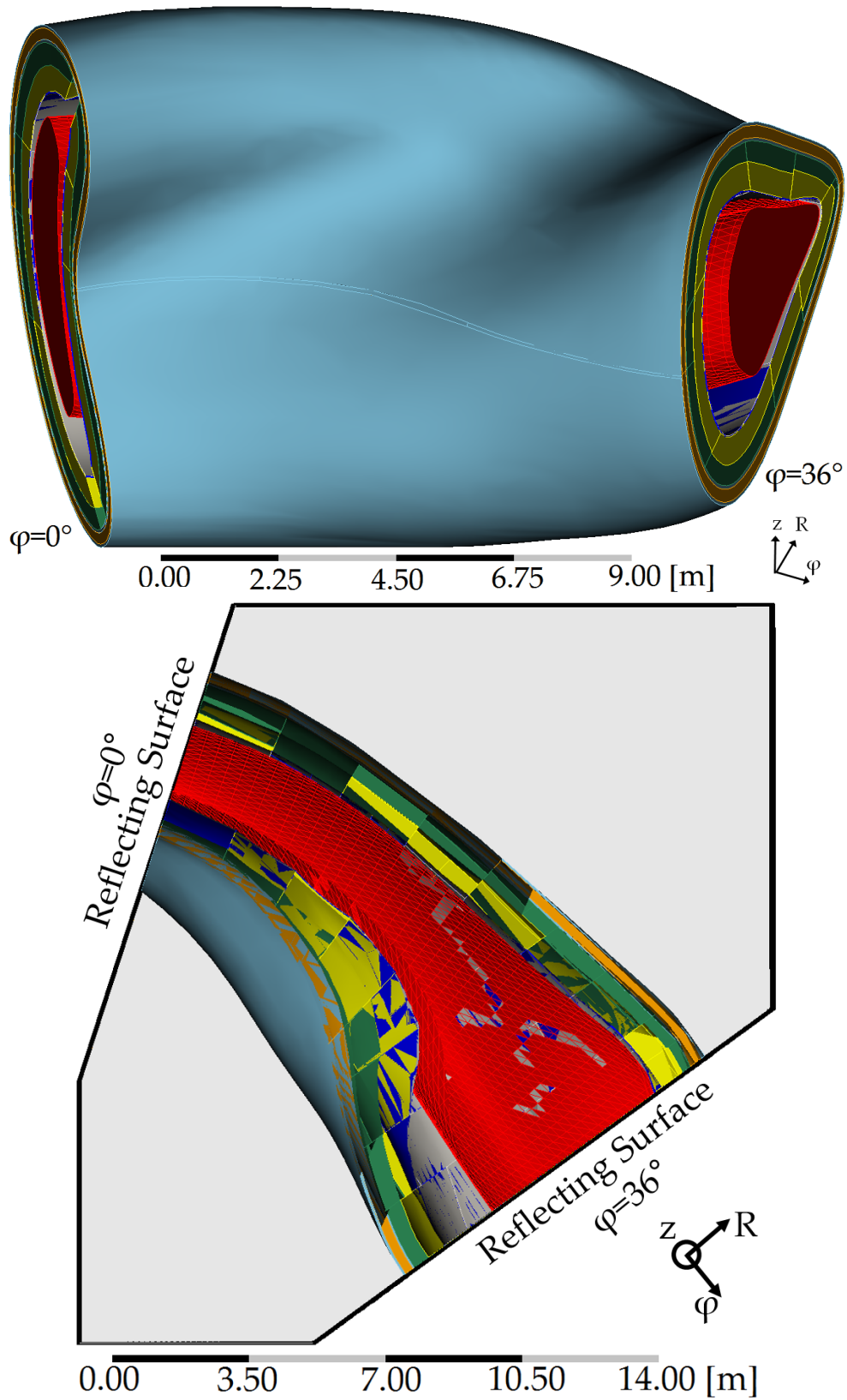


Figure A.5: HELIAS geometry in DAGMC representation, top: view from inboard to the triangular shaped side; bottom: cross-section at the mid-plane including the bounding box (light grey).

## Proof of the computational geometry consistency

Two different criteria are considered for the quality check between the CAD geometry and the computational geometry. First, the volumetric deviation must be as small as possible and second, the appearance of lost particles in MCNP simulation with the computational geometry should be avoided. An acceptable lost particle rate for ITER tokamak neutronic calculations is ‘generally below 1 in  $10^7$ ’ [Lei18] starting particles. The same value is taken as reference for HELIAS as no other limitations are specified.

Lost particle checking is done in several steps, in voided geometry (all materials are replaced by void) to not take any collisions in the particle track with the material into account. The calculation requires a neutron source, defined as sphere surrounding the computational geometry, and emitting the particles from the sphere surface directed towards inside. The particles cross the computational geometry in a straight way through cell boundaries and get killed when they reach the sphere again. MCNP cannot detect gaps or overlapping cells inside the geometry unless a particle track is lost. If there is a geometry error, which means an ill-defined part inside the geometry, MCNP terminates the particle history and registers in an output file the location of this lost particle.

The second check including all materials and the plasma neutron source, which provides information about ill-defined locations that are reached by scattered or secondary particles. Some of these errors could hardly be detected inside the voided geometry. This check helps to find out most of the locations of lost particles and to judge, if the total lost particle rate per source particles is acceptable. If the lost particle locations are not affecting the concerned regions, these lost particle can be considered less important.

### Quality assurance for CSG

The CSG model accuracy is proven by performing a stochastic volume calculation with MCNP and comparing it with the volume of the CAD data. The accuracy depends also on the conversion algorithm used in McCad [TT07]. The test is done internally in McCad during the conversion process for each solid. These check results in the deviations of the CSG solid and the CAD solid are below 1 % which is considered as negligible.

The lost particle check has been performed as described previously. As this geometry contains only one layer, steel [McC11] is used for this test with different material densities. The density range chosen are 25 %, 50 %, 75 % and 100 % of the original steel

density. The different densities have an effect on the particle transport. This means that the particles undergo interactions with the material and, due to the material density change, the probability rises to find more ill-defined geometry areas.

The performed checks have exhibited a very poor quality of the CSG model with a lost particle rate of about 20%. A lot of lost particles have been encountered in areas with three or more surfaces which share an edge or a curve, because McCad cannot process these surfaces in the stellarator correctly. A modification on such regions in the CAD model leads to a massive deviation to the original spline model, therefore it is not applicable. Another problem is that the CSG model includes only one material layer. The introduction of more layers to represent the stellarator in a higher accuracy approximation causes even more ill-defined CSG geometry regions. All these reasons have led to the conclusion, that the traditional CAD to CSG geometry translation approach with McCad is not well suited for stellarators.

## Quality assurance for UM

The hybrid UM geometry needs additional checks compared to the CSG geometry. A very important check is the investigation of the Jacobian ratio. The Jacobian ratio is a rate of the deviation of a given element from an ideally shaped element. In an ideal case, the Jacobian ratio for all mesh elements equals 1. While in a worst case it is a large spread of the Jacobian ratio about several orders of magnitude including negative values. For testing purpose, the tool ‘um\_pre\_op’ is provided within the MCNP6 package and can be used for UM quality checks. It allows the checking of the abaqus mesh for ‘deformed and/or twisted elements by calculating the determinant of the Jacobian at all node locations that define the finite element’ [Mar14]. Correctly defined elements have a positive Jacobian, otherwise the mesh is damaged and needs to be fixed with a meshing tool [Mar14]. An example for a twisted mesh element, which fails the Jacobian test, is shown in figure A.6.

This test criteria is used during the generation of the abaqus mesh in ANSYS, because ANSYS provides a statistical test to check for the Jacobian ratio. If there is a large deviation from 1 in the Jacobian ratio occurs, the mesh is not suited for any further investigation.

Nevertheless, only relying on the Jacobian ratio is not sufficient. An example: the location shown in figure A.7 is a part at the triangular shaped side,  $\varphi = 36^\circ$ , of the stellarator. Two different mesh settings are presented, left a coarse mesh with overlapping and right a finer mesh without overlap, that both pass the Jacobian ratio

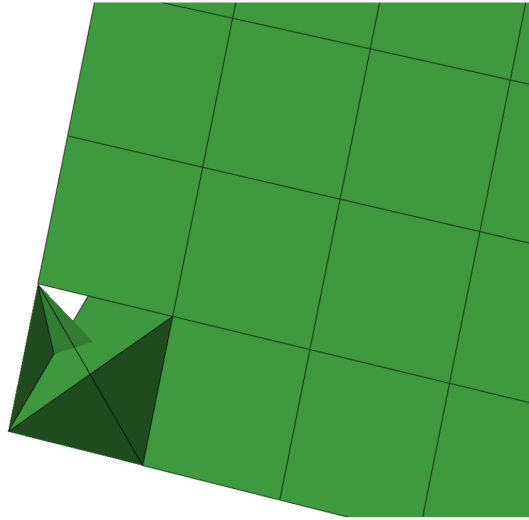


Figure A.6: Example for a twisted first-order tetrahedra mesh element. [Mar14]

test. It is clear, only by the visual comparison, that the left mesh from figure A.7 cannot be taken for the particle transport calculations. Overlapping areas must be avoided during mesh creation, which can only be done while setting up the mesh generator in an appropriate way to take into account all solid boundaries and, in an ideal case, connect all mesh element boundaries to avoid overlapping. The mesh element test of ANSYS provides this information about the mesh quality.

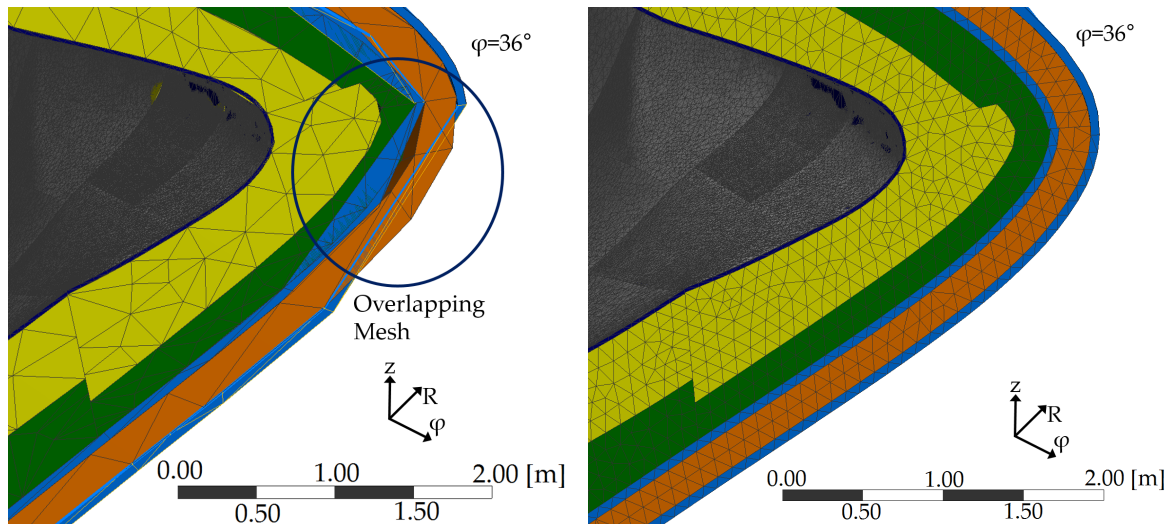


Figure A.7: Two different mesh which both pass the Jacobian ratio check. The mesh is shown at the tip of the bean shaped side  $\varphi = 36^\circ$ . The left mesh has overlaps, highlighted in the blue circle, which occurs problems during particle tracking.

An additional test from ‘um\_pre\_op’ is the volume checking. This test ‘enables the user to check the finite element volumes (against a value) and to obtain volumes

and masses for the pseudo-cells' [Mar14]. It is executed automatically and provides the differences between mesh and CAD. The result of the test show a deviation between CAD and UM less than 0.11 % for the layered HELIAS model. This difference is tolerable and does not need to take into account for upcoming MC particle transport calculations.

## Quality assurance for DAGMC

The quality assurance for the DAGMC approach is more intensive than for the other two approaches. Trellis includes internal checks which are looking for, e.g. overlapping volumes and surfaces, small areas, small curves and small surfaces. Some of these checks are very time consuming, e.g. the check for overlapping volumes needs more than 26 h for the HELIAS model.

The 'imprint' step in the model preparation is indispensable, but it causes slight volume changes in the post-imprint model. A comparison of the pre- and post-imprint volume is important which is done in Trellis with the help of a user defined script. The script can determine the volume size, therefore it must be run before and after the 'imprint' step to obtain volume differences. In the HELIAS model, a maximum difference of the pre- and post-imprint volumes  $\leq 4\%$  is reached. The vast majority of the volumes have deviations below 1 %.

A fully water-tight model is a basic requirement in order to avoid lost particles in the radiation transport simulation. After the geometry export into a the DAGMC format, the tool 'check\_watertight' is executed, which is part of the DAGMC package and checks if all solids are completely sealed in the export step. Around 99 % of all volumes in the layered HELIAS model are sealed, a higher rate could not be achieved. The whole geometry preparation process is very sensitive and each modification of the CAD geometry can cause new problems, especially with the complex HELIAS representation.

The lost particle check, where a surrounding sphere is used as surface source, cannot be performed, because a sphere cannot be assigned as surface source. The DAGMC developers recommend as alternative a check with a plasma neutron source and reduced material density inside the geometry. An acceptable lost particle rate given by the developers is  $\leq 1/5 \times 10^6$  per source particles [The16]. Some regions, mostly small edges or tiny curves, lead to a hot spot of lost particles where rates were obtained of several 10000 lost/ $1 \times 10^6$  birth particles. These areas were all fixed in the CAD model. Other locations of the lost particles, which were in the middle of a cell volume,

could hardly be removed. It was found, that such areas are too complicated for the Trellis processing, and after separating them into smaller volumes, the lost particle rate decreased. Nevertheless, a lost particle-free model could not be generated, even with using different output tolerances for the DAGMC geometry. The lowest rate achieved in this work has been  $\sim 2 - 3$  lost/ $1 \times 10^6$  birth particles and the lost particles are spread over the whole geometry. The rate is higher than the recommended rate by the DAGMC developers, but is considered in general as acceptable for the upcoming simulations.

## Limitations in performing calculations with the different geometry set-ups

The application of different CAD to MCNP geometry approaches can cause many failures of the MCNP simulation, as well as a different cost of computation resources. It is important to know in advance some of the problems which can occur while taking these geometry description rather than CSG. Therefore, the UM and DAGMC drawbacks are discussed here.

### UM

Theoretically, every CAD model can be used for the UM neutronic analyses. Nevertheless, it is a recent development of the geometry description in MCNP6 and it only supports a limited number of tallies. Currently, the method can only be used as a candidate, but it seems to be a promising method. Some drawbacks for the UM geometry are concluded based on the geometry preparation and performing of MCNP calculations, which are:

**Geometry processing time** The mesh geometry must be parsed and processed by MCNP before each calculation into an internal data format. This step cannot be skipped because the internal data format is mandatory to perform calculations.

**Simulation freezes without returning feedback** A problem was encountered that MCNP 6.1.1beta sometimes returns no feedback about computational issues and runs into infinite loops. This has to do with the UM quality and also with the chosen random number generator in MCNP. This problem is very complicated and at the end it is not solved completely. It is assumed that MCNP 6.1.1beta

has some problems in internal subroutines that run into infinite loops during the particle tracking, without the possibility to exit them.

**Large computational resources required** A lot of Random-Access Memory (RAM), in the order of 8 – 10 GB per CPU core, is occupied by MCNP when running UM geometry. This limits the usability on large scale computational systems, as typically the ratio between RAM per CPU core is lower than required. An example is the cluster ForHLR II at KIT which has a ratio of 3.2 GB RAM per CPU core on a regular computational node.

**Slow computational speed compared to CSG** A higher number of mesh elements in a model increases the time consumption for the particle tracking. MCNP must check the particle intersection with the geometry at each surface crossing. The layered HELIAS model contains a large amount of mesh elements and therefore a significant slow down of the simulation speed is detected.

## DAGMC

The DAGMC approach can theoretically process any CAD model into a MCNP computational model. Nevertheless, some drawbacks of this method are encountered during usage in radiation transport calculations:

**Many dedicated software suits needed** The DAGMC package relies on different external codes, e.g. MOAB or HDF5. It is important to check for the specific versions of these codes as proposed by the DAGMC developers. Sometimes newer code versions introduce changes which are not taken into account in the older DAGMC version. The installation process of DAGMC on a computational cluster is error-prone if the correct software versions are not used.

**Lost particle locations occurrence** It was encountered that the reduction of lost particle locations is not straightforward. Even in regions which are not overlapping during one step to the other, lost particles show up. It is not clear about the reasons and a careful check in the geometry as well as in the export parameters is important to receive a low lost particle rate in the computational geometry.

**Large computational resources required** The faceted geometry description of HELIAS needs around 14 GB RAM per CPU core which highly limits the usability of computational clusters. The solution in this work is to set-up a dedicated computer with 512 GB RAM and 48 cores to run DAGMC calculations on it.

**Slow initialisation time** The DAGMC geometry must be processed at each computational run which lasts around 8 h and cannot be accelerated. It writes a processed geometry file in the folder that can be used for a next computational run with the geometry. A test comparison shows that the start-up from the already processed geometry file is slower than writing a new processed geometry file, which means that a long waiting time until the start of the particle tracking cannot be avoided.

**Slow computational speed compared to CSG** A large number of surface facets decreases the computational performance, as DAGMC needs to check at each facet crossing what happens with the crossing particle. The layered HELIAS model contains around  $10^8$  facets which slow down the computational time significantly.



# Acknowledgements

I would like to express my sincere gratitude to all who have contributed to the success of this dissertation through their professional and personal support. First of all, thank you to Prof. Robert Stieglitz and Dr. Ulrich Fischer for giving me the opportunity to work on my dissertation at the Institute for Neutron Physics and Reactor Technology (INR). Thank you to Prof. Robert Wolf for co-referring and enabling the dissertation as cooperation project between KIT and IPP Greifswald. I am deeply grateful to all of them for their valuable guidance, their constant support and their constructive review of my dissertation.

I also thank all my colleagues of the ‘Neutronics and Nuclear Data (NK)’ group. The eye-opening discussions, sharing ideas and their professional knowledge have been an important contribution to my thesis. Thank you to Yuefeng, Bastian, Pavel, Dieter, Elena, Prasoon, Lei, Arkady, Anton, Jin Hun and all other colleagues.

Thank you to the INR secretaries, Mrs. Schwartz, Mrs. Klug and Mrs. Zagolla, for their support in all organisational questions. Thanks to Peter Moster who helped me with all my IT problems, and set-up of a dedicated computer to perform my neutronics calculations.

Thank you to Felix Warmer and his colleagues at IPP Greifswald. Their support by providing necessary input data and being open at any time for discussions has been very important for my dissertation.

Sincere thanks to the DAGMC developers, in particular to Prof. Paul Wilson (University of Wisconsin - Madison) and Andrew Davis (UK Atomic Energy Authority), who helped me to learn, understand and use DAGMC.

A very special thanks to my family, most of all to my mother and my sister, who always stood by my side during this difficult time.